Investigation of Magnetic Pulse Welding on Lap Joint

of Similar and Dissimilar Materials

Dissertation

Presented in Partial Fulfillment of the Requirements for the Degree Doctor of Philosophy

in the Graduate School of The Ohio State University

By

Yuan Zhang, B.S., M.S.

Graduate Program in Materials Science and Engineering

The Ohio State University

2010

Dissertation Committee:

Dr. Glenn S. Daehn, Advisor

Dr. Sudarsanam Suresh Babu, co-Advisor

Dr. Michael J. Mills

Dr. David Rigney

Dr. Shelly D.Jepsen

Abstract

The main objective of this research is to investigate the magnetic pulse welding (MPW) process, the resulting joint strength and the interface welding metallurgy. It is known that traditional fusion welding is not able to weld dissimilar materials with different thermal properties, but MPW has been applied to both similar and dissimilar materials. MPW is a solid state impact welding technology that may provide metallurgical bonding without melting and solidification, and there is no significant heat affected zone (HAZ). It shares the same physical principle with explosive welding (EXW) and is good for workpiece with length scale in the order of millimeter to centimeter. This research first compares three impact welding technologies, EXW, MPW and laser impact welding (LIW), for different length scale with different driving system. The joining is likely the result of an instability associated with jetting, which scours the surface clean during impact. It was found that the metallurgical bonding by oblique impact was only realized at the combination of certain impact velocity and impact angle. Taking 0.254mm thick copper alloy 110 plate to plate joint as an example, the suitable impact velocity was larger than 250m/s and the suitable impact angle was within $2°\sim7°$. As a result, the joint interface undergoes high strain rate deformation and the strain rate was established in the order of $10^6\sim10^7\mathrm{s}^{-1}$. In this research, aluminum alloy, copper alloy, and low carbon steel were

welded by MPW using electromagnetic force to accelerate the metal. The strengths for both similar and dissimilar material joints were examined by lap shearing test, peeling test and microhardness test, and the similar materials joint was also tested by nanoindentation. The joint strength was greater than that of the base metals and the welded region was hardened by high velocity impact. The tensile failure and peeling failure were outside of the welded region. The welded interface microstructure was characterized by optical microscopy, scanning electron microscopy, electron backscatter diffraction, transmission electron microscopy, and field ion atom probe microscopy. The welded interface indicated wave interface morphology. Due to adiabatic heating and high strain rate deformation, the welded interface microstructure exhibited various features, including grain refinement with large grain boundary misorientation angle, formation of band structure, deformation twins, lamellar grains, and high dislocation density (~estimated to be $10^{11} m^{-2}$). Similar materials welding suggested pure solid state bonding, while dissimilar materials joints sometimes contained small amount of intermetallic phase distributed discontinuously in the vertex region of certain waviness along the welded interface. In order to identify the coupled thermal, electromagnetic, and mechanical properties during the impact welding process, a finite element analysis was attempted via LS-DNYA®. Some of the simulation results were compared to the instrumented experiments and the validated model can be used to investigate the successful welding criterion with regard to the impact angle and impact velocity for other materials.

Dedication

In memory of my beloved grandmother, Ms. Fenying Zhang.

谨以此论文献给我挚爱的外祖母，张粉英女士。

Acknowledgements

My study in the past four years cannot be completed without the help from many individuals and the financial support from American Welding Society. All these efforts help me go through the research work with great pleasure.

First, I want to show great appreciation to my advisors Professor Glenn Daehn and Professor Sudarsanam Suresh Babu. They are always the constant source of guidance and support. They motivate me to think with critical perspective and to apply the text book knowledge on solving real problems. They offer me the chance to work on such interesting research topic and create many unique opportunities for me to explore aboard on materials science, all of which enriched my research work at OSU to be a worthwhile experience. After four years working together, I am deeply impressed by their global perspective, noble personalities, hard working, and their passion for discovery. I feel very lucky to have them not only as the mentors and role models, but also as the friends. Thank you, Glenn and Suresh, for your effort and faith on me.

I thank Professor Michael Mills and Professor David Rigney for being my dissertation committee. I appreciate their kind help and useful discussions on my research work. I

also want to point out that it was a great pleasure to work as the teaching assistant twice for their Materials Characterization classes. It was not only a great teaching experience but also a nice training for my communication skills.

I want to thank the assessment from American Welding Society (AWS) on the impact welding technology and my performance. It is a great honor to be one of the four winners among North American universities for AWS Fellowship Award since 2007. The generous financial support for continuous three years offers me the best opportunity to investigate magnetic pulse welding.

I also highly appreciate the SHaRE program from Oak Ridge National Lab (ORNL) sponsored by the Scientific User Facilities Division, Office of Basic Energy Sciences, U.S. Department of Energy, which allows me to use the state-of-the-art facilities freely. These unique opportunities helped me to understand the microstructure evaluation down to atomic level resolution. The scientists at ORNL are all very kind and they offered me nice help on my on-site working, and they are Dr. Michael Miller, Kaye Russell, Kathy Thomas, Dr. Ai Serizawa, Tom Geer, Dr. Ed Kenik, Dr. Hongbing Bei, and Dr. Sang Hoon Shim. It is a great experience to work with such nice and patient scientists.

Thanks to Curtis Prothe, Micheal Blakely at Dynamic Materials Corporation and John Kwasegroch, Mike LaHa at Continuum Inc. for their help on the study of different length scales impact welding. Thanks to Pierre L'Eplattenier and Mike Burger at Livermore

I also thank my friends at our department. They encouraged completing my study overseas and gave me the chances to express the scientific ideals loudly and confidently in my second language. Especially, thanks to Professor Suliman Dregia, Professor James C. Williams, Dr. Ed Herderick, Clarrisa Yablinsky for help on many mock exams, and they taught me to gratefully cheer for myself rather than keeping happiness deep down inside. Thanks to Dr. Adam Pilchak for his great help on my EBSD sample preparation. Thanks to Dr. Alpesh Shukla, Dr. Libor Kovarik, Dr. Amit Samanta, Dr. Ning Zhou, Dr. Weiqi Luo, Li Sun, Dr. Liang Qi, and Dr. Dong Liang for their general discussions.

Last but not least, I also deeply appreciate the love and support from my family. Thanks to my parents' endless love. They walked me through the frustration and taught me the secret to realize my dreams: work hard with patience. Thanks to my elder sister who always stand with me shoulder by shoulder to face both the happy time and the hard time. Thank you, Mom, Dad, and Sis! Sincere thanks to my wonderful boyfriend, Kuiyu Li for his great understanding and accompany in these years, and I am looking forward to explore more adventure with you in the future.

Vita

Born November 6, 1981……………………...Yinchuan, Ningxia, China

2004………………………………………..B.S. Materials Science and Engineering

Zhejiang University, China

2005……………………………………… M.S. Innovation of Manufacturing System

and Technology, Singapore-MIT Alliance,

Singapore

2007……………………………………… M.S. Materials Science and Engineering

The Ohio State University

2005-Present…………………………………Graduate Research Associate

The Ohio State University

2007-Present……………………………… American Welding Society Graduate

Student Fellowship

Publications

1. Application of High Velocity Impact Welding at Varied Different Length Scales, **Y. Zhang**, S. S. Babu, C. Prothe, M. Blakely, J. Kwasegroch, M. LaHa and G. Daehn, Journal of Materials Processing Technology, (2010)

2. Coupling Experiment and Simulation in Electromagnetic Forming Using Photon Doppler Velocimetry, J. Johnson, G. Taber, A. Vivek, **Y. Zhang**, S. Golowin, K. Banik, G. Fenton, G. Daehn, Metal Forming, Volume 80, (2009), No.5, P359-365

3. Microstructure Characterization of Magnetic Pulse Welded AA6061-T6 by Electron Backscattered Diffraction, **Y. Zhang**, S. S. Babu , P. Zhang, E. A. Kenik, and G. S. Daehn, Science and Technology of Welding and Joining, Volume 13, (2008), No.5, P467-471

4. Experimental Study and Numerical Simulation for Magnetic Pulse Welding Process on AA6061-T6 and Cu101 Sheet, **Y. Zhang**, P. L'Eplattenier, G. Taber, A. Vivek, G. Daehn, and S. S. Babu, 10th International LS-DYNA® Users Conference Proceeding (2008), P8-13~8-23

5. Materials Constitutive Parameter Identification Using an Electromagnetic Ring Expansion Experiment Coupled with LS-DYNA and LS-OPT, I. Henchi, P. L'Eplattenier, G. Daehn, **Y. Zhang**, A. Vivek, and N. Stander, 10th International LS-DYNA® Users Conference Proceeding (2008), P14-1~14-9

6. Microstructure evolution of Magnetic Pulse Welded Interface, **Y. Zhang**, P. L'Eplattenier, S. S Babu, and G. Daehn, 8th International Conference on Trends in Welding Research Proceeding (2008)

7. Mn Effect on Wurtzite-to-cubic Phase Transformation in ZnO, Y. Wang, **Y. Zhang**, W. J. Chang, G.L. Lu, J. Z. Jiang, Y.C. Li, J. Liu, T.D. Hu, Journal of Physics and Chemistry of Solids, Volume 66, (2005), P1775-1778

8. Effects of Nitrogen on Oxygen Precipitation in Heavily Sb-doped Czochralski Silicon, Yu Xuegong, **Zhang Yuan**, Ma Xiangyang, Yang Deren, Journal of Semiconductor, Volume 51, (2004), P284-287

Fields of Study

Major Field: Materials Science and Engineering

Table of Contents

List of Tables

List of Figures

Chapter 1 Introduction of solid state impact welding

Welding is one of the important materials assembling technologies and it is widely applied to join materials for many applications, such as the construction of automobiles, aircraft, ships, gasoline pipeline, and spanning bridges. According to phase changes during the welding process, welding technologies can be divided into three categories. And they are the liquid state welding, solid/liquid state welding, and solid state welding, as shown in Figure 1.1 [1]. The liquid state welding has been developed and widely applied with long history, and it is also called fusion welding because the workpieces are melted by chemical or electric methods and the joints undergo melting and solidification process during welding. As a result, there is a heat affect zone (HAZ) after fusion welding. The solid/liquid state welding usually only melts the filler metals without melting the workpiece itself. The solid state welding does not require filler metal or flux and the process temperature is essentially lower than the melting point of the base materials. Therefore, there is no significant melting of the base metals or any resulting HAZ.
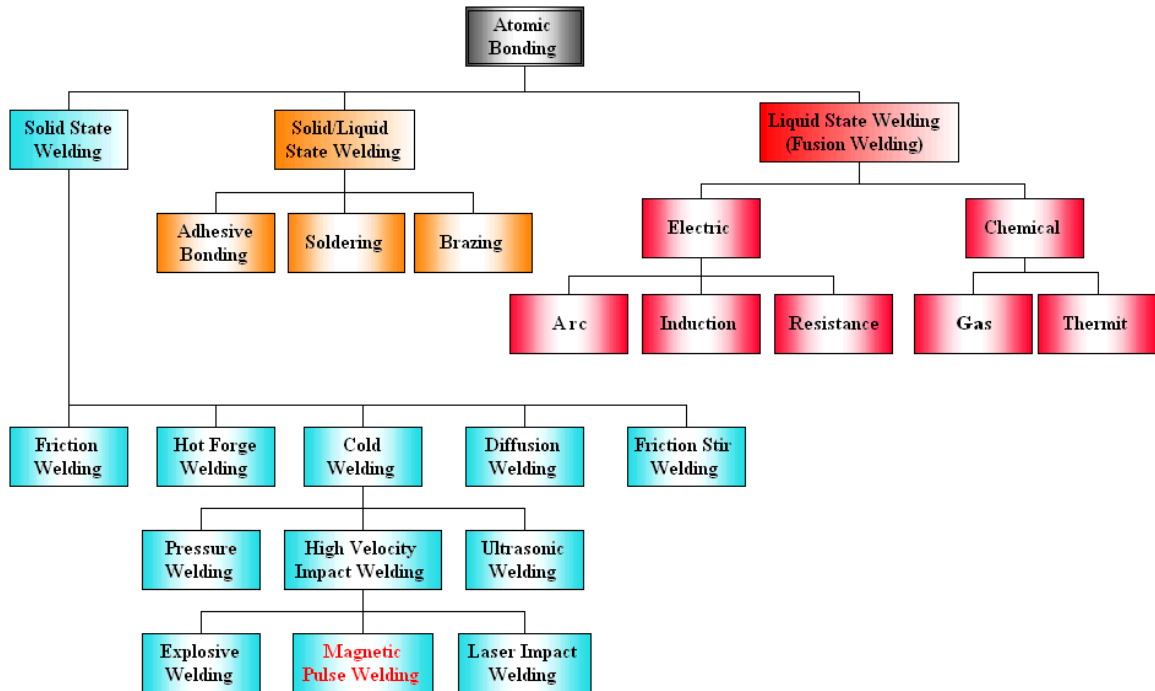
Figure 1.1 One category of welding technologies according to phase changes during welding process.

This research focuses on some of the solid state welding technologies, which have rapid development in recent four decades. The most outstanding feature of solid state welding is that there is no significant HAZ generated after welding. Hence, the being welded materials retain or improve their original properties, unlike fusion welding, which usually degrades the joint strength and causes residual stress with consequent cracking and corrosion issues. The other important advantage of solid state welding is that it can be used to weld both similar and dissimilar materials regardless of the property difference of the melting point, thermal expansion, and thermal conductivity.

The main objective of this research is to investigate the relationship between the joint strength and the welded interface microstructure evolution after high velocity impact welding for various material pairs. The dissertation includes ten chapters to stress above issues. Chapter 1 introduces solid state impact welding. Chapter 2 is a literature review based on previous research on impact welding process. It reviews three high velocity impact welding processes for different length scales, which are explosive welding (EXW), magnetic pulse welding (MPW) and laser impact welding (LIW). All of these three impact welding technologies share the same welding principles and have been established as fast, reliable, and cost-effective joining process. It is necessary to point out that the welding time for high velocity impact welding is extreme short, and it completes from microsecond to a few seconds. The goal is to review the development of the technology and to justify the current research to aim at the unsolved problems. Chapter 3 compares the joint interface structure and mechanical property from EXW, MPW and LIW at different length scales, ranging from hundred meters to millimeters scales. They were fabricated by different acceleration mechanisms. The following chapters stress on MPW process. MPW has been applied to weld many pairs of materials, including both similar and dissimilar materials. Chapter 4 introduced the MPW process parameters and the advanced instruments to measure them. Chapter 5 focuses on aluminum alloy 6061 similar material welding. Chapter 6 exhibits similar material welding on copper alloy 110. Chapter 7 and chapter 8 study the dissimilar materials welding on pair of copper alloy to aluminum alloy and pair of aluminum alloy to low carbon steel. Chapter 9 stresses on the finite element analysis (FEA) on MPW. The commercial FEA based software, LS-

DYNA®, was used for MPW because it is able to couple mechanical-thermal-electromagnetic simulation together for high velocity impact process. Chapter 10 summaries the research work and point out the possible future research directions.

Chapter 2 Literature review

2.1 Introduction of high velocity impact welding

There is a growing recognition that optimal lightweight structures for automobiles, aircraft and even bicycles are often created from multi-material assemblies. Joining dissimilar high-strength light alloys has therefore been of significant and growing interest. One of the most elegant ways to accomplish dissimilar metal welding is by impact welding. The outstanding advantage of impact welding is that it can minimize the formation of continuous intermetallic phases or HAZ while chemically bond dissimilar metals.

EXW, MPW, and LIW all share the same basic principle to join the metals together by impact-driven solid state welding but they are best applied at different length scales. Figure 2.1 schematically showed the range of three welds. EXW is well suited for large planar interfaces, up to meters in extent. As shown in Figure 2.1(a), a 90-meter-long explosive welded refinery column is transited on several rail cars. MPW can provide linear or circular welds, but equipment limits the total energy stored and this keeps weld

lengths to the order of meters or less, with typical widths of millimeters to centimeters. Figure 2.1(b) showed MPW welded tubes in which the outer diameter is about 20mm. LIW is a new process, just introduced in 2009 [2], that can create spot-like welds on the order of millimeters in diameter. Figure 2.1(c) showed a 3mm diameter spot welding of an aluminum tab on to an aluminum sheet.
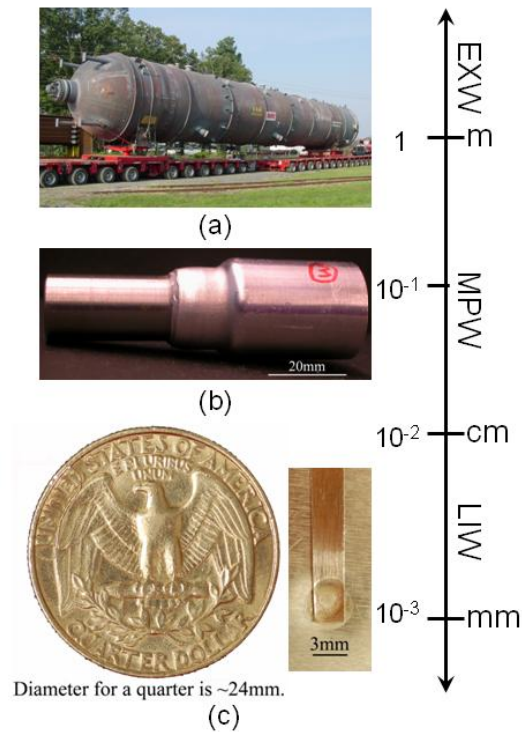
Figure 2.1 Illustration of EXW, MPW and LIW for different length scales. (a) Stainless steel clad to 387 alloyed steel by EXW to make refinery columns. (b) 1018 steel rod impact welded to AA 6063-O by MPW. (c) AA 1100 thin plates seam linear welding by LIW. The coin quarter is shown as a length scale reference for LIW.

2.1.1 History of High Velocity Impact Welding

Bahrani et al. (1967), Crossland (1982) and Blazynski (1983) studied EXW on a variety of metal combinations at large scales, and their research work indicated extensive industrial application [3-5]. Recently, MPW has been applied to both similar and dissimilar metals. For example, Tamaki and Kojima (1988) and Shribman et al. (2002) welded aluminum tubes together [6, 7]. Hokari et al. (1998) welded aluminum tube to copper tube, Aizawa et al. (2007) welded aluminum alloys to carbon steel sheet, Ben-Artzy et al. (2008)welded aluminum to magnesium, Hutchinson et al. (2009) welded copper plate to zirconium-based bulk metallic glass plate [8-11]. MPW has seen limited, but rapidly growing industrial application [12-14]. The commonly-welded length scale for MPW ranges from a few millimeters to several centimeters. Required energies are too great for larger structures and coupling of magnetic energy to the part becomes inefficient at much smaller lengths. Recently, Daehn and Lippold (2009) proposed LIW and developed for low temperature spot impact welding [2]. It is best applied to relatively thin samples about $200\,\mu m$ or less, and the weld regions are a few millimeters in diameter. One distinctive advantage of this approach is that it appears applicable to arbitrarily small foil thicknesses and length scales, and does not rely on the intrinsic electrical conductivity of the flyer. This makes the method well suited for the manufacture and assembly of micro-devices such as micro-electro-mechanical systems.

2.1.2 Explosive Welding

EXW is a solid state impact welding process that employs large quantities (usually a few centimeters thick) of high explosive to accelerate a flyer plate against a target plate. The method is well established for wide variety of materials with flat and large surface area. A schematic diagram in Figure 2.2 shows the basic components for EXW. The explosive detonation is normally initiated at a point or along a line, and the relative velocities, between the explosive detonation front velocity and the flyer plate downward velocity, set the contact angle upon impact [15]. Changing initial standoff (the distance between the flyer plate and the target plate) can change the impact velocity and angle. The collision takes place across the entire surface along an impact line that moves from the detonator and produces the plasma jet. The jet atomically removes the oxide and cleans the surface. The main process parameters for EXW include the surface finish and cleanliness, the placement of the detonator, the standoff distance, and the characteristics of the explosive used, particularly its detonation velocity and the pressure produced. These controlled variables are responsible for the impact velocity and impact angle that is developed [16].
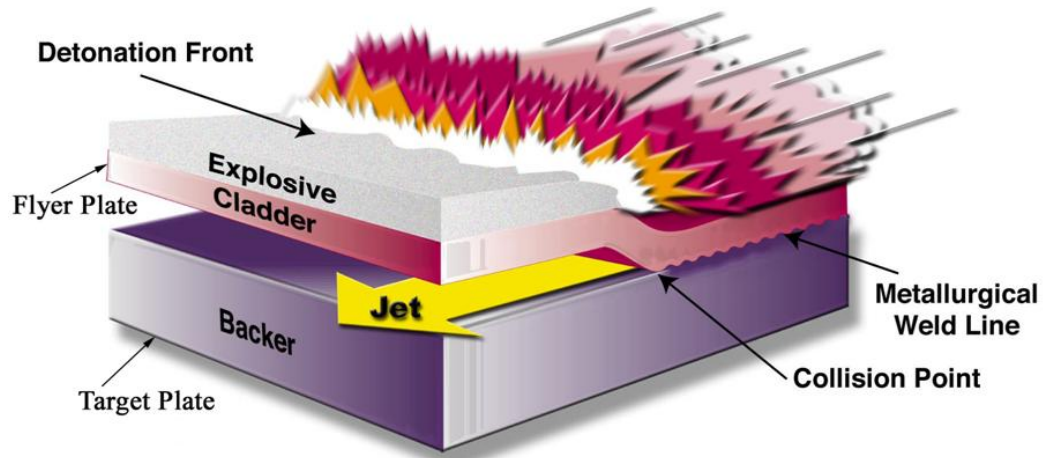
Figure 2.2 Schematic Diagram of EXW Process. Jet was generated from the collision point and propagated along the welded interface.

2.1.3 Magnetic Pulse Welding

MPW is closely analogous to EXW and it is necessary to have a slight impact angle to form a jet along the mating surface [9]. However, rather than explosives, it uses electromagnetic force to accelerate the flyer plate. Therefore, MPW can be safely and reproducibly used in production environments controlled by an electric power supply and the fine adjustment to parameters is straightforward. With proper design, the energy is fairly efficiently used for accelerating the flyer plate or tube rather than heating or melting the materials. The MPW system includes a capacitor bank, actuator, and workpieces. The capacitor bank simply consists of an inductance-capacitance circuit and an actuator of some impedance. Figure 2.3 shows one of the MPW actuators with the

workpieces. Once the current flows through the actuator, the overlap region of the flyer plate and target plate will be welded.

EM Actuator

Flyer Plate

Target Plate

Inbound Current

Outbound Current

Fixture
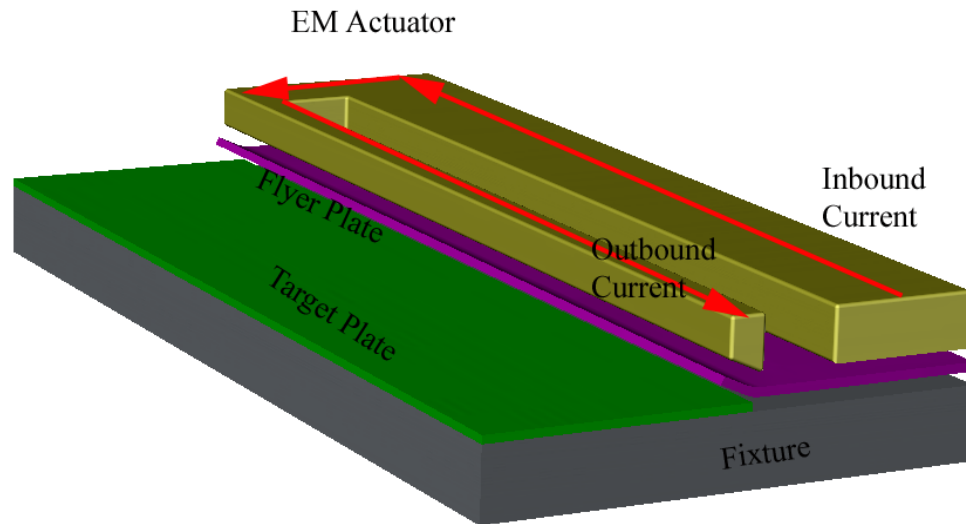
Figure 2.3 Schematic Diagram of MPW Process. Both the flyer plate and the target plate were supported by insulated layers with certain standoff distance between them. The Electromagnetic (EM) actuator was connected to capacitor bank. The arrows indicate the primary current flow direction in the actuator.

When capacitors are discharged, the current with high density flows through the conductive actuator, which is regarded as primary current. If there is a closed current path, the associated electromagnetic field induces a strong secondary current through the nearby metal workpiece (flyer plate). Therefore, the flyer plate carries current and stays

in the electromagnetic field. Because the primary current in the actuator and the secondary current in the flyer plate generally travel in opposite directions, their interactions result in a strong repulsive force, which is the Lorentz force. As shown in Figure 2.4, the flyer plate is repelled from the actuator and accelerates with sufficient velocity for impact welding. MPW uses an electromagnetic field and thus the flyer plate must be electrically conductive and plastically deformable, or coupled to a conductive driver. It is also suggested that the target plate should have a higher yield strength than the flyer plate to avoid extreme deformation of the target [17].
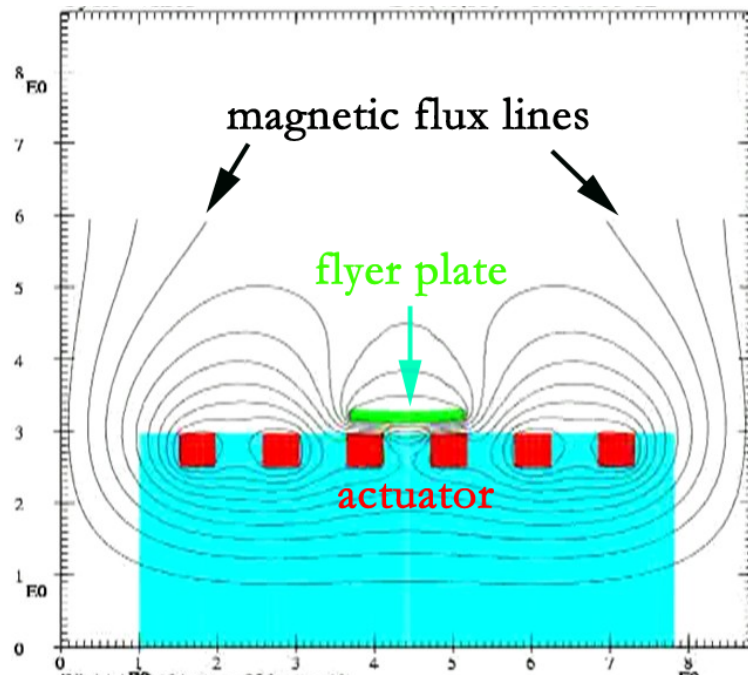
Figure 2.4 Illustration of magnetic flux lines during impact welding process.

Since 1969, MPW has been successfully applied for tube to tube impulse welding but typically required fairly high electrical energies to be stored in capacitor bank with typical values in the range of 20~100kJ [18]. With the recent development of MPW, the geometry of the welding workpiece could be cylindrically symmetrical [6] or asymmetrical [9, 19, 20]. Studies by Aizawa's group (2007) in Tokyo and Date's group (2007) in Mumbai have developed MPW seam linear welding [9, 20]. These methods tend to use much less energy than those for tube welding. For example, the reported energy to weld aluminum alloy plate about 1 mm in thickness to SPCC steel plate is only about 1.4kJ [9]. Very rapid rise times (time for actuator to reach maximum primary current) in the capacitor discharge circuit are largely responsible for this efficiency.

2.1.4   Laser Impact Welding

LIW technology has recently been proposed and demonstrated [2]. The initial experiments were carried out with a Continuum Powerlite II model 9000 Yttrium Aluminum Garnet (YAG) laser at Continuum Inc. in Santa Clara, CA on materials, including aluminum alloy 1100 and low carbon steel 1010. Both the aluminum to aluminum and aluminum to low carbon steel plates were successfully welded.

LIW is also caused by direct solid state impact welding of a flyer and target, both of which are at nominal ambient temperature and does not produce gross melting of the

12

metals which are joined. It is quite different from the laser beam welding which has liquid pool along the welding line. As shown in Figure 2.5, focused and pulsed laser beam shines through a transparent confinement component adjacent to the flyer. The flyer plate has an optically absorbent surface, in this case a darkened surface from a black permanent marker. The laser ablates the ink and the resulting plasma reacts against the confinement. The ablation generates a plasma-based pressure pulse between the confinement and the plate. This accelerates the flyer sheet over a time interval of a few nanoseconds. The plates collide with high velocity. The short duration of the high-pressure pulse causes the surfaces to co-deform, possibly forming a plasma jet. When the clean metal surfaces meet under pressure, metallurgical joining is accomplished. Figure 2.5 also shows that the impact angle and the standoff distance can be adjustable by simple geometric variations. The optical output energies for LIW are in the order of a few joules, as opposed to several or tens of kilojoules for MPW and megajoules for EXW. Accordingly, the sizes that can be bonded with each technique scale proportionately. LIW, it seems, can be tuned to produce impact welding for almost arbitrarily small foil thicknesses and length scales.
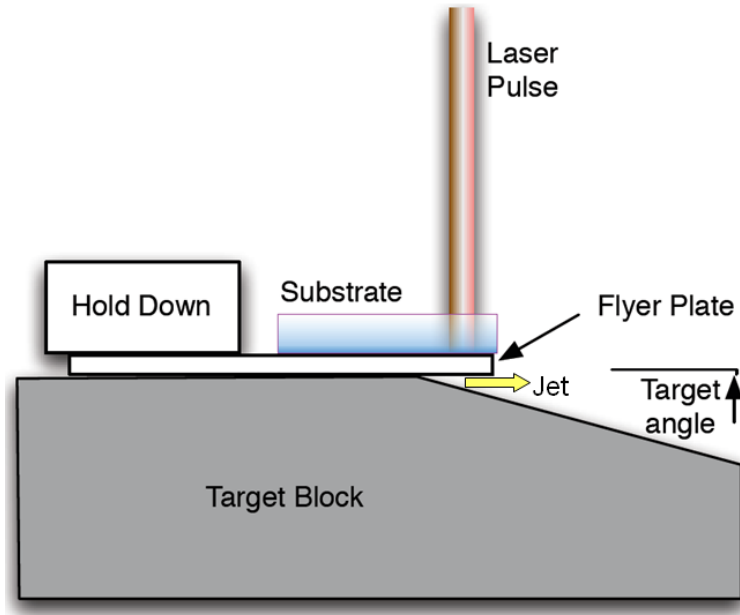
Figure 2.5 Schematic Diagram of LIW Process. The laser pulse ablates the substrate. Plasma jet was generated between flyer and target block. For plate to plate welding, the target plate can be attached to the block oblique surface and beneath the flyer plate with certain angle.

2. 2 Joining mechanisms for high velocity impact welding

Bahrani et al. (1967) and Ezra (1973) established the impact welding principle based on the jetting effect that allows atomically clean metal surfaces to join each other [3, 21]. When two plates collide with high velocity at a proper impact angle, a jet forms from the being deformed metals. At the collision point, the impact stress greatly exceeds the yield

14

stress. The jet propagates along the mating interface, cleans away the surface oxide layer and leaves two atomically clean surfaces. Simultaneously, these two virgin surfaces are under a large contact pressure. Bahrani et al. (1967) also pointed out that the impact pressure brings the surface atoms into direct contact, allowing a chemical or metallic bond of great strength [3]. Botros and Groves (1980) and Salem (1980) concluded that the jet is the essential for impact welding [22-24]. Palmer et al. (2006) found that the collision process often involves severe plastic deformation, mechanical alloying, possibly local melting with rapid solidification, and high strain rate induced fluid-like behavior [16]. Due to varied instabilities including Kelvin-Helmholtz instabilities [25, 26], the welded interface is often highly heterogeneous. The instability induces dynamical shear stress and shear strain flows along the welded interface, which is critical for the development of wave morphology. The previous experimental work has shown wave-like interface morphology. Based on the study from Bahrani et al. (1967) and Grignon et al. (2004), it is also known that the detailed interface morphology is critically dependent on the impact angle, impact velocity, properties of the materials, and geometry of the welded plates [3, 27]. The important parameters that determine the weld quality and interface microstructure are the impact velocity and impact angle [22, 23]. With a fixed impact angle, the impact velocity has a dominant effect. Excessive velocity can cause significant melting, leading to intermetallic formation, or it can produce brittle damage or spalling in the impacting plates. Insufficient impact velocity may not initiate the jet required to remove the surface oxide [28]. The typical estimates of the strain rate may be as high as $10^7 s^{-1}$ [6] produced from an impact velocity which is about 250~400m/s [9]. And the

15

following section discusses the possible joining mechanism in details.

2.2.1   Collision Jetting

Marya *et al*. [29] reported that the high collision velocity is sufficient to peel off the oxide layer on the surface of the colliding contact area. The metal is sprayed at the collision apex and forced outward with high velocity. The mixture of the peeled surface oxide and the surrounding gas form the jet. The jet propagates along the two colliding surface in a swirl motion and cleans the metal surface layer. The two clean metal surfaces were pushed into intimate contact by high pressure instantly, which leads to the metallurgical bonding across the interface. This jet assistant welding mechanism has been widely accepted but less research work has been conducted to capture the jet because it exists in a transient process. M. Kimichi (2007) at Edison Welding Institute used high speed camera to capture the welding process and the induced jetting was shown in Figure 2.6. After impact, the jet was sprayed and deposit on the surface near to the welded region. This deposition could be regarded as the indirect evidence of the jetting effect. Figure 2.7 is postulated by Bahrani *et al*. [3], and the schematic representation shows the wave interface development step by step. As long as the jetting is sufficient, the continuous wave interface can be formed. If there is insufficient jetting, the metal surfaces will result in little or no bonding. Since the jet modifies the metal surface during impact process, the surface roughness of the being welded workpiece did not obtained significant attention in

the previous research.
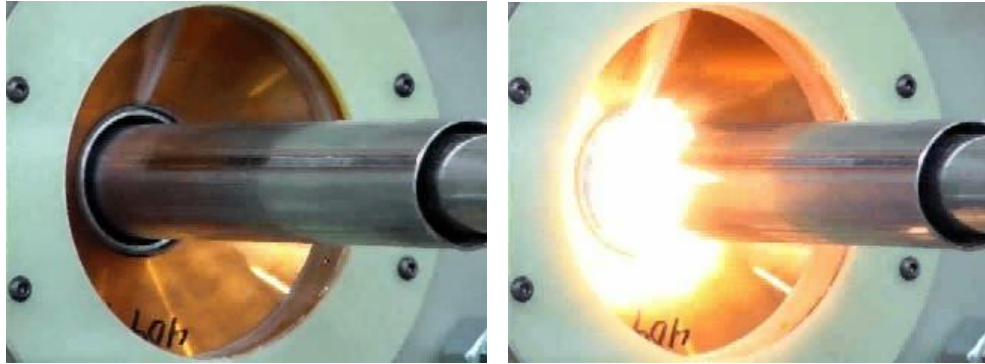
(a) Before impact welding   (b) During impact welding process

Figure 2. 6 High speed camera recorded jetting during MPW.
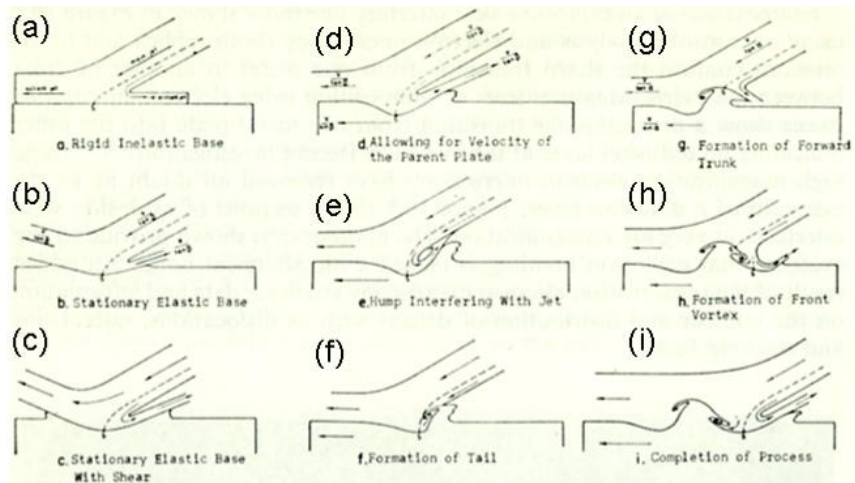
Figure 2.7 Development of wave interface during the explosive welding [3, 21]

The important conditions for jetting to form depend on the collision point velocity and the collision angle. At the critical collision angle, if the jetting exceeds the dynamic elastic limit of the materials, the plastic deformation occurs on the metal surface and then the bonding can be formed. If the collision point velocity is high enough at the critical collision angle, the interface temperature also rises and causes melting. Therefore, minuscule volumes of the interface materials can be liquefied. And the liquid phases subsequently flow around and eventually surround each other. Since the impact process is short, and the melting region is then rapidly quenched by surrounding materials and solidified into pocket at the swirl.

Based on previous research work on EXW, the high velocity impact welded interface morphology resulted from jet effect is classified into three types [7, 30-32]: (1) flat interface, (2) wave interface, (3) pocket type and continuous transition layer along the interface in the bond zone as shown in Figure 2.8. Among them, the wave interface is the most common one and this structure is formed by the collision jet. The jet is from an oblique collision controlled by plate velocity, pressure, collision angle and collision point velocity. The shown impact angles are 11º and 15º and the velocities are about 470~606m/s. And the flyer plates are 3mm thick stainless steel and 30mm thick base metals. It is important to point out that for thinner plate with low yield strength, the impact velocity and impact angle could be smaller than these reported values.

18

(a) Impact at 15 °, 470m/s, flat interface

(b) Impact at 11 °, 486m/s, wave interface
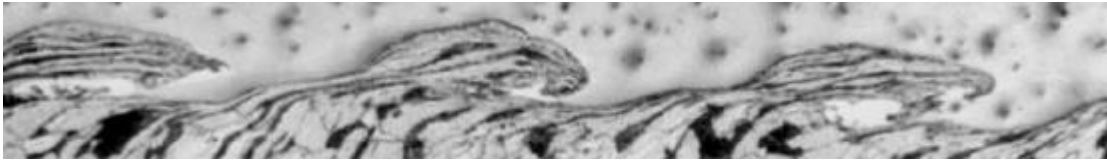
(c) Impact at 11 °, 606m/s, pocket type interface, wave pattern with vortex shedding

Figure 2.8 Interface morphology for various impact parameters [32]

2.2.2 Intermetallic Phase Formation

The binary phase diagrams for Al-Fe and Cu-Al system in Figure 2.9 show that directly welding these two dissimilar materials together will result in formation of intermetallic phases. And it is known that the intermetallic phases are usually around the cracking susceptible microstructures and could significantly influence the welding strength and toughness. Hence it is difficult to weld dissimilar materials together by fusion welding.
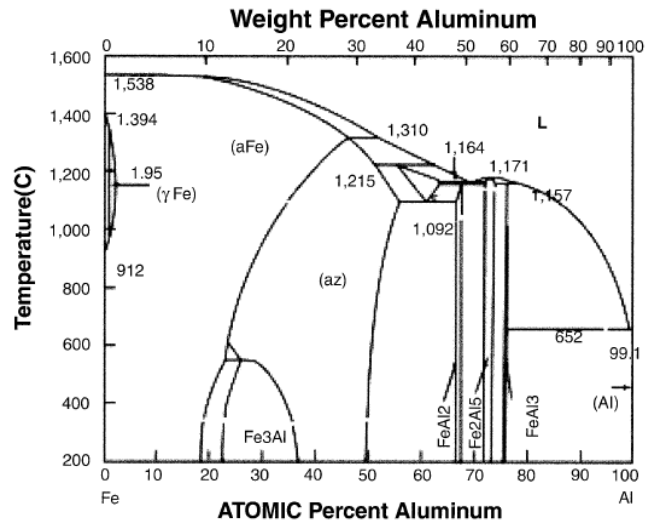
(a) Al-Fe phase diagram
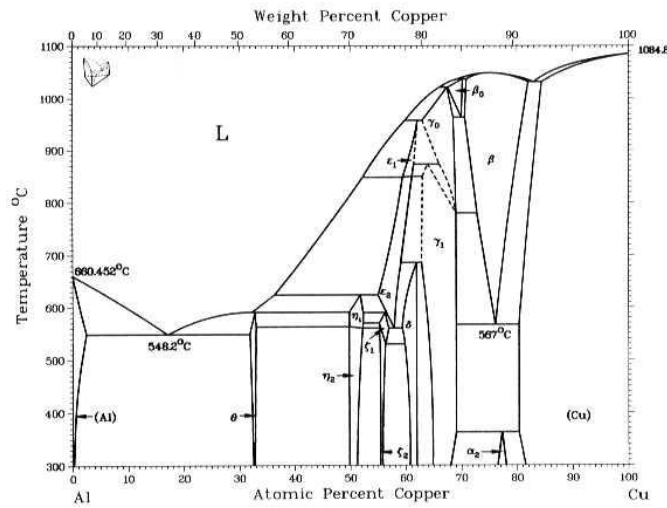
(b) Cu-Al phase diagram

Figure 2.9 Binary phase diagram for Al-Fe and Cu-Al.

Different from the fusion welding, MPW has very low heat input and rapid cooling rate.

Thefore the intermetallic phases could be entirely suppressed, or at least minimized, leading to the good mechanical and electrical properties. However, the intermetallic free joints are the ideal situation. In fact, some researchers have found that the intermetallic phases occur in the transition zone of MPW joints for aluminum, copper, magnesium and steel. For instance, Marya *et al*. [29, 33] found an intermetallic composition similar to gamma Cu-Al phase in the MPW joint of copper and aluminum as shown in Figure 2.10(a), which is a secondary electron (SE) image of the Cu-Al interface. They also believed that the presence of intermetallic phase supported the interfacial melting as well. Figure 2.10(b) is the interface layer made by MPW between AA 1050 and Mg AM50 alloys [34]. It suggested that new phase or metallic alloying might occur along the wave interface via different contrast on the backscattering electron (BSE) image.

(a)   (b)
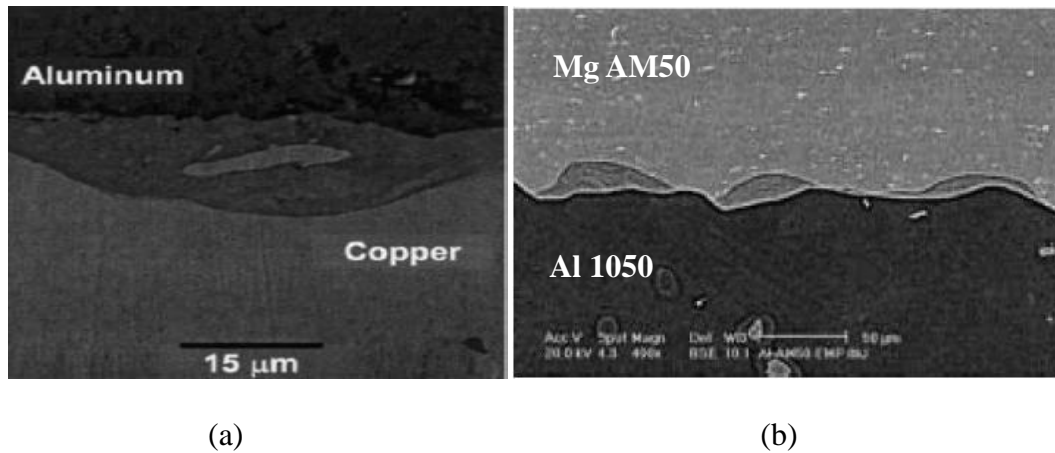
Figure 2.10 Dissimilar materials welded interface. (a) SE image on the Cu-Al MPW interface [33]. (b) BSE image on AA 1050 and Mg AM50 MPW joint [34].

In order to check intermetallic phase composition on the MPW joints, Stern *et al*. [34] carried out a composition profile study on AA 1050 and Mg alloy AM50 joints. It is known that AA 1050 matrix contains Al_3Fe spherical particle phase but no iron in the solid solution. However, after MPW, the iron was detected on the interface but negligible amount of Al_3Fe phase. The iron concentration across the interface layer is uniform; meanwhile, the magnesium and aluminum concentrations decrease. It indicates the extensive mixing and phase transformation occurred during MPW collision, which is possibly caused by the local melting and rapid cooling process. This phase transformation is also responsible for the mechanical property changes.

However, there is disagreement with the intermetallic phase formation. Based on the microstructure study of the ultrasonic bond for aluminum joint and Cu-Ti joint, Minoru *et al*. [35] believed that there is no other phases observed in the interface. The joining mechanism of this solid-state welding is only dependent on the mutual interatomic diffusion rather than any formation of intermetallic. This is because their X-ray diffraction patterns for joint specimens did not show the intermetallic features or any non-parent crystal structure. Such opposing results make this intermetallic formation mechanism not quite suitable for MPW. But according to the scanning electron microscopy (SEM) image, the different contrast levels indicate different atomic numbers. It apparently shows that certain mixture and intermetallic phases appear on the interface. There are two possible reasons for the X-ray failure on detecting the new phases. First, conventional X-ray diffraction technique may be limited in detecting the exceptionally

fine phases. Secondly, the intermetallic phase cannot form in some of the highly thermal conductive materials because of the rapid heat dispersion. For most engineering materials, such as aluminum, steel, copper and their alloys, MPW can be regarded as an adiabatic process. And the heat rapidly diffused into the workpiece without causing great amount of melting. However, the local melting and the resulting intermetallic phase along MPW joint interface suggested that intermetallic phase formation is also a possible joining mechanism for impact welding.

2.2.3   Local Melting and Solidification

Volobuev *et al.* (1972) and Stern (2002) [34, 36] assumed most of the kinetic energy from the flyer is converted into the amount of Joule heat on the contact welded interface during the collision. As a result, the local interface temperature increases. When the local temperature is above the melting temperature, local melting occurs on the welded surface. During interfacial melting, both the composition and the microstructure change within the transition zone. Examples of the molten layer formed in the MPW is shown in Figure 2.11(a) and (b) [34]. The welded materials in Figure 2.11(a) are AA 7075 with AA 7075, and those in Figure 2.11(b) are AA 1050 with mild steel. The molten layer is formed with the occasional occurrence wave type morphology. The laminar molten layer indicates the liquid/solid interface. This phase transformation also results in fine grained microstructure and the interfacial hardness increase. The size of the Vickers

microhardness indentations across interface in Figure 2.11(a) and (b) indicates the hardness increases across interface layer relative to the base metal [34]. Based on the experimental results, local melting and wetting are another possible joining mechanism for MPW joints.
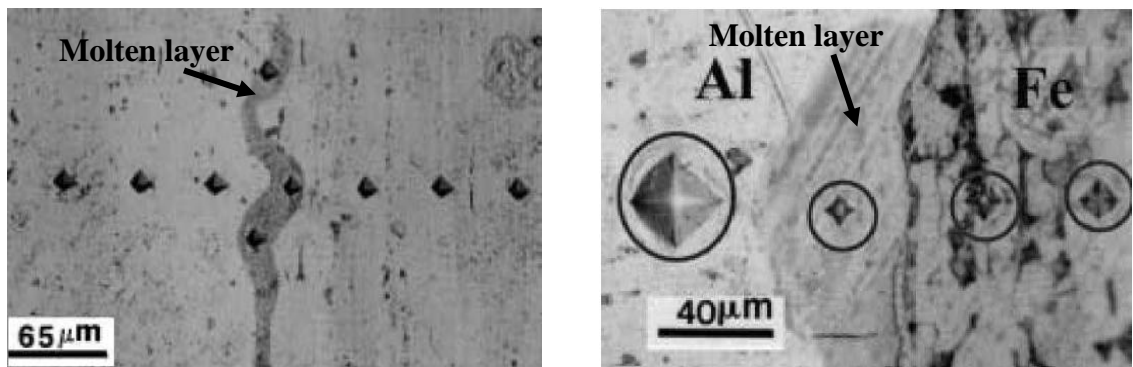
(a) Al 7075 MPW joints   (b) Al 1050 with mild steel MPW joint

Figure 2.11 Optical microscopy image of interface layer for MPW joints [34]

2.2.4   Interfacial Temperature Calculation Model

In order to investigate the melting phenomena, Marya *et al*. [29, 33] took into account the kinetic, thermal, and magnetic properties and built a model to calculate the interface temperature of MPW for aluminum and copper joints. They assumed that MPW is perfectly adiabatic within microseconds. Therefore, the collision kinetic energy is equal

to the enthalpy increase for the material with the lower melting temperature. In their experiment, aluminum was taken as the welded material, so that:

$$\frac{1}{2}(\rho_{Al}At_{Al})V_{Al}^2\eta = \rho_{Al}At_{IM}\Delta h \quad \text{Equation (2.1)}$$

in which, ρ, A, t, V, and η represent density, area, thickness, mean collision velocity and the efficiency factor respectively. The efficiency factor (η) was not estimated from any instrumental measurement but only an empirical value. The subscript 'IM' represents 'interfacial microconstituent'. Δh is the change of enthalpy, which can be derived from:

$$\Delta h = \int_{298K}^{T}C_p dT + (\Delta h_f + \int_{Tm}^{T}C_p dT)_{T\geq Tm} \quad \text{Equation (2.2)}$$

where T is the interface temperature; C_p is the temperature dependent specific heat. Once the enthalpy change is known, the interface temperature can be calculated. Since other variables in Equation (2.1) describe the material properties, only the velocity needs to be measured. Based on Newton's second law and the basic electromagnetic rules, the terminal collision velocity can be predicted by:

Electromagnetic pressure: $P = \dfrac{B^2}{2\mu}$ Equation (2.3)

Acceleration: $a = \dfrac{F}{m} = \dfrac{PA}{\rho At} = \dfrac{P}{\rho t} = \dfrac{B^2}{2\mu}\dfrac{1}{\rho t}$ Equation (2.4)

Mean collision velocity: $V = \dfrac{\sqrt{2ax}}{2} = \dfrac{B}{2}\sqrt{\dfrac{x}{\mu\rho t}}$ Equation (2.5)

where B is the magnetic field varying with time, μ is the permeability ($4\pi\times10^{-7}\,\text{Hm}^{-1}$),

ρ is workpiece density and t is the workpiece thickness. The collision velocity is also determined by the standoff distance x. Equation (2.5) shows that large magnetic field and separated distance or thin specimen can result in high mean collision velocity. Consequently, by plugging the mean collision velocity from Equation (2.5) into Equation (2.1) and (2.2), the interface temperature during MPW can be solved, as shown in Figure 2.12 for aluminum MPW joints. And it indicates that melting on aluminum could happen when collision velocity is larger than 170~180m/s [29]. Although the precise validation of this model is missing and the stored energy is neglecting in this model, it reveals that the enthalpy rise may increase the temperature beyond the melting point and result in local melting on the collision interface.
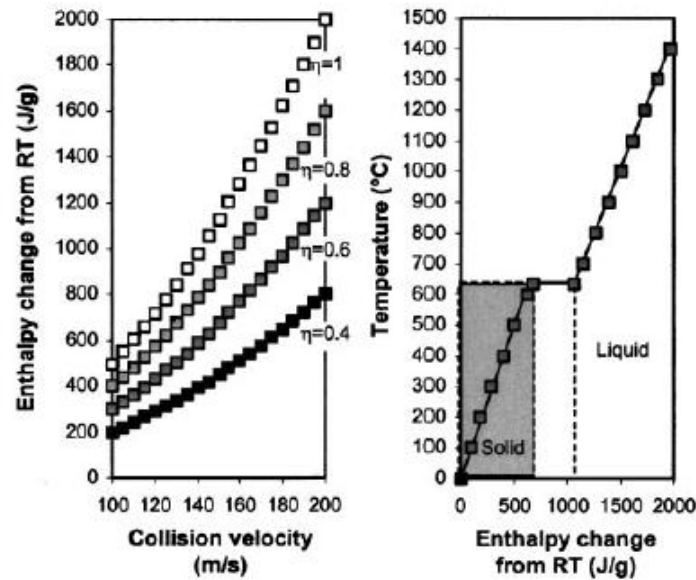
Figure 2.12 Enthalpy and temperature in aluminum as a function of collision velocity [29]

2.2.5 Interatomic Diffusion

Diffusion across the welded interface is the dominant process when the joints are subject to high temperature over a long time period. During MPW, two workpieces contact each other, and the limited atomic diffusion is possible across the welded interface [37, 38]. For example, based on the X-ray microanalysis, Minoru *et al*. [35] have reported that the interatomic diffusion occurs at the interface during the ultrasonic welding. From the intensity of X-ray, they [35] found out that the two different base metals diffused beyond the interface and into each side by 10~40μm. The across-interface concentration profiles for the base elements appear compensative as well. Therefore, they concluded that interatomic diffusion occurs between the two base metals during the welding process. Additionally, Wakemen and Hultgren *et al*. [39, 40] mentioned that for aluminum and copper MPW joints, the interface temperature significantly influences the diffusion of aluminum in copper, and the copper atoms also dissolve and diffuse in the aluminum matrix which is thermally activated by high temperature. Therefore, the interface temperature is the key variable that influences the diffusion-controlled joining mechanism. However, there are also some claims saying that the atomic diffusion cannot happen because of the less diffusion time in MPW, and the composition changes are the result of the local melting accompanied by extensive mixing [29, 34]. Additionally, the interface temperature changes have not been experimentally measured.

2.2.6   Summary for Joining Mechanisms

For similar and dissimilar metal pairs, the observed joint interface morphology including flat interface, wave interface, pocket-type wave interface, and the following possible joining mechanisms have been discussed:

(1) Joints as a result of jet assistant collision process.

(2) Joints as a result of intermetallic phase formation, which is inside the thin molten layer between the base metal pairs.

(3) Joints as a result of local melting and rapid solidification.

(4) Joints as a result of atomic diffusion at locally high interface temperature.

(5) Joints as a result of extensive mechanical alloying.

Since the discussed joining mechanisms are related to each other, there can be one of the above mechanisms or a combination of them valid for MPW. In other words, the elevated temperature may cause local melting, which can speed the intermetallic phase formation and the wave interface generation. The phenomena may be accompanied by interatomic diffusion and solution mixing with intensive plastic deformation as well. It is necessary to point out that the impact condition has significant effect on the joining mechanism, which could be studied carefully by simulation.

2.3 Material behavior after high velocity impact

It is very important to understand the main mechanical properties of MPW joints, such as hardness, tensile strength, and fatigue strength. However, few research works have been performed and there is still lack of a systematic knowledge on the mechanical property of MPW joints. This section reviews the tensile property and shock hardening.

2.3.1   Tensile Property

There are few reports on the tensile properties of MPW joints and the details of the sample preparation are not always given. Therefore, it is hard to compare the tensile properties for different specimens. From the existing research results, it is reported that during tensile test, the failure occurs outside the welded area either on the weaker base metal [41, 42] or on the point where the thickness suddenly changes [7]. It is also found that the maximum tensile strength is nearly the same as the base metals [41, 42]. Furthermore, it is noteworthy that the condition and the treatment of the materials have critical effect on the strength of the welded joint [43, 44]. For example, a larger loss in tensile strength and elongation will be seen, if the base metals are pre-welding heat treated [45, 46].

2.3.2 Shock Hardening

The most remarkable mechanical property change for MPW joint is the hardness increasing of the welded zone. Some results show that good MPW joint can be produced with hardness approximately equal to or even larger than that of the base metals [7, 47].

MPW is a pressure-associated impact welding process, and the joint is made from the collision between the flyer and the target. Therefore, it can be regarded as that the workpieces are deformed by a plane shock wave load during MPW, and this deformation includes surface erosion, shock hardening and deformation twinning [47]. The shock load generates the deformation twins at variant strain rate in the order of $10^5 \sim 10^8$ s^{-1} [48]. The deformation twins have been observed and intensively studied on pure iron, steels, nickel, copper, and aluminum alloys under shock load [47-57]. It is found that copper shocked by plane wave load exhibits strong preference for deformation twins [58-60]. Based on experimental results, Murr *et al*. [61] found that the shocked metal has higher work-hardening coefficient than the as-received metal and they thought high strain rate favors twinning formation. They also accounted twinning subdivides the grains and increases the flow stress of the material. Therefore, the deformation twins could contribute to additional hardness of the MPW joints when the strain rate reaches certain level.

2.3.3 Deformation Twins

Deformation has two competing mechanisms, twinning, and slip. Normally, dislocation movement is slipping rather than twinning. Embury *et al*. [62] postulated two basic conditions for the deformation twins formation: (a) dominant slip system changes, and (b) applied shear stress reaching to the critical shear stress level where twinning occurs. Usually, twinning happens on the crystallographic orientation, along which the resolved shear stress can decrease the external shear stress or reduce the overall internal energy [54]. It is also known that the activation energy for twinning is high. Thus in quasi-static deformation process, twinning does not often appear. However at high strain rate or shock load pressure, twinning is easier to happen for both metals and alloys [59, 63-67].

2.3.4 Stacking Fault Energy Effect on Twinning

The other key factor influencing the twinning formation is the stacking fault energy (SFE), as shown in Table 2.1. It is reported that low SFE favors microtwins (twinning in miroscale), while high SFE favors microbands for the same shock wave geometry and deformation conditions [54]. However, for nickel, which has high SFE, the deformation microtwins have been observed with shock loading [59, 68] rather than microbands. This is because the shocked microstructure is strongly dependent on the shock wave geometry and the dislocation movement. Esquivel *et al*. [54] summarized the relationship between

SFE and microstructure as: (a) for high SFE metal, by cratering shock wave, the glide or cross slip of the primary and the secondary dislocation result in microband structure; while by planar shock wave, only the primary dislocation glides and forms microtwin; (b) for the low SFE metal, mircotwin is the dominant structure; (c) for the intermediate SFE metal, it will be the mixture of the microtwin and microband. Since the shock wave is regarded as planar shock in MPW, the most possible deformation structure is twinning. When the plane shock pressure is beyond the critical twinning pressure, twinning occurs. The critical twinning pressure increases with increasing SFE [69-71]. Generally speaking, the relationship between the SFE and the deformation twins is that low SFE makes the dislocation hard to cross slip, and more likely to form twinning. As a result, both the dislocation density and the shock strengthening are low for low SFE metal [48, 55], vice versa.

Table 2.1 SFE for different FCC metals at 25 °C [72-75]

Alloy or Metal	Brass	Stainless Steel	Cu	Ni	Al
SFE (mJ/m^2)	10	20	50	130	166

2.3.5 Strain Rate Effect on Twinning

The hypervelocity deformation happens in the impact welding process and the corresponding strain rate is also very high. According to Armstrong and Worthington [56, 76], the shear stress for twinning formation is also dependent on temperature (T) and strain rate($\dot{\varepsilon}$), which can be expressed as:

$$\sigma_T = \sigma_0 + m \left(\frac{Gb}{C_1}\right)^{1/2} \left[\frac{U^*}{RT} \ln \frac{\dot{\varepsilon}}{\dot{\varepsilon}_0}\right]^{1/q} d^{-1/2} = \sigma_0 + k_T d^{-1/2} \quad \text{Equation (2.6)}$$

where σ_0 is the friction stress, m is a orientation factor, G is shear modulus, b is Burgers vector, C_1 is material constant, U^* is the normalized activation energy for twinning, R is gas constant, $\dot{\varepsilon}_0$ is reference strain rate, and d is the average grain size. The value of the exponent 'q' varies between 4 and 8. In Equation (2.6), the term $\left[\frac{U^*}{RT} \ln \frac{\dot{\varepsilon}}{\dot{\varepsilon}_0}\right]^{1/q}$ shows how the shear stress is related to temperature and strain rate. If the strain rate increases from 10^{-2} to 10^3, this term will change by 10~60% [61]. Therefore, the strain rate generated by impact significantly influences the twinning formation on the joints.

Lastly, twinning is not the only possible reason for the shock hardening. The pressure-induced lattice strain [77], and high residual concentration of point defects [78] produced by fast moving dislocation, may also lead to hardness increases.

2.3.6   Summary of Material Behavior

During high velocity impact welding process, the materials are subject to impact pressure and high strain rate deformation, which is similar to the shock load deformation. The MPW joint has significant impact on the hardness increase, as well as the ductility of the joint [43, 44]. The deformation twins and the increase dislocation density could be the possible reasons to explain the hardness increase.

2.4 Materials microstructure evolution of impact joint

The MPW joint mechanical properties are largely dependent on the microstructure evolution, the welding defects, base metal composition, and metallurgical states [79]. This section will discuss the microstructure evolution from three aspects: the intermetallic phase formation, the grain refinement, and the dislocation density increase on the interface of the high velocity impact joints.

From the standpoint of the microstructure evolution, the mechanical property changes are classified into three characterizations: (a) for similar materials welding, the fine grained microstructure created along the welded interface; (b) for dissimilar materials welding, besides of the fine grained microstructure, the stable or metastable intermetallic phases also lead to the hardness increase of the joint interface; (c) for both similar and dissimilar

materials welding, the high velocity collision, the jetting effect, and the high strain rate effect, can change the microstructure and the mechanical property of the mating interface.

Note that due to the lack of information in the literature regarding the MPW joints microstructure evolution, this section will also review the analogous shock deformed microstructures.

2.4.1 Effect of Intermetallic Phase

As mentioned before, intermetallic compounds are found in the dissimilar materials MPW joints [29, 34, 80]. Some intermetallic phases have higher hardness than the base metal. These intermetallic phases are formed by the solute redistribution in the local melting and consequent rapid solidification process. To date the aluminum alloys combined with mild steel, magnesium alloy and copper have been reported to weld by MPW. It is found that the metastable compound $FeAl_6$ [34, 80] appears on the interface for AA 1050 with mild steel MPW joints, and $FeAl_6$ was responsible for the increase in the interface layer hardness. For the joint of AA 1050 with Mg alloy, it is also found that interface composition (in at %) varies between Al-45Mg and Al-55Mg, and the interface Vickers microhardness is 480 ± 110 kgmm^{-2}, which is much higher than that of the base metals: AA 1050 (45 ± 2 kgmm^{-2}) and Mg (47 ± 3 kgmm^{-2}) [34]. For aluminum and copper joint, Marya et al. [29, 33] found that the intermetallic $\gamma_1(Cu_2Al)$ phase increased the

interfacial hardness.

2.4.2 Effect of Grain Refinement

The joint interface is subject to a rapid solidification process, during which only short range diffusion could occur and result in fine grained structure on the interface of MPW joints. Since the MPW joint is subject to impact pressure, the existing grains near the mating interface are extensively elongated along the welding direction [38, 81]. The effective grain refinement and grain elongation can significantly influence the hardening [34, 59, 82, 83]. Stern *et al*. [34] studied the typical transition zone in ferritic stainless steel MPW joints and found that the grain size is less than 0.5μm on the interface of the ferrite stainless steel MPW joints, and the totally fine grained transition zone is in a width of 40μm adjacent to the interface.

According to Hall-Petch Equation $\sigma_y = \sigma_0 + kd^{-\frac{1}{2}}$, small grain size leads to larger yield stress. This relationship is also approved by experimental results from the high velocity impact joint. It is also reported [84] that during cooling process, fine grains are able to solve the local concentrated stresses. However, there are only limited studies of grain size effect and grain orientation effect on the mechanical properties of the MPW joints interface from previous research work.

Furthermore, the relationship between grain size and joint solidification cracking has not been confirmed yet. There is opposing points of view that the fine grains are more susceptible to cracking. Compared with the solidification cracking susceptibility for both MPW joints and the fusion joints, it is found that in the fast welding process, the grain size could be fine but these fine grains are regarded more susceptible to solidification cracking [85-88], because the residual liquid along the grain boundaries may form liquid-film and cause the strain concentration [43]. Therefore, the refined grain effect plays a two-sided role on the mechanical properties at various cooling rates. Considering about the MPW joint, because of the low heat input, less liquid phase and rapid cooling rate, the fine grained structure can strengthen them rather than reduce their resistance to cracking.

2.4.3   Effect of Dislocation Density

Transmission electron microscopy (TEM) observation shows that high dislocation density and twinning appear in the shock loaded metals comparing to the as-received materials. MPW welded interface has higher dislocation density. It has been reported that the residual dislocation densities observed by TEM near to the welded zone are up to the order of $10^{15} \sim 10^{16}$ m^{-2} [38, 89-91], which is much larger than the quasi-static loading deformation [48]. The recrystallization and recovery occur on both sides of the high dislocation density regions [34, 38, 92]. Therefore, the dislocation density change also influences the MPW joint properties.

As shown in Figure 2.13, Rohatgi *et al*. [55] took typical TEM images of the twinned region from the shock deformed Cu-4wt%Al. The large dislocation density region is the dark region in the bright field (BF) TEM image. Murr *et al*. [61] found that the dislocation density is a strain-rate induced saturation. The dislocation density and dislocation interaction rise rapidly with the strain-rate increasing, especially for FCC materials. Therefore, during the MPW process, the materials also undergo high strain rate deformation, and the dislocation density is expected to increase on the MPW joints in the same manner.
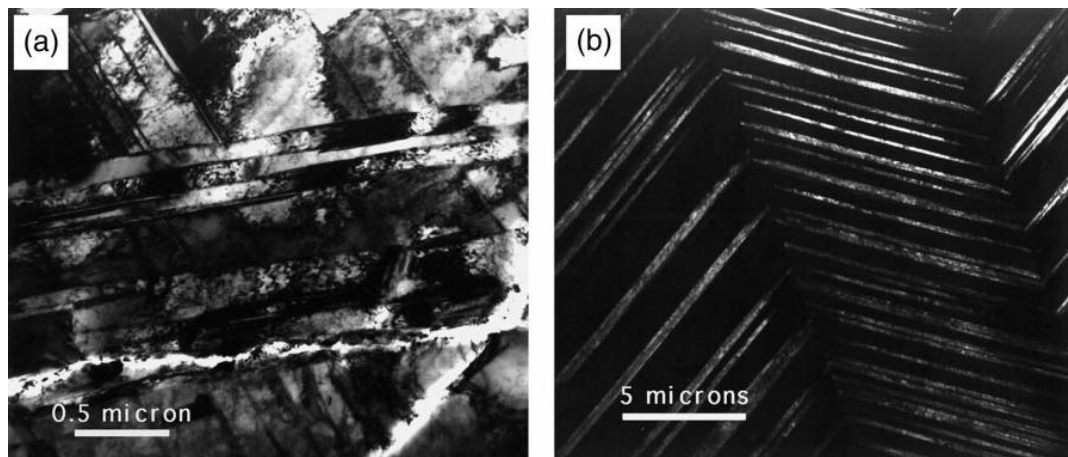
(a) TEM BF image (35GPa)   (b) TEM DF image (10Gpa)

Figure 2.13 TEM images showing large dislocation density and microtwins in Cu-4wt%Al [55].

2.4.4　Summary of Microstructure Evolution

As a summary, the mechanical property changes in the transition zone of MPW joint depend on the phase transformation and microstructure evolution. From the viewpoint of the phase transformation, the similar base metal welds are hardened by fine grains and the dissimilar base metal welds are influenced by the creation of stable or metastable intermetallic phases, together with the fine grained microstructure of the interface layer. From the microstructure viewpoint, the mechanical property changes are commonly attributed to the higher effective dislocation densities, the grain refinement, and the shock induced deformation, such as the deformation twins and the stacking fault. All of the effects can be simply summarized into linear relationship written into Equation (2.8) [55, 59]:

$$\sigma = \sigma_0 + K\rho^{1/2} + K'd^{-1/2} + K''\Delta^{-1/2} \text{ Equation (2.8)}$$

where σ_0 is related to the yield strength of pre-MPW materials, ρ is the dislocation density, d is the average grain size, Δ is the space between the deformation twinning. The coefficients K, K', and K'' are the experimentally determined constants.

2.5 Research motivation and unsolved problems

Based on the literature study of the high velocity impact welding, which includes EXW

and MPW, the current research progress can be put into three categories: (1) few facts and statements that are broadly supported and for which there is almost no dispute; (2) a number of ideas that are widely believed, but not truly proven; and (3) there are some aspects of the process that appear to be very poorly understood and relatively uninvestigated. In this section the relevant ideas on this technology area will be grouped into three classes from well-proven ideas to aspects in desperate need of study. Note that these groupings are somewhat arbitrary and one could argue that some topics belong in another category, but the overall classification has utility in framing the overall understanding.

2.5.1   Well-Supported Statements

1) EXW is a routinely-practiced commercial operation that is used to clad metal and for other operations. It has been well-studied (mostly between the 1950's and 1980's) and has been the subject of many academic papers and books [4, 21, 93-108]. Authors in that area have emphasized that effective welding requires a proper combination of impact velocity and impact angle between the flyer plate and target plate.

2) In EXW it is most typical that large areas of plate are accelerated to high velocities about 1000 m/s [32] and the flyer plates are typically quite thick and bonding takes place over the entire area of the plate. In MPW, velocities are typically less than 500 m/s [109];

the flyers are commonly thin, about 1mm thick, and only one edge is accelerated, as shown in Figure 2.14(b). Thus, the velocities and absolute energies are typically much less than in EXW. As a result, the MPW process seems to be more prone to problems related to removing surface contamination.

(a) EXW   (b) MPW
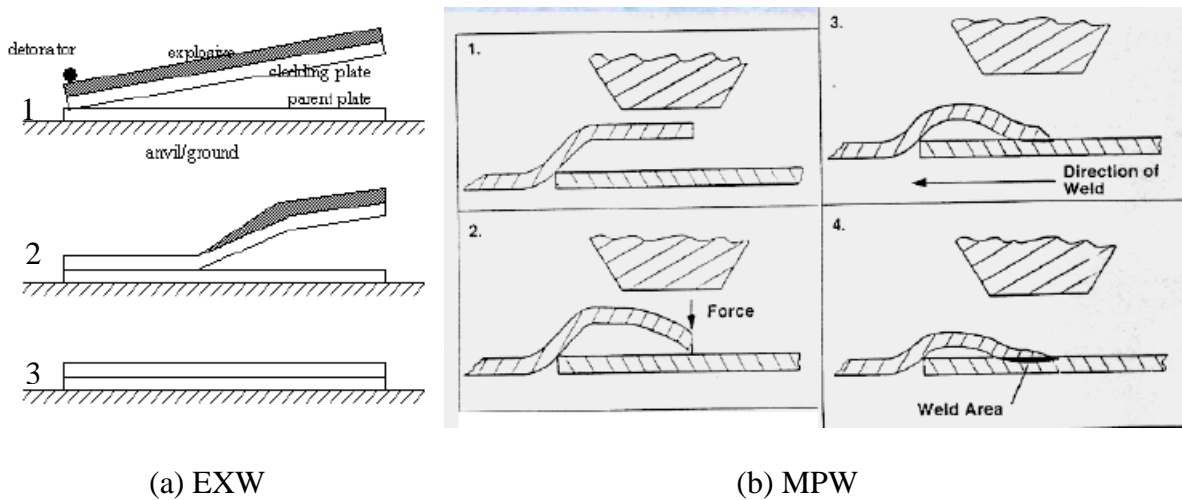
Figure 2.14 Experimental set-ups for impact welding[110]

3) It is widely accept that solid state welding is possible and has been demonstrated when two clean (i.e., free from oxides, oils, etc.) metallic surfaces touch one another [3, 4, 30, 32, 38, 39, 111, 112]. This solid state joining mechanism very likely has a key role in impact welding. There is good evidence that a solid state jet of material can form at the impact point and remove the oxide from the metal surfaces [4, 32], allowing the atoms of

41

two work pieces approach to inter atomic distances and forming metallic bonding on contact.

4) Significant heat is developed on impact between the flyer and base. Often this heat is sufficient to cause local melting [34, 111, 113, 114]. This may be done in a manner that melting is locally heterogeneous and then bond is spatially heterogeneous along the interface.

5) The morphology of the weld interface can vary widely depending upon the impact angle and velocity. Mousavi and Al-Hassani [32, 115-117] have shown this experimentally and with theories based on AUTODYN simulation. The interface morphology can range from straight to very wavy with strong vortex areas as shown in Figures 2.8 [34]. The transition from a planar to a wave interface appears to be related to an increase in the plastic strain and shear stress. Higher plastic strain and shear stress were seen in the cases where wave interfaces wear formed [32].

6) In the impact region in MPW and EXW, there is a region of the metal that has clearly suffered high levels of plastic deformation with high strain rate. In these regions the material microstructure is usually quite refined and significantly harder than the base metal. It is very likely that the high strain rate and possible shock conditions give higher rates of strain hardening than that would be produced at low strain rates. Local heating may also introduce recovery or recrystallization in this region.

7) Intermetallics are a common feature in dissimilar metal welds [29, 33-35, 42]. Due to the typically poor fracture toughness of intermetallic phases, continuous intermetallics result in poor joint performance.

2.5.2 Supported but Unproven Ideas

1) Several detailed models have been offered that relate to the development of jets [3, 4, 30, 32, 38, 39, 111, 112], unstable flow [118], plastic strain [33], new surface generation [34, 35] and heat generation at the interface [3, 4, 119]. Most of this work has been done before 1980 and is reliant on closed-form techniques. The early models tend to focus on jetting and plastic deformation in the immediate vicinity of the impact zone, and there is also careful consideration to the notion that the impact conditions may be unstable and this can result in wave formation upon impact.

1a) There is some disagreement what sets the interface wave length and amplitude. As described by Robinson [120], one class of models on, flow instability attributes to the unstable nature of the metal jet that forms and crashes as the contact point moves forward. There is also evidence that the wavelength is set by the transit time for reflected waves to come from the back side of the base metal. Wronka and Jaramillo have shown [121, 122] that for joining a tube onto a bar by MPW with an off-center hole, the wavelength of the interface wave is smaller where the hole is closer to the base surface, which supports the

idea reflected waves are important.

1b) The spatial and temporal temperature distribution during interface generation is of key importance in impact welding. This determines if melting will occur, if intermetallics will form and how much recovery or recrystallization might take place immediately after bonding. Coupled with the understanding of the interface waviness, it determines if intermetallic formation would be continuous or discontinuous, and this has a clear tie to the mechanical behavior of the joint. A number of ideas have been used to form equations to estimate temperature rise at the interface. These include estimating deformation at impact [123], shearing of the jet [102], wave formation [100, 124] and material Eddy currents at impact [125]. One important limitation of all these closed-form models is that the thickness over which energy is dissipated must be chosen as an assumption. This is length difficult to bound and has a leading role in determining what the peak temperatures are and therefore if melting, for example, will take place.

1c) It has been suggested that if the velocity of the contact point exceeds a critical speed the interface will become planar [126] because the volume trapped jet increases and suppresses the formation of waves. This suggestion seems reasonable based on this argument, also Bahrani and Black [3] reported the interface wavelength changes gradually when keep the impact angle constant varying the impact velocity or keep the velocity and change the angle.

2) Numerical solid mechanics methods show much promise for modeling the plasticity, heat generation, instability, and phase formation in the process. The research work by Mousavi [32] and Panshikar [127], which used AUTODYN to model the oblique impact, wave interfaces, and jetting phenomena. But these studies have not been practically detailed. For example, the effects of mesh refinement and the solidification have not been studied. And Nemat-Nasser S. *et al.* [128] studied the constitutive parameters of elasto-visco-plastic flow of metals, and they also established constitutive models for large scale computational simulation of high strain rate phenomena. Their finite element simulations on PRONTO-2D were compared with high speed photographic recorded deformation and led to fine tuning of the parameters.

3) While it is clear that in dissimilar metal impact, welding intermetallics may form in a continuous or discontinuous manner, the mechanism by which they form has been the subject of some debate. Sergeeva [35, 37, 38] suggested that in the Cu-Al case intermetallics form in the solid state by diffusion, however more recent studies [29, 33, 34] have argued convincingly that at least partial melting is required for intermetallic phase formation. It is important to note that intermetallic formation is often exothermic and this can produce heat that further enhances intermetallic phase formation. According to solid state diffusion theory, the diffusion distance is proportional to the square root of the product of diffusion coefficient and diffusion time. Taking the maximum diffusion coefficient for metals at the melting point, which is approximately $10^{-5} \text{cm}^2\text{s}^{-1}$ [129] and

MPW impact process lasts less than one second, taking it as 10^{-5}s, the maximum available diffusion layer thickness on the interface is less than 0.1μm, which is much less than the observed 40~60μm intermetallic layer. Therefore, we believe the intermetallic phase layer is not formed by diffusion.

2.5.3 Unfounded or Unresolved Notions

1) While it is clear that impact angle and velocity lead directly to the structure and properties of the impact-welded interface, launch speeds and angles have not yet been measured in MPW, as they have in EXW. In EXW, it has been possible to measure the impact velocity and these bonding conditions have been correlated with interface structure. This has been possible, in large part, because steady state conditions exist over the large areas of the bonded plates. MPW is different in two very important ways: the velocities and energies are much lower, and there is no 'steady-state' over the distance of the weld. At present, it seems clear that if the impact velocity and angle are appropriate, metallurgical bonding is possible. However, the literature gives no clear guidance on what the 'optimal' conditions should be. It is also likely that the thickness of the flyer and the base metal may play a role, as these also affect impact conditions, the time the interface spends in compression and the time between impact and wave reflection.

2) Accepted and complete models of the impact welding process are lacking and likely to

be unavailable for some time. The process is very complex involving high strain rates, large local strains (where constitutive data is not available) and the process involves huge gradients of strain, strain rate, temperature, and pressure. These all make numerical modeling very difficult. One particular complication is the impact interface acts like a singularity where temperature is generated and shock waves may be initiated. Many models assume that thermal energy is introduced over a thickness of $50\,\mu m$ or so. For example, Ben-Artzy [110] calculated the total energy to completely melt $50\,\mu m$ intermetallic layer is about 750J/gr. This is an arbitrary length scale that is chosen for convenience. Peak temperatures estimation depends strongly on this assumption. Also, numerical models need elements smaller than this length at the impact zone and this has not been done as yet.

3) The evolution of the length scales in interface wave formation is also not understood and plagued with the same difficulties described above.

4) Lastly it is very likely that there are areas where true solid state bonding can take place by oxide stripped metal surfaces coming into contact with one another under pressure as in the ultrasonic welding [35]. However how the oxide is stripped with a jet and how it becomes fractured and deposited in the joint is unclear.

2.5.4 Proposed Research Work

The greatest utility of impact welding is in enabling the metallurgical joining of dissimilar metals, because traditional fusion welding will almost always form large intermetallic zones that render fusion joints brittle and unreliable. This research attempted to study both the similar and dissimilar materials joining on aluminum alloy, copper alloy, and low carbon steel. Both experimental and numerical tools will be developed to understand the impact conditions, such as the velocity, angle, materials properties and component dimensions. The resulting joint strength and the interface microstructure will be studied to reveal the joining mechanism and the strengthening mechanism. The numerical tool based on LS-DYNA® simulation will be developed with tightly coupling of electromagnetic, thermal, and mechanical properties.

Chapter 3 High velocity impact welding on different length scales

3.1 Abstract

This chapter provides a comparative study of the interface structures and the interface microhardness on both similar and dissimilar material joints. The joints were fabricated by three impact welding processes at different length scale and they are EXW, MPW and LIW, as described in section 2.1. They share the physical principle that general impact-driven welding can be carried out by oblique impact but are used at different length scales from meters to sub-millimeter. The different length scales require different kinds of systems to drive the process, and the scales themselves can give different weld morphologies. Metallographic analysis on cross sections shows a wave interface morphology which is likely the result of an instability associated with jetting, which scours the surfaces clean during impact. The normalized period and amplitude of the undulations increase with increasing impact energy density. Microhardness testing results show the impact welded interface has a much greater hardness than the base metals. This can lead to weldments that have strengths equal to or greater than that of the weakest base material.

3.2 Introduction

This chapter presents three types of impact welding technologies. They are EXW, MPW, and LIW, which are regarded as fast, reliable and cost-effective welding process. They all share the same basic principle to join the metals together by impact driven solid state welding but these are best applied at different length scales. EXW is well suited for large planar interfaces, up to meters in extent. MPW can provide linear or circular welds, but equipment limits the total energy stored and this keeps weld lengths to the order of meters or less, with typical widths of millimeters to centimeters. LIW is a new process, which can create spot-like welds on the order of millimeters in diameter. This chapter examines the processes and characteristic of the welded interfaces for EWX, MPW and LIW joints. The studied materials include aluminum alloy, carbon steel and copper alloy.

3.3 Experimental procedure

3.3.1   Experiment on Explosive Welding

Two sets of EXW experiments were performed on Al-Fe and Cu-Al respectively. For each set, the experiments were repeated four times and all of the four samples were studied. The explosion welded materials evaluated in this study were a standard explosion clad product produced by Dynamic Materials Corporation. The being welded

surfaces were ground to remove the oxides. One of the samples was taken from an aluminum-steel structural transition joint material consisting of 3.175mm thick AA5086, 6.35mm thick AA1100, and 9.525mm thick carbon steel SA516-55. This tri-clad material was produced in a single explosion welding shot. The primary explosive was an ANFO, which was mixture of explosive grade ammonium nitrate (AN) prills with about 6wt% Diesel Fuel Oil. The exact composition is proprietary, but common mixes are discussed in the literature [130]. The flyer plate velocities could be estimated using a modified Gurney equation with the applied explosive load [5]. The flyer plate velocity for aluminum to aluminum welding was estimated to be ~1000m/s, and for the aluminum to steel welding was ~900m/s. The copper-aluminum clad sample was taken from the electrical transition joint. It consisted of the 3.175mm thick Cu102 as the flyer plate and 9.525mm thick AA1100 as the target plate. The copper flyer plate velocity was estimated to be ~450m/s.

3.3.2   Experiment on Magnetic Pulse Welding

The detailed MPW study is discussed in chapter 5-8. In this section, AA6061-T6 plate welded to both Cu110 plate and low carbon steel 1008 plate were taken as examples. For each set, eight samples from the repeated experiments were investigated. A commercial Maxwell Magneform capacitor bank was used, for which the maximum stored energy is 16kJ and maximum working voltage is 8.66kV. There are eight capacitors and each has a capacitance of 53.25 μF. The being welded metal plates were in rectangular shape and the

length was 100mm and width was 75mm. The thickness for the flyer plates varies within the range of 0.3mm to 0.5mm. The welding surfaces were lightly sanded and degreased before impact. The sanding and cleaning process were carried out on a flat steel surface, and thus the plates were flattened at the same time. In order to maintain flatness, a thick steel backing is placed behind the target sheet. The standoff distance was 3.15mm and the overlap width was 12mm. The input energy for successful welding was 4.8kJ for Al-Al, 5.6kJ for Cu-Al and 8.8kJ for Al-Fe. Taking Cu-Al experiments at 5.6kJ as an example, the Cu plate was the flyer plate and placed near to the actuator with an insulator layer in between; and the Al plate was the stationary target plate and placed 3.15mm away from the flyer plate. These two plates had 12.7mm wide overlap, which was the possible welding zone. After the energy discharged from the capacitor bank, the primary current flowed through the actuator and reached the peak value of about 140kA within approximately 12 μs, as shown in Figure 3.1, measured by Rogowski coils. Because of the electromagnetic force, the flyer plate was accelerated until it collided against the target plate. During this process, the flyer velocity was measured. Figure 3.1 also showed the impact velocity was up to 265m/s at 14 μs measured by Photon Doppler Velocimetry (PDV) [131]. After the collision, the sample vibrated and this was shown by the oscillating of the absolute value for the measured velocity.
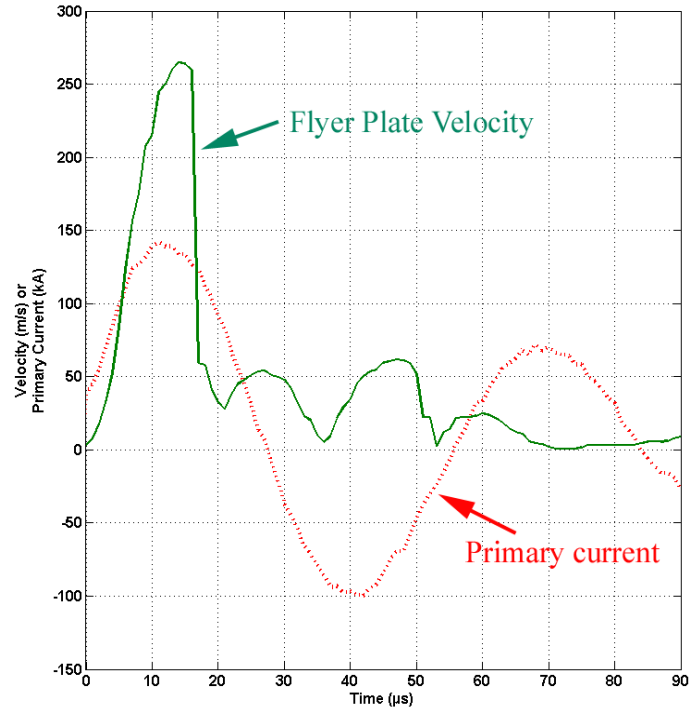
Figure 3.1 Primary current and magnetic pulse induced flyer velocity for MPW process on Cu-Al joint. The flyer plate material for this specific velocity measurement is Cu110 and the thickness is 3.175mm.

3.3.3   Experiment on Laser Impact Welding

In the present study AA1100 plates and low carbon steel 1010 plates were welded by LIW. The laser beam source was a Continuum Powerlite II YAG laser, which could output a 3 Joule pulse in the infrared spectrum at 1064 nm wave length. The pulse width was about

8ns and the beam was focused to a spot size of a 3mm diameter circle. For similar materials welding, the material was a low strength aluminum alloy 1100. The flyer sheet was 3mm wide and 20mm long, with a thickness of 0.175mm. The target plate was large in all dimensions relative to the flyer plate and had a 15°taper as shown in Figure 2.5. For dissimilar materials welding, the flyer plate was AA1100 which was 0.05mm thick, 3mm wide, and 20mm long. The target plate was low carbon steel 1010, which was again a large block with a 15°tapered flat surface. The real impact region on the flyer plate was an approximately 3mm diameter circle. The metal surfaces were lightly ground with sand paper and flattened by steel die prior to welding. For both similar and dissimilar welding, the experiments were repeated and four samples for each set were investigated.

3.3.4   Experiment on Microhardness and Microstructure Characterizaiton

For each welding method, a series of samples were prepared and the cross sections were taken through the middle part of the welded flyer target interface, because the joint in the vicinity of the edge was usually weak. The samples were sectioned and polished through standard metallurgical procedures. The final polish was conducted on a polish cloth with 1μm diamond paste. These cross sections were then examined by an optical microscope (OM), SEM and energy dispersive X-ray spectroscopy (EDS). The microhardness was measured on the exposed surfaces with 10g, 50g and 200g load at 20s dwell time. The wave feature and the microhardness data were the average results collected from all of

the samples for each method.

3.4 Results and discussion

3.4.1 Wave Interface Characterization

The welded interfaces from these three welding processes indicate wave morphology as shown in Figure 3.1(a-b), 3.2(a-b), and 3.3(a-b). For EXW and MPW, the wave structures show both non-symmetric and symmetric waves and it is similar for all of the repeated samples; for LIW, the interface is nearly flat and the waves are more symmetric. The wave lengths and amplitudes increase with both increasing input energy and sample thicknesses. In EXW, the wave loses symmetry and forms crests shape interface. LIW surface demonstrates periodic sine waves with quite small wave lengths and amplitudes. In all cases, the two materials do genuinely adhere to one another except the edge, and detailed mechanical testing is in progress.
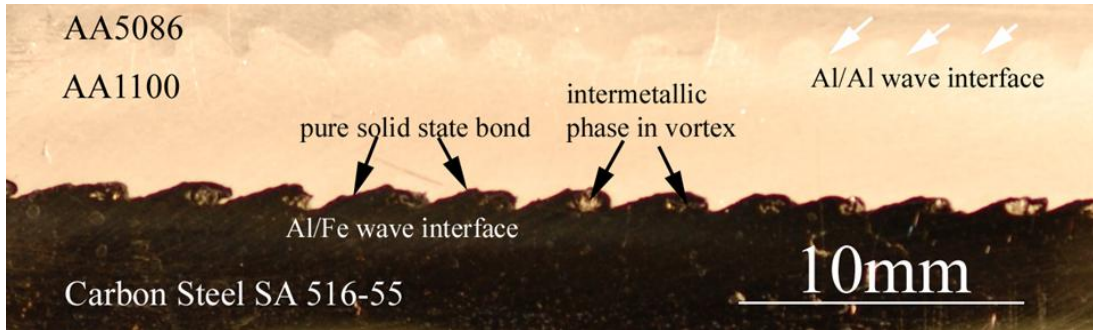
(a) Three metal layers were welded together. From top to bottom, the materials are AA5086, AA1100 and Carbon Steel SA 516-55. There were two wave interfaces and they are Al/Al and Al/Fe interfaces.
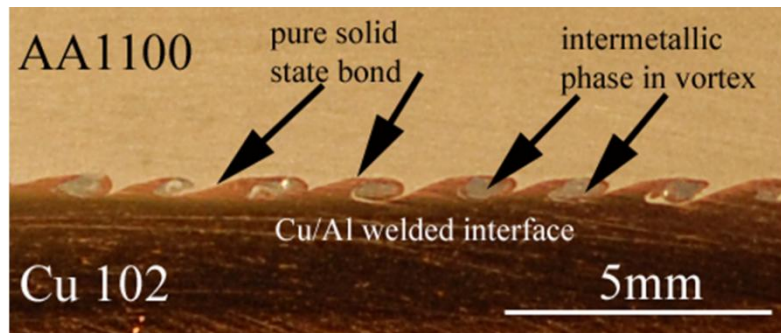
(b) Welded interface between AA 1100 and Cu 102.

Figure 3.2 Wave interface morphology from EXW.
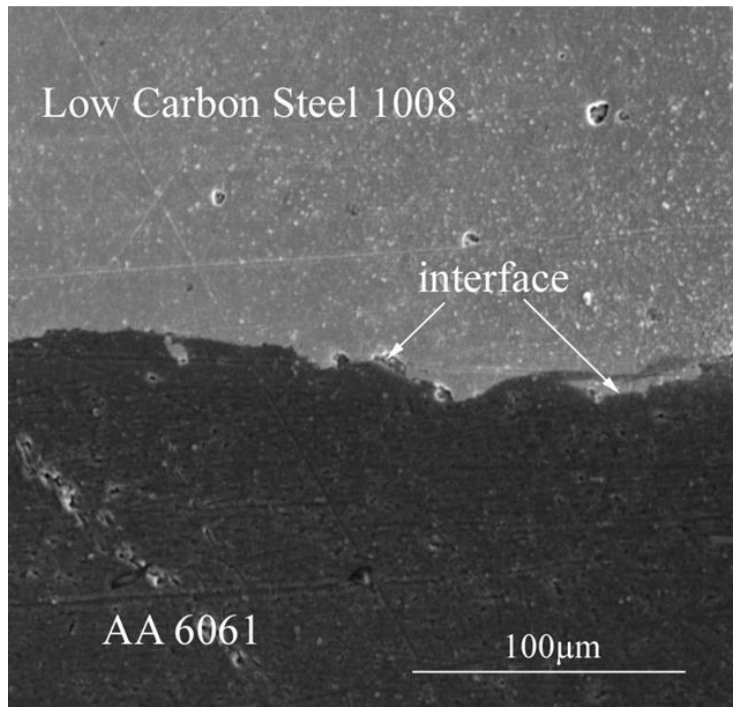
(a) Interface between low carbon steel 1008 and AA 6061.
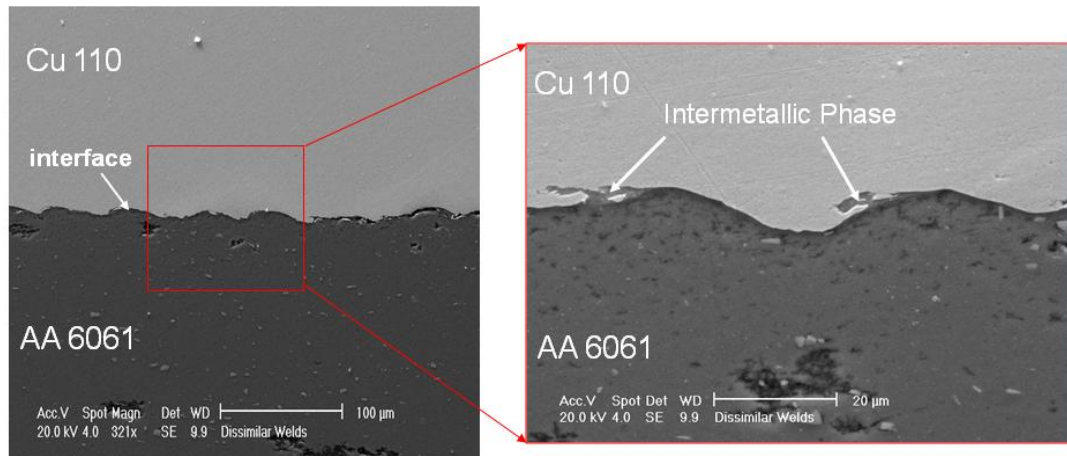
(b) Interface between Cu 110 and AA 6061.

Figure 3.3 Wave interface morphology from MPW.
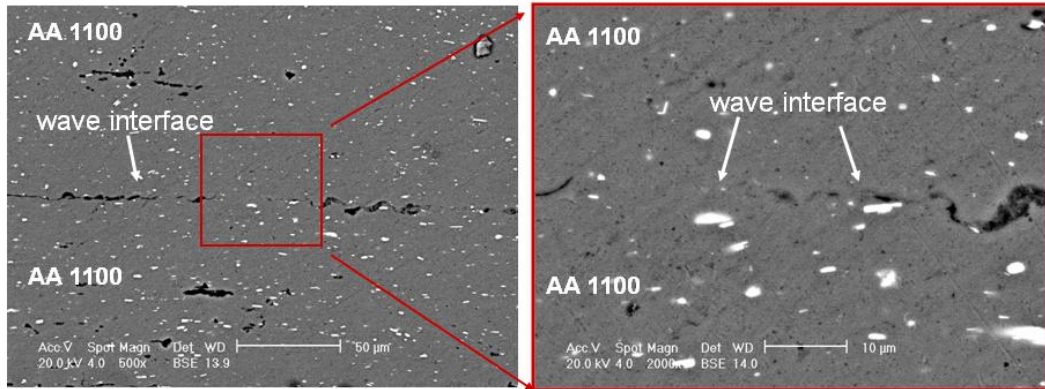
(a) Interface morphology made by LIW on AA 1100 welds.
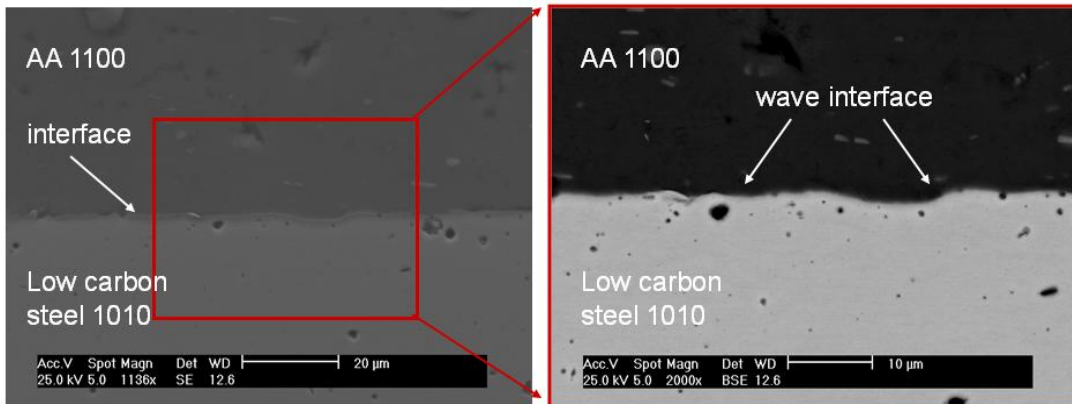
(b) Interface between low carbon steel 1010 and AA 1100.

Figure 3.4 Wave interface morphology from LIW.

For each cross section sample, the wave length and wave amplitude were measured. All of the samples in every welding method showed the similar wave features, but at widely different amplitudes. The average results from all of the examined samples are

58

summarized in Table 3.1. The wave length generally correlates with impact velocity. Since it has been suggested that the flyer plate thickness (t) will influence the wave shape, wave length (λ) and the amplitude (A) [132], in this study, the wave length and amplitude were normalized as λ/t and A/t.

Table 3.1 Summary of wave length and amplitude from EXW, MPW, and LIW

Welding Method	Materials (Flyer/Target)	Flyer Plate Thickness (t) (mm)	Energy Density (kJ/m^2)	Impact Velocity (m/s)	Wave Length (λ) (mm)	Wave Amplitude (A) (mm)	λ/t	A/t	λ/A
EXW	Al/Al	3.175	4286	~1000	3.60	0.83	1.134	0.261	4.34
	Al/Fe	6.35	6944	~900	4.00	0.65	0.630	0.102	6.15
	Cu/Al	3.175	2861	~450	1.26	0.21	0.397	0.066	6.00
MPW	Al/Al	0.50	640	~300	0.100	0.010	0.200	0.020	10.00
	Al/Fe	0.406	1173	~250	0.064	0.009	0.158	0.022	7.11
	Cu/Al	0.31	747	~265	0.045	0.004	0.145	0.013	11.25
LIW	Al/Al	0.175	53	~475	0.034	0.0020	0.194	0.011	17.00
	Al/Fe	0.050	53	~475	0.017	0.0008	0.340	0.016	21.25

Figure 3.4 is the map of the normalized wave length (λ/t) and wave amplitude (A/t) for the three different welding methods. It indicates that, high impact energies result in long wave length and increased amplitude, and amplitude and wave length tend to scale with each other. The lower energy intensities for MPW and LIW result in smaller waves. With the large excess energy of EXW, the interface still has periodic wave fashion, but the wave shape loses the symmetry and has strong vortices. With lower impact velocity in LIW, the interface has smoother wave with reduced amplitude.
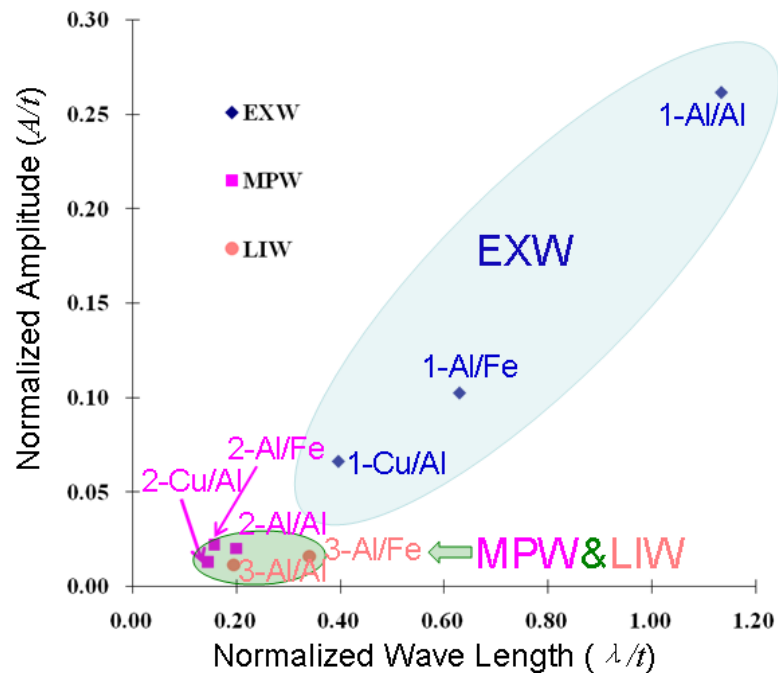
Figure 3.5 Wave length and wave amplitude map for three different impact welding processes. The map could be divided into two domains, and they are EXW domain and

MPW&LIW domain. In each domain, there are different welded metal pairs. 1-Al/Al is EXW for AA5086/AA1100; 1-Al/Fe is EXW on AA1100/Carbon Steel SA 516-55; 1-Cu/Al is EXW on Cu102/AA1100. 2-Al/Al is MPW on AA6061/AA6061; 2-Al/Fe is MPW on AA6061/Low carbon steel 1008; 2-Cu/Al is MPW on Cu110/AA6061. 3-Al/Al is LIW on AA1100/AA1100, 3-Al/Fe is LIW on AA1100/Low carbon steel 1010.

The wave morphology increases the intimate contact area, and can aid interlocking between two metal surfaces for strong bond. Most researchers think of the waviness as being caused by a Kelvin-Helmholtz instability [132]. The oblique impact process generates intense shear stress and the shear stress is spread out from the collision point. When the shear stress exceeds the welding plate yield stress, the plates can be regarded as an inviscid fluids [24] and the high values of plastic strain occur near the impact. From the collision point to the entire mating interface, the velocity distribution, the strain and strain rate distribution have large variations. Interacting with the disturbances from the fluid-like welding plates, the variation is believed to result in the periodic wave interface. Despite sample to sample differences, it appears that the same basic mechanism works over a range of length and energy scales. Varied impact velocities and angles, which were not studied presently, are also expected to cause variations.

3.4.2 Interfacial Intermetallic Phase Formation

It is also interesting to point out that there is extensive mixture, which was possible intermetallic phase, formation in the corner of wave vortex for EXW and MPW as shown in Figure 3.1(a-b) and 3.2(b), while the interface for LIW is relatively flat and the intermetallic phases are largely absent. The pockets of intermetallics are likely formed by intense local heating, melting, mixing and rapid solidification in wave vortices. The interface forms discontinuous pockets, but the most welded region is free from intermetallic phases in all cases. The intermetallic phase along the EXW welded interface was taken as an example here because it was more obvious by larger length scale. The chemical composition changes cross the interface were studied by EDS from different locations as shown in Figure 3.5 (a) and 3.6 (a). And the EDS results are shown in Figure 3.5 (b-c) and 3.6 (b-c). In the region of an apparent pure solid state bond, the chemical composition profile has sharp interface composition change, as shown in Figure 3.5 (b) and 3.6 (b), whereas for the interface with intermetallics, the composition gradually changes from one phase to other phase with several steps. And these steps in Figure 3.5 (c) and 3.6 (c) indicate varied Al-Fe and Al-Cu compounds respectively.
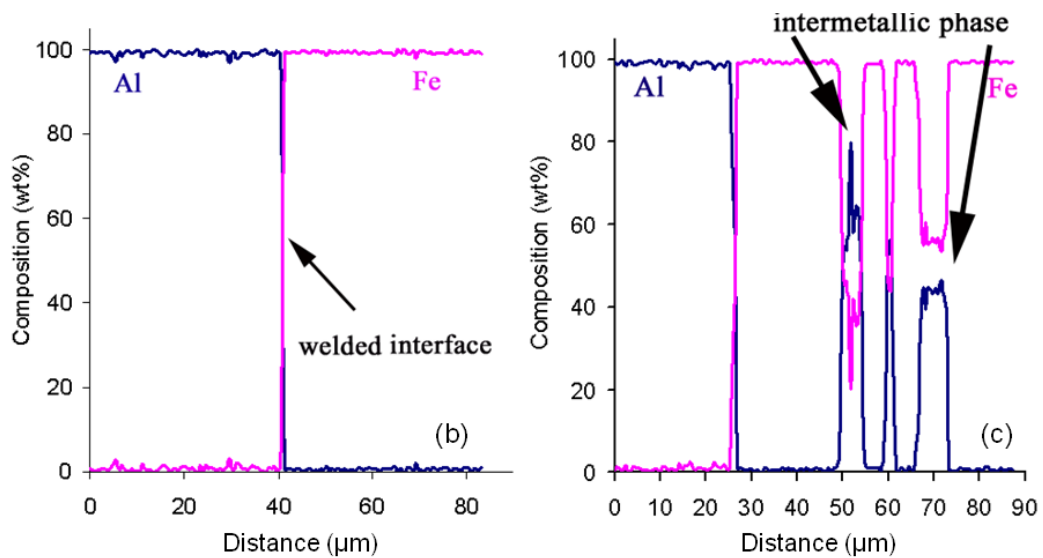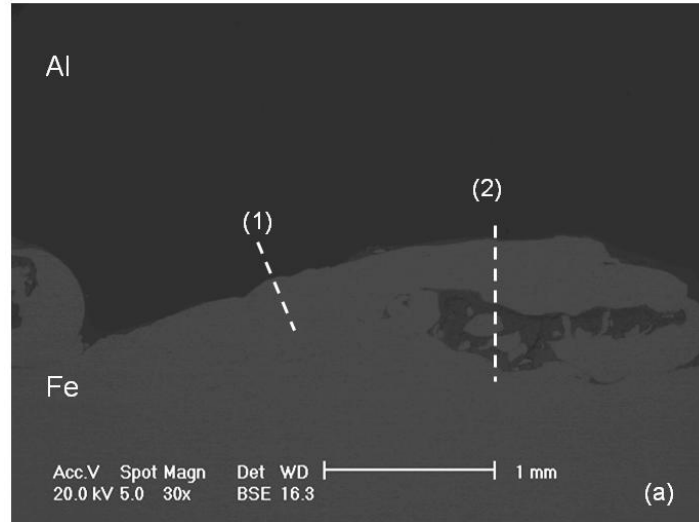
Figure 3.6 EDS study on EXW welded Al-Fe interface. (a) SEM image, the two white lines indicate the linear EDS scan locations. Both of them were across the interface. One was in the pure solid state bond region, position (1); and the other crossed the intermetallic phases, position (2). (b) Chemical composition distribution for linear scan from the pure solid state bond region at position (1). (c) Chemical composition distribution for linear scan from the Al-Fe intermetallics region at position (2).
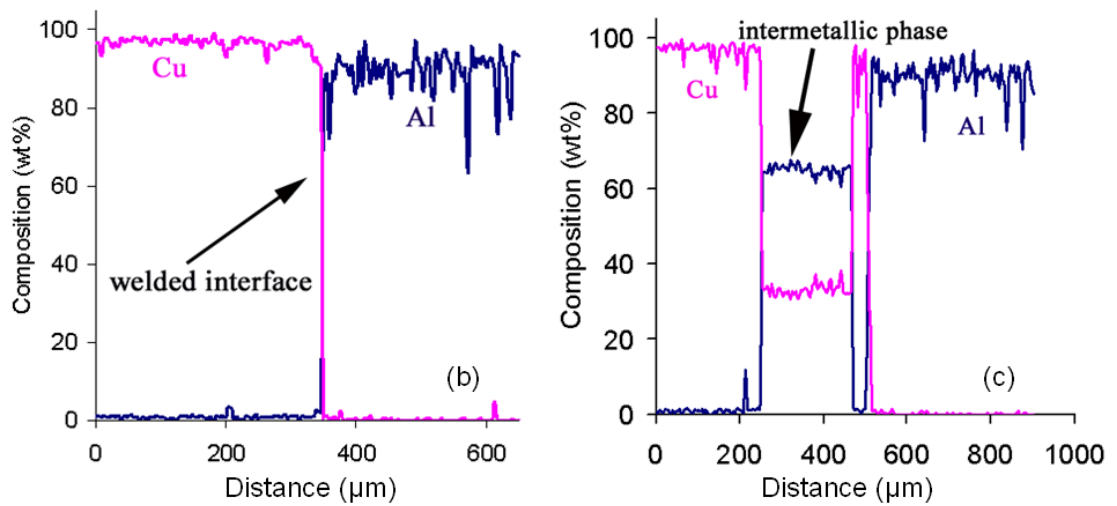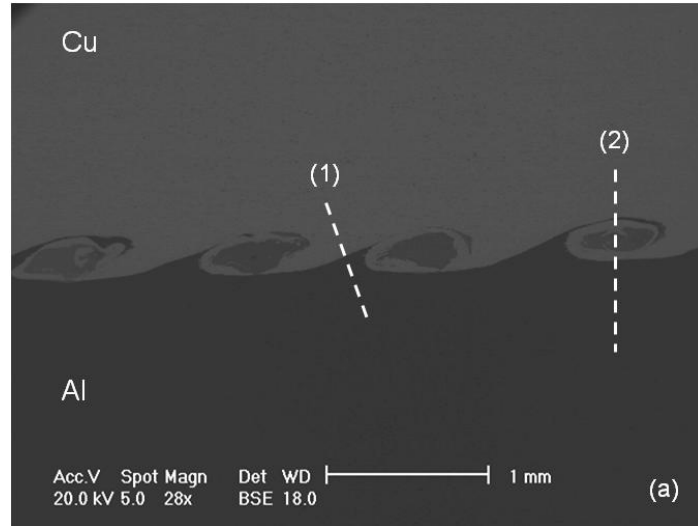
Figure 3.7 EDS study on EXW welded Cu-Al interface. (a) SEM image, the two white lines indicate the linear EDS scan locations. Both of them were across the interface. One was in the pure solid state bond region, position (1); and the other crossed the intermetallic phases, position (2). (b) Chemical composition distribution for linear scan from the pure solid state bond region at position (1). (c) Chemical composition distribution for linear scan from the Cu-Al intermetallics region at position (2).

The structure and distribution of the intermetallic regions that form in impact welding are quite important. Fusion welding of dissimilar metals is essentially impossible, because wide regions of intermetallic form and these are almost universally very brittle. Thus, fusion welded interfaces will have very poor reliability and poor mechanical strength. While intermetallics can form on impact welding, these regions are discontinuous and the resulting overall structure is expected to have excellent toughness in all cases, because none of these collision-welding processes lead to the formation of continuous intermetallic phases.

3.4.3 Interfacial Microhardness

The average Vickers microhardness (HV) values taken from the interface region are shown in Figure 3.7 (a-b). For each of the three impact welding processes, the interfacial hardness is higher than that in the base metals. Local plastic deformation and impact shock harden the local regions. For EXW interface, within 250 μm wide range on either side, the hardness increases obviously, as show in Figure 3.7 (a). Beyond the strengthened region, the hardness is same as the base metals. For MPW and LIW, the hardened interface region on either side is smaller and the width is about 50μm and 20μm respectively, as shown in Figure 3.7 (b). The size of these hardened zones largely scales with the energy input and wave lengths seen in each case. This is significant because in fusion welding, in most cases, local heating generates HAZ that are softer than the base

metals, which reduces joint efficiency. Thus, impact welding holds the opportunity to produce welds with much greater joint efficiencies.

(a)   (b)
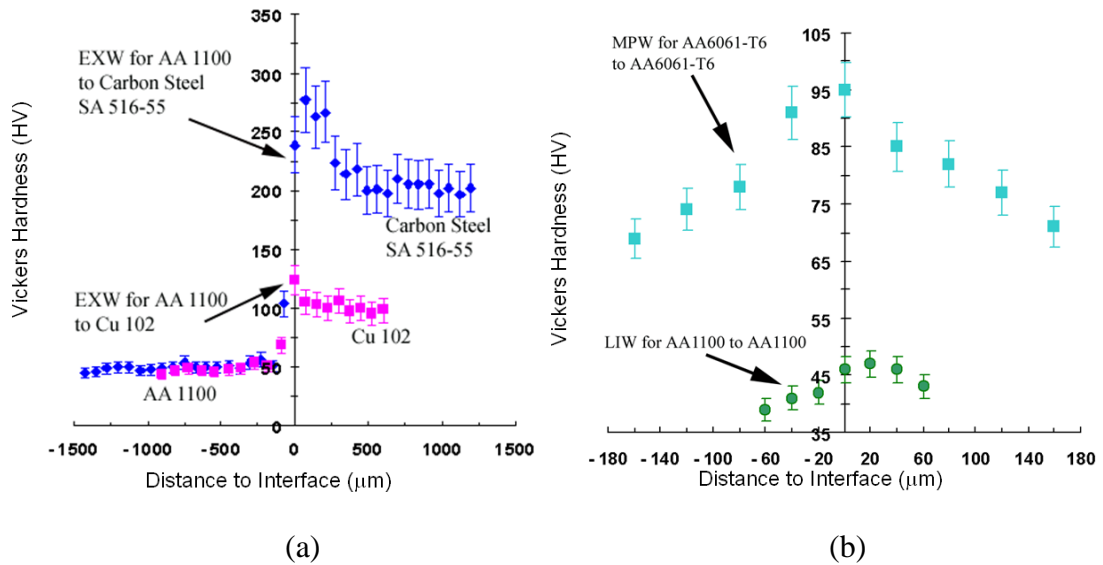
Figure 3.8 Summary of microhardness testing results for three welding methods. (a) Microhardness changes across EXW welded Al-Fe and Cu-Al interface. The testing load is 200g and the dwell time is 20s. (b) Microhardness changes across the interfaces from MPW welded AA6061-T6 pairs and LIW welded AA1100 pairs. The testing load for MPW interface is 50g and for LIW interface is 10g, the dwell time is 20s.

3.5 Conclusion

The structures that result from three types of solid state impact welding processes are

studied and compared, and the three welding processes are EXW, MPW and LIW. The study shows that high velocity oblique impact welding is feasible for all length scales with proper impact angle and velocity. And all of them can be applied to join similar and dissimilar materials. The wave interface is observed at all length scales, and it is presumed that cleaning of the interface by jetting is also important in all cases. The jetting removes surface oxide layer and the oblique impact brings the two clean surfaces joint together. In each case, a wave interface was generated and the wave length and amplitude are related to both flyer plate thickness and flyer impact velocity. High energy density results in long wavelength and great wave amplitude. EXW has wave interface with vortex; MPW has wave interface near sinusoidal profile; LIW has a relatively gently curved surface. Interfacial intermetallic phase was often found to exist in the wave vortex of explosively welded samples, but there was no continuous intermetallic layer along the welded interface. Intermetallics were possible but isolated in MPW, and were not observed in LIW. It was also found that all of the three welding processes result in the improved microhardness along the interface after high velocity impact welding. While EXW has earned a reputation for excellent weld quality between widely dissimilar metals, MPW and LIW produce similar structures. These techniques are significant because they can be easily applied in typical manufacturing environments, and therefore offer new opportunities for dissimilar metals welding.

Chapter 4 Magnetic pulse welding process study

4.1 Introduction

As discussed in chapter 3 that impact welding can be applied for different length scales to obtain high strength joint, the detailed welding process, joint strength and joint interface metallurgy of MPW are discussed from this chapter to chapter 9. For MPW, the weldability and joint strength are strongly dependent on the impact welding process. There are various process parameters for MPW. Some of them are adjustable during every single welding, for example, the impact energy level, the standoff distance, and the overlap width. Others are constant and determined mainly by the welding system, for example, the actuator inductance and the secondary current density. In order to investigate the condition for successful welding and also to improve the energy efficiency, it is necessary to monitor the process parameters and obtain the optimal condition of the process parameters. However, capturing the parameters for MPW is quite difficult, because it is an extreme short process; the welding duration is only about a few microseconds. Therefore, high precision, high resolution and reliable measurements with

particular analysis approaching have been developed to investigate the process parameters. This chapter discussed the actuator design for different workpiece geometry, the process parameter measurement, and the suitable materials properties for MPW.

4.2 Actuator design

For MPW, the actuator is used to transform the stored electrical energy into kinetic energy of the nearby workpiece. The actuator significantly affects the welding system efficiency because the distribution of the generated electromagnetic field is mainly determined by the actuator geometry. With certain amount of the input energy, the efficient design of actuator can offer maximal force to accelerate the flyer plate with much less energy waste in form of heating or expanding the actuator itself. The design of the actuator also depends on the welding workpiece geometry. Circular actuator is used for tubular lap welding and single turn flat actuator can be applied for plate to plate lap welding. Since MPW is compression based lap joining, it is required to condense the primary current and the resulting Lorentz force within the section where the overlap of the being welded workpiece is. Three types of actuators were applied in this research work and they are discussed as below.

4.2.1   Circular Actuator for Axis Symmetrical Welding

Figure 4.1(a) presents the electronic circuit for MPW system, which includes AC power supply, charger, capacitor bank, high current switch and the actuator. A circular actuator with both flyer and target workpieces was shown. The primary current through the circular actuator generates symmetrical electromagnetic field as shown in Figure 4.1(b). As a result, the repelling force on the being welded tubes is symmetrical and thus the welded region on tubes is also symmetrical with regard to the tube axis. Not only for welding, this actuator is also used for localized tube compression or expansion. The circular actuator can be designed as a single turn closed actuator or a connection between two open half-circular actuators. The former one has higher energy efficiency and can result in uniform welding since there is no gap on the actuator or any resulting electromagnetic field leakage, but it is difficult to assemble very long workpiece into the actuator. For large workpiece, the latter one is easy to assemble with, but the energy efficiency will be lower due to the connection between two half circles. It is important to point out that during real impact welding process, the coaxial alignment and overlap alignment between the actuator and the workpieces can affect the joint quality.
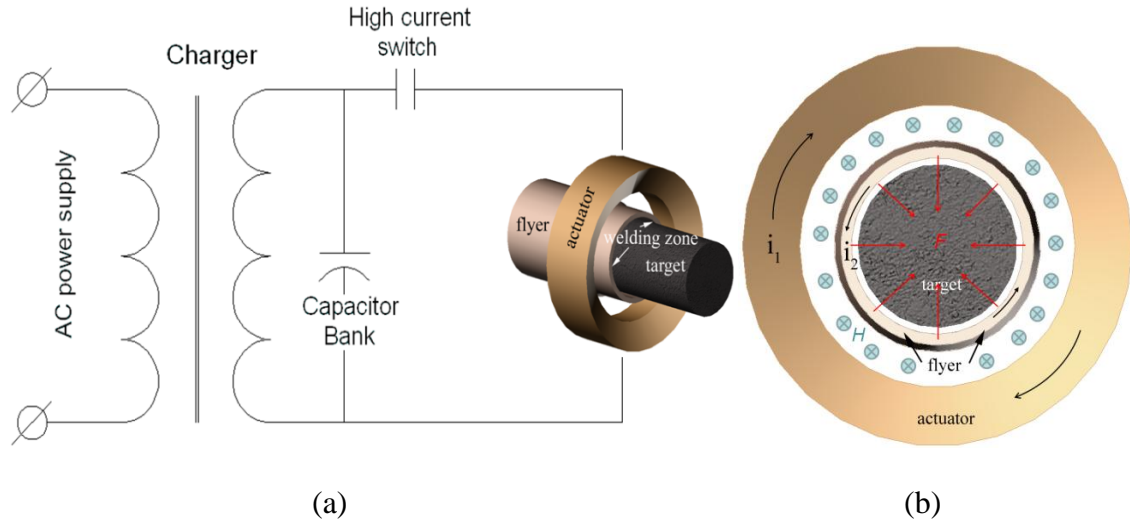
Figure 4.1 Schematic of MPW system for tubular welding. (a) Electric circuit for welding system with circular actuator. (b) Induced electromagnetic field *H (indicated by dots)* and repulsive force *F (indicated by arrows)* acting on the flyer tube. i_1 is primary current in actuator and i_2 is induced current in flyer.

4.2.2 Bar Actuators for Axis Asymmetrical Welding

One variation of flat bar actuator with different cross section areas of the inbound and outbound legs is designed for plate to plate welding. The asymmetrical design helps to increase the primary current density and concentrates the Lorentz force narrowly in the leg with small cross section area. Two generations of the flat bar actuators were developed for linear seam welding. A particular bar actuator was developed for coupled flanging and welding process. In the following section, these three types of actuators

were discussed.

4.2.2.1 Flat Bar Actuator

The first generation of the flat actuator is shown in Figure 4.2(a) made by copper alloy, C2 C18150 Plate. Once the primary current flows through, the current density inside of the narrow leg is greater than that of the wide leg because of smaller cross section area. The being welded region is set right above this narrow leg. The finite element based software *Magnet*® was used to assist the actuator design. Figure 4.2(b) is the simulated current density contour for the bar actuator. Once the current density in the narrow leg surface is about 70% of the total current density, the design can be used for real impact welding. Otherwise, the modification of the actuator dimension is necessary. The other critical factor for the flat bar actuator design is the actuator inductance, which is proportional to the spacing between the inbound and outbound of the current through the actuator. High inductance is preferred for impact welding because it reduces the rise time. Figure 4.2(c) is the real actuator followed by the design and simulation results which was used for welding experiments.
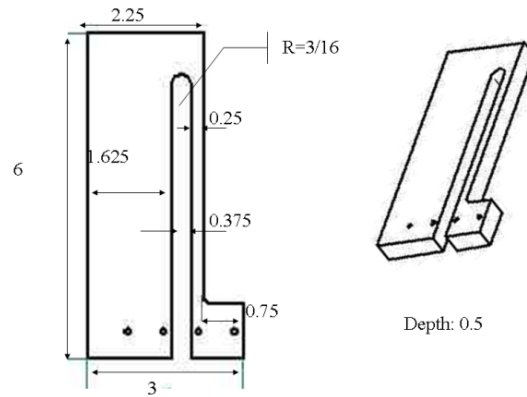
(a)
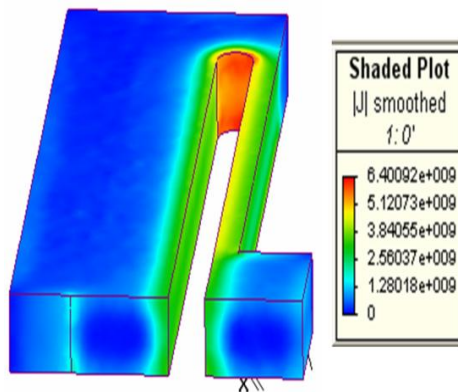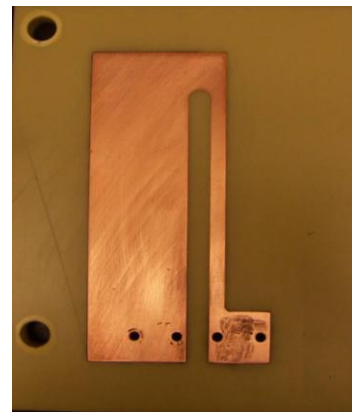
(b)   (c)

Figure 4.2 (a) Schematic of the first generation flat bar actuator. The unit is in inch. (b) *Magnet*® simulated current density within the actuator. (c) The real actuator for welding.

4.2.2.2 Chamfered Actuator

It is known that the combination of impact angle and impact velocity determines the welding succeeds or not. In order to study the impact angle and impact velocity effects for the seam linear welding, the second generation flat bar actuator was designed, which

is able to assemble the testing probes and also to offer different initial launch angles. Figure 4.3(a) presents the actuator which is assembled into the die. The narrow leg has a chamfered angle and four through holes with 2.54mm diameter. The holes are used to assemble the laser beam probes for impact velocity measurement at different locations. And the chamfered angle determines the initial launch angle as shown in Figure 4.3(b). The narrow leg has been chamfered into 5 °, 10 °, 15 °, 20 °and 30 °angles. Accordingly, the being welded flyer plates were bent to such angles which are regarded as the initial launch angles. Therefore, the impact angles should be no larger than the initial launch angles.
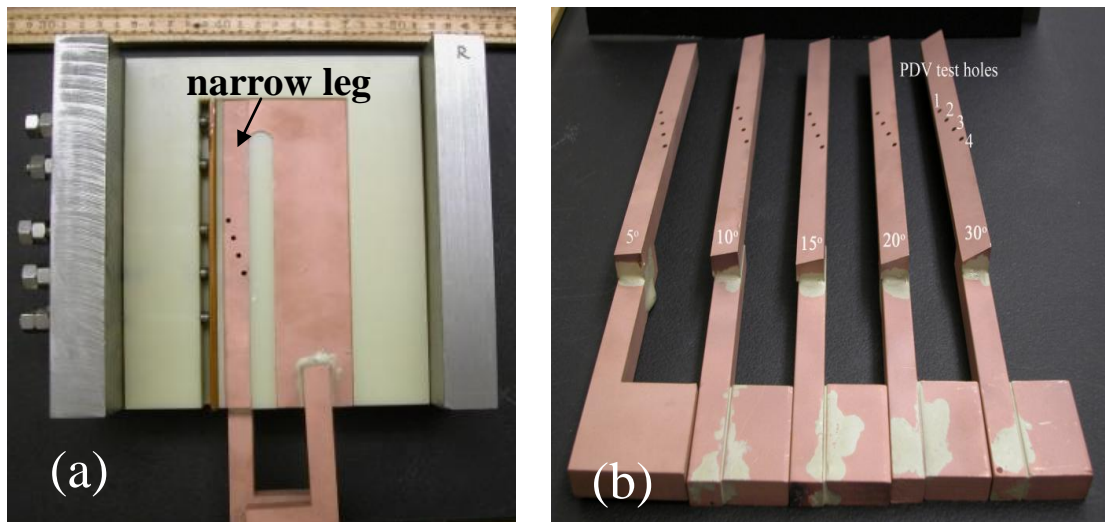
Figure 4.3 (a) Second generation of the flat bar actuator with chamfered legs. (b) narrow legs with different chamfered angles.

4.2.2.3 Pre-flange Actuator

The pre-flange actuator can be regarded as a bar actuator, however the inbound leg and outbound leg are not in the same plane as shown in Figure 4.4. The being welded plate was bent and inserted beneath one of the actuator legs with certain pre-flanged angle. Once the primary current goes through the actuator, the Lorentz force from the outbound leg will push the flyer down against the target and weld them together with high impact velocity. Therefore, with such built in impact angle, the flyer plate undergoes flanging and welding at the same time.

Figure 4.4 Pre-flange actuator with workpieces. The inbound and outbound currents were labeled onto the actuator.

4.2.3 Uniform Pressure Actuator for Embedded Wire Welding

The uniform pressure (UP) actuator developed by Daehn, Kamal and Banik [133, 134] has been used for electromagnetic assistant forming process. In this research, UP actuator was used for impact welding. The preliminary attempts for impact welding were conducted with embedded wires between the flyer and the target plates. The embedded wires are attached to the target plate by tape prior to welding. These wires were used to make the flyer contact onto the target with certain impact angle. If there is no wire between them, the UP actuator accelerates the flyer plate to against the target plate parallel but no joint can be formed after such parallel impact. As shown in Figure 4.5, UP actuator is a solenoid actuator with several turns. The detailed geometry information of the actuator will not be discussed here and it can be find in Manish Kamal's thesis [134]. The flyer plate is loaded onto the outer channel. And it undergoes approximately uniform pressure from the inner actuator during the impact process. In order to fix the target plate during impact process, a top die is put onto the target plate and the welding system is then clamed down with press at 5000psi pressure to avoid any energy waste in form of the target plate or the top die moment.
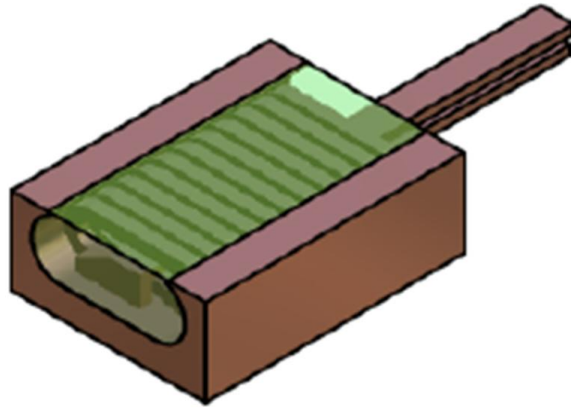
(a) Illustration of uniform pressure actuator[133]
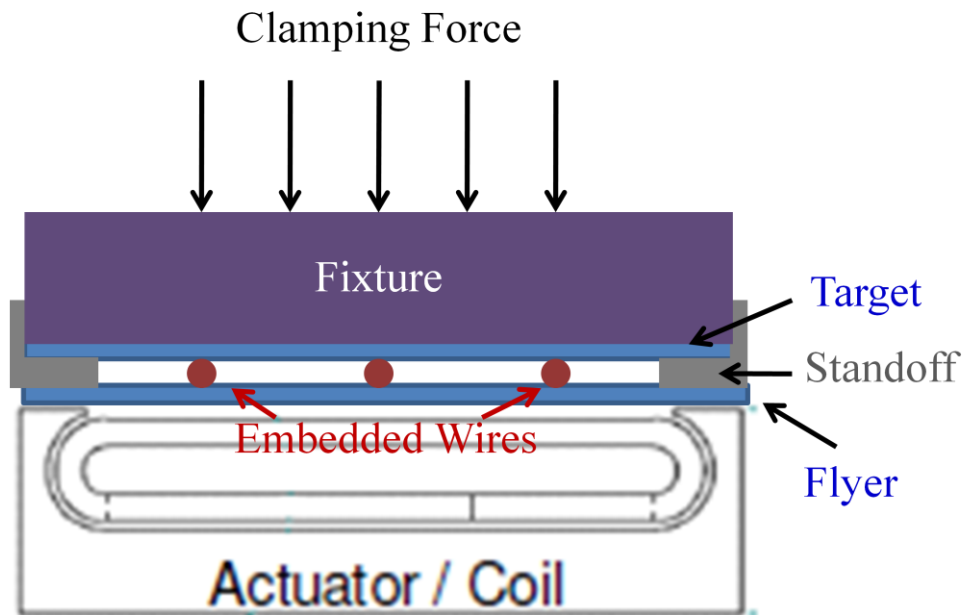
(b) Welding system with uniform pressure actuator

(c) Welded sample for aluminum plate with steel wire embedded

Figure 4.5 Uniform pressure actuator applied for plate to plate welding with embedded wires.

4.3 Process parameter measurement

The process parameters for MPW are various, including the impact energy level, the primary current density, the impact velocity and impact angle, the impact duration, the standoff distance, the overlap width between the flyer and the target plates, and the workpiece thickness. In order to investigate the successful welding conditions for different materials, some adjustable process parameters are investigated instrumentally as discussed below.

4.3.1   Impact Energy Level

One of the basic factors for the impact welding process is the impact energy level which is easily controlled by adjusting the capacitance of the capacitor bank, because the energy from capacitor is proportional to the charging voltage and the square of the bank capacitance. It was reported that the efficiency for transforming the stored energy into the kinetic energy of the workpiece is in range of 10 to 20 percentage [135]. The energy level mentioned in this study is the nominal energy discharged from the capacitor bank and only portion of it transferred into the flyer plate kinetic energy.

A commercial Maxwell Magneform capacitor bank was used for all of the asymmetric welding. There are six capacitors with 53.25 μF capacitance. The maximum output energy value is 16kJ and the working voltage is up to 8.66kV. The tested energy level for MPW

varied from 3kJ to 12kJ. Generally speaking, high impact energy leads to high impact velocity and high strain rate deformation on the welded workpieces. Insufficient energy level is not able to generate jet for atomic bonding, whereas extreme impact energy results in overheating or arcing. Therefore the suitable impact energy levels for different materials welding were studied separately in the following chapters.

4.3.2   Primary and Induced Current Measurement

As shown in Figure 4.1, the actuator is connected to the inductance-capacitance-resistance (LCR) circuit. During energy discharging process, there is an alternating current (AC) through the actuator, which is called primary current. It induced a parallel current circuit in the nearby metal plate with opposite direction, which is the eddy current. Such eddy current in the nearby workpiece was also named as the secondary current. Rogowski coil is used to measure both primary and secondary current by monitoring the mutual inductance interference of the magnetic fields. The peak value of the current changes with the impact energy level, but the time for the current to reach peak value (rise time) does not affect by the impact energy level. It mainly depends on the capacitance and inductance of the capacitor bank and the applied actuator.

4.3.3   Impact Velocity and Impact Angle Measurement

4.3.3.1 Photon Doppler Velocimetry Working Principle

PDV has been developed [131] and packaged into the welding system to monitor the impact velocity. It is different with the traditional high velocity measuring instrument Velocity Interferometer System for Any Reflector (VISAR) which was developed by Barker and Hollenbach at Lawrence Livermore National Lab (LLNL) in 1972 [136]. VISAR requires careful optical alignment and light collection. And it is expensive because it requires large laser light sources. However, PDV system is inexpensive, because the main components for PDV are fiber optic lasers and high speed oscilloscope. PDV can measure the moving surface velocity with exceptional resolution and accuracy. The measured results provide submicron displacement resolution and nanosecond range temporal resolution. The maximum measurable velocity depends solely on the bandwidth and acquisition rate of the photodetector and oscilloscope. By multiple fiber optic lasers in several channels, it is straightforward to collect the data at multiple locations. PDV is compact and can be easily packaged into the electromagnetic forming facilities in geometrically tight situation. Taking MPW as an example, the thin fiber optic laser line, covered by an inexpensive probe, is directly inserted into the bottom die and aligned concentrically with the through holes on the actuator narrow leg. Therefore, the laser beam can aim at the flyer plate surface and captures its movement. There are two advantages to use PDV for electromagnetic forming process. First, the fiber optic lasers do not cause any electrical isolation for the welding system. Second, the magnetic pulse generated noise does not interfere with the velocity signal. The working principle of PDV is schematically shown in Figure 4.6.
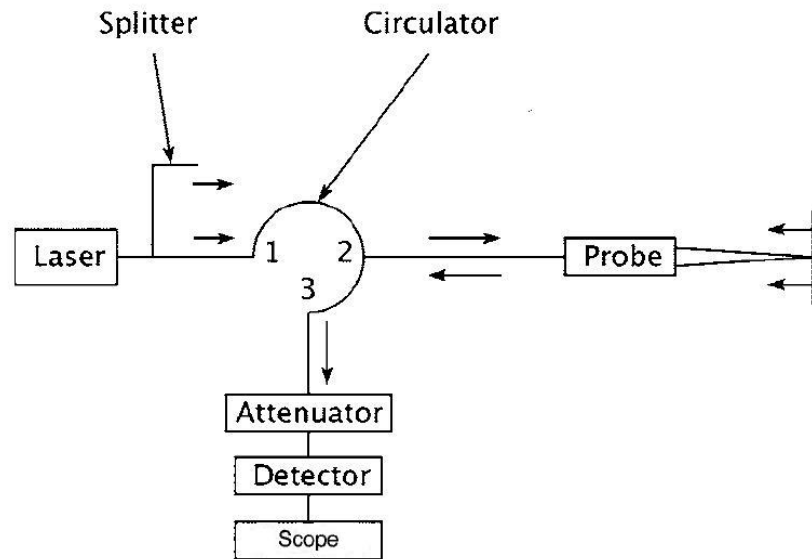
Figure 4.6 Schematic diagram of a Photon Doppler Velocimeter (PDV) system [131].

The PDV system has been adopted and specially developed in electromagnetic forming group at The Ohio State University [131]. The high power erbium fiber laser is used and it has about 1550nm narrow spectral linewidth, and 1000mW output power with the frequency less than 3kHz. As shown in Figure 4.6, once laser passes through the splitters, it is divided into multi channel and transported in several independent fiber optic ports, which are good for multiple location measurement. The separate laser beam transported into the probe and then aims at the moving surface. Both the incident laser beam and the reflected laser beam are guided into the detector by a one watt uniphase device. The detector is a short rise time battery biased photon detector with frequency 1.5GHz, which

is comparable to oscilloscope. The applied LeCroy Wavesurface 104MXs oscilloscope has 1GHz frequency, 5GS/s sampling rate and four channels. This oscilloscope has large data storage and the storage period is up to 2ms at full speed on all of the four channels. The attenuator shown in Figure 4.6 is used to adjust the signal level to avoid the damage of excessive optical flux. More details about the PDV system is described in reference [131].

4.3.3.2 Impact Velocity Measurement

PDV collected both the incident beam and the reflected beam from the moving surface. These two beams generate beat frequency and such beam frequency is proportional to the moving surface velocity. Therefore, by analyzing the beat frequency, the yield velocity and time profile is known. The full beat cycle is observed for every half of the incident wavelength, 1550nm/2=775nm, and the simple way to calculate the velocity is distance dividing by time, so the moving surface velocity can be calculated by 775nm dividing the period of one beat cycle. The PDV raw data is in frequency domain, and a Fourier Transform is performed to change the raw data into time domain and obtain the period of the one beat cycle. The four PDV channels correspond to four independent measurements and the calculation of the velocities are same. The related displacement can be integrated and it is in the order of millimetres to centimetres.

During impact welding process, the fiber optic laser beams aim at the flyer surface and capture its entire movement. A subroutine for Matlab program has been developed which is capable to analyses the raw PDV data into the impact velocity versus time profile directly.

4.3.3.3 Impact Angle Calculation
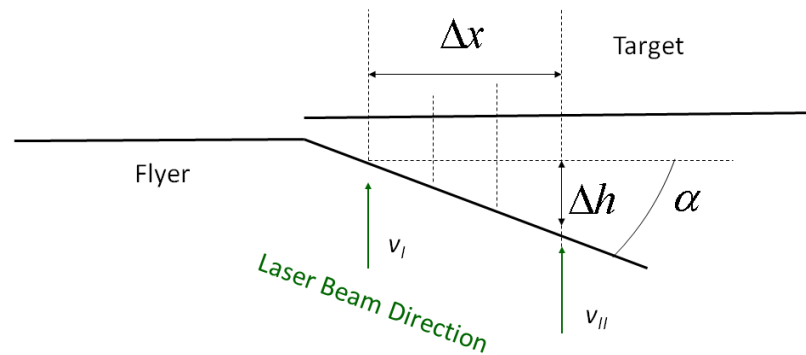
Figure 4.7 Schematic of impact angle calculation.

PDV probes can be used to measure multiple velocities at different specific locations as shown in Figure 4.7. During impact welding, the flyer plate collides onto the target plate forming an initial welding line and this welding line moves along the being welded interface. Due to the oblique impact, the flyer plate travels in shorter distance to contact the target plate at the position of the initial welding line than at the position of the final

welding line. Assuming the flyer plate is rigid before collision and deformable after collision, the impact angle can be calculated as Equation (4.1)~(4.2).

$$\alpha = tg^{-1}\frac{\Delta h}{\Delta x}$$ Equation (4.1)

in which, Δh is the travelling distance difference and Δx is the distance between the two measured position. The traveling distance difference can be calculated as:

$$\Delta h = \int v_2 dt_2 - \int v_1 dt_1$$ Equation (4.2)

v_1 and v_2 are the velocity at position 1 and 2, t_1 and t_2 are the total travelling time for the impact process at position 1 and position 2.

4.4 Materials selection

4.4.1   Electrical Property

MPW involves electromagnetic interference and thus metals with high electric conductivities are preferred. For low conductivity materials, MPW can be applied but a metal driver layer is required to pick up the electromagnetic force. Usually, high electrical conductivity results in large repelling force on the flyer plate. For this research work, the copper alloy, aluminum alloy, and low carbon steel were investigated.

4.4.2 Mechanical Property

High velocity impact process leads to high strain and high strain rate deformation on the being welded materials. At the collision point, the electromagnetic pressure can reach beyond the materials yield strength and undergo plastic deformation. Therefore, the yield strength of the being welded materials influence the welding condition. Additionally, the hardness and the strength differences between the flyer plate and the target plate also determine the weldability. Ben-Artz etc. [132] reported that soft materials are easily to be welded onto hard materials. In other words, large hardness difference benefits the weldability for MPW.

4.4.3 Thickness

The thickness of the being welded workpiece influences the induced current distribution, the adiabatic heating distribution, the joint interface morphology and the joint strength. The flyer plate thickness should be larger than its skin depth to confine the magnetic field within the flyer plate. And the skin depth is calculated as Equation (4.3):

$$\delta = \frac{1}{\sqrt{\pi \sigma \mu f}} \quad \text{Equation (4.3)}$$

in which δ is skin depth, σ is conductivity of work piece, μ is permeability, f is frequency of the field variation.

Previous research work also indicated that the interface wave morphology is affected by the workpiece thickness [137]. Large thickness results in large wave length and wave amplitude. Thickness variation may also cause high velocity impact induced defect in certain aluminum tubes, such as spalling, because of the alternatively penetrated tension and compression plastic strain, which is studied in Chapter 5.

In a summary, several different types of actuators were designed for different welding geometry. And the mentioned process parameters were investigated for every welding experiment to find out the successful welding situation. In this research work, design of experiment approach was used to systematically study the effect of the energy level, standoff distance, and sample thicknesses. By changing the parameters and monitoring the impact velocity and impact angle, the successfully welding conditions for different material pairs were obtained. And the weldability map with regard to the impact parameters for copper alloy 110 was developed. The detailed information is discussed in the following chapters.

Chapter 5 Magnetic pulse welding on aluminum alloy 6061

5.1 Abstract

MPW is applied for aluminum alloy (AA) 6061. This is similar material welding and both the flyer and the target plates are AA6061. The metallurgical bond by oblique impact was realized on both linear and tubular configurations. With high impact velocity up to about 250m/s and the resulting jet, the metal surface oxide layers were removed and the two atomic level clean metal surfaces were welded together. During the welding process, the joined interface underwent high strain rate deformation. Therefore, their mechanical properties and microstructure were affected. This chapter examined the joint by lap shearing test, peeling test and nanoindentation test. The results indicated that the joint interface mechanical properties were improved comparing to the base metal. The interface microstructure was studied by OM, electron backscatter diffraction (EBSD) and TEM. It exhibited extremely refined grains with higher grain boundary angles. It was also noticed that the dislocation density in the grain interior increased after impact welding. The joint strength improvement was attributed to all of these microstructure changes. Significant spalling was observed away from the welded region, in the interior of tubular

welds. The results show the complex interaction of shock waves with the materials during this impact welding process.

5.2 Introduction

AA6061-T6 aluminum alloy was chosen because it has good weldability and suitable conductivity for MPW, and it is also widely used for lightweight components. MPW is a solid state impact welding technology. The process uses electromagnetic force to accelerate one metal piece (flyer plate) onto another stationary metal piece. The velocities attained during this process range from 200 m/s~500 m/s [29, 109, 138]. The joining occurs on impact within microsecond magnitude [29]. Even in such short time period, the extent of heating is minimal in the joints. Therefore, metallurgically, no significant HAZ in MPW joints [19]. It is generally agreed that the joining mechanism is similar to explosive joining where the surface oxide is disrupted due to the jet action and metallurgical bonding is achieved between clean surfaces. However, the details of shock wave interaction and the resulting high strain rate deformation of the underlying microstructure are not clearly understood. Therefore, a systematic microstructure characterization effort has been initiated. The overall study involves understanding of crystallographic features near the interface, chemical composition changes near to the interface and modeling of the interfacial phenomenon using computational models. This

chapter presents selective results from welding process study, mechanical property tests and microstructure characterization of AA6061 joints.

The chemical composition of AA6061 is shown in Table 5.1. Before impact welding, the precipitates hardening AA6061-T6 was solutionized at 560 ℃ for 20 minutes following by air quench. Therefore, the annealed materials have lower yield strength and microhardness.

Table 5.1 Chemical Composition of AA6061 (wt%)

AA6061								
Mg	Si	Cu	Fe	Cr	Mn	Zn	Ti	Al
0.8-1.2	0.4-0.8	0.15-0.4	<0.7	0.04-0.35	<0.15	<0.25	<0.15	Bal.

5.3 Experimental procedure

5.3.1　Welding Actuators

Two types of workpieces, flat plates and tubes of AA6061 were welded by MPW. Accordingly both the flat bar actuator and the circular actuator (as shown in Figure 4.1) were used. Figure 5.1 presents the schematic drawing of the welding system for flat bar actuator (as shown in Figure 4.2). During MPW process, electromagnetic force is used to accelerate the flyer plate to collide against the target plate which is usually few millimeters away. The welding system mainly includes the power supply, the capacitor bank, the actuator, and being welded workpieces. Once the stored electric energy in the capacitor bank is discharged into the actuator, the primary current (i_1) induces a secondary current (i_2) in the nearby flyer plate. They flow parallel but in the opposite direction. Both the primary and the secondary current generate magnetic fields. However, due to the opposite phases of the resulting magnetic fields, the flyer receives a repulsive force (F) and collides against the target with 200m/s~500m/s collision velocity [29, 109, 138]. The surface oxide layer on the metal workpieces is then removed by jetting [139] and metallurgical bond is formed along atomic level clean surface. Meanwhile the impact welded interface undergoes high strain rate deformation. Taking the collision velocity 250m/s as an example, surface of the 0.254mm thick plate changed from flat to wave pattern with wave amplitude about 10μm, and then the PDV estimated strain rate is within the order of $10^6 \sim 10^7 s^{-1}$.
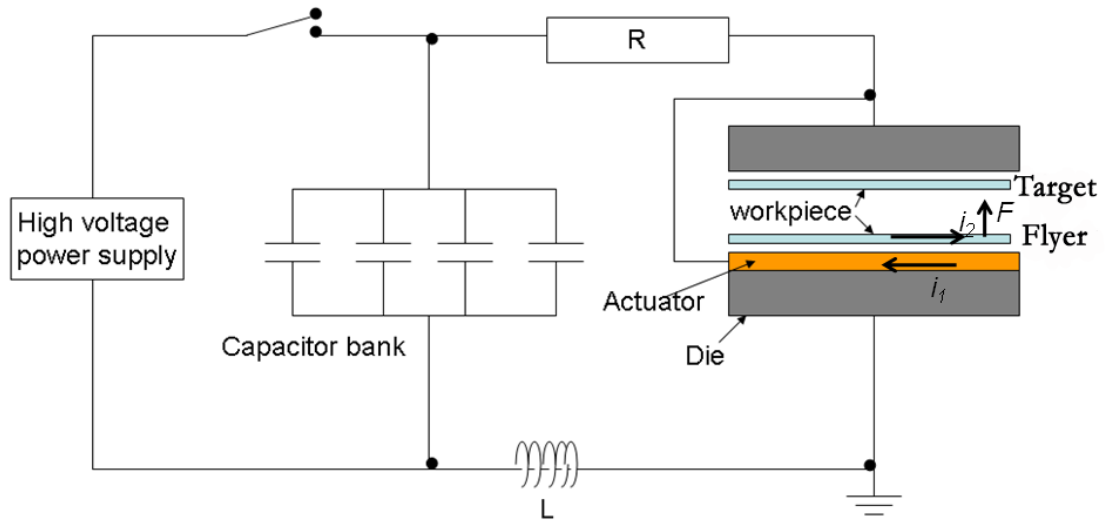
Figure 5.1 Illustration about MPW system for flat bar actuator.

5.3.2 Study on Process Parameters

The discharge energy level can be adjusted to make successful welding. The flat bar actuator was connected to the capacitor bank with 16kJ maximal output energy. A sequence of impact energy was tried at a fixed standoff distance. For the 0.5mm thick plate to plate, the minimal impact energy leads to successful welding on AA6061 plates are 4.8kJ with 210KA peak current. The welded plates are 0.254mm thick, 76.2mm wide and 101.6mm long. The standoff distance between the flyer plate and the stationary plate was 4.50mm and the overlap was 12.70mm. The tubular welding was conducted on a larger capacitor bank with 90kJ maximal output energy. The input energy for the tubular AA6061 welding was 45kJ with 860kA peak current. The outer and inner diameters for the AA6061-T6 tube were 50.80mm and 47.50mm, respectively. The diameter for the

AA6061-T6 rod was 40.89mm. There was a concentric cylindrical through-hole in the rod with diameter 25.40mm. The standoff distance was 3.30mm and the overlap was set as 19.05mm.

5.3.3   Impact Angle and Impact Velocity

The impact velocity was instrumentally measured and the typical collision velocity is about 250m/s. As a result, during impact welding, the welded interface deformed by shot blasting with high strain rate in the order of 10^7s^{-1}. The strain rate was controlled by a number of process parameters, such as the flyer plate traveling distance, the impact energy and the electromagnetic field frequency [131]. In this study, the flyer plate traveling distance was kept at 3.5mm and the welded region was about 12.7mm wide and 101.6mm long. The impact energy was controlled at certain levels ranging from 4.8kJ to 8kJ, and the electromagnetic field frequency was kept constant.

The mechanical properties of the joint were characterized at room temperature using lap shearing test, peeling test, and nanoindentation test. In most cases, the mechanical tests were carried out four times for each condition. The average values were determined from separate measurements. And the test setup is illustrated in Figure 5.2.
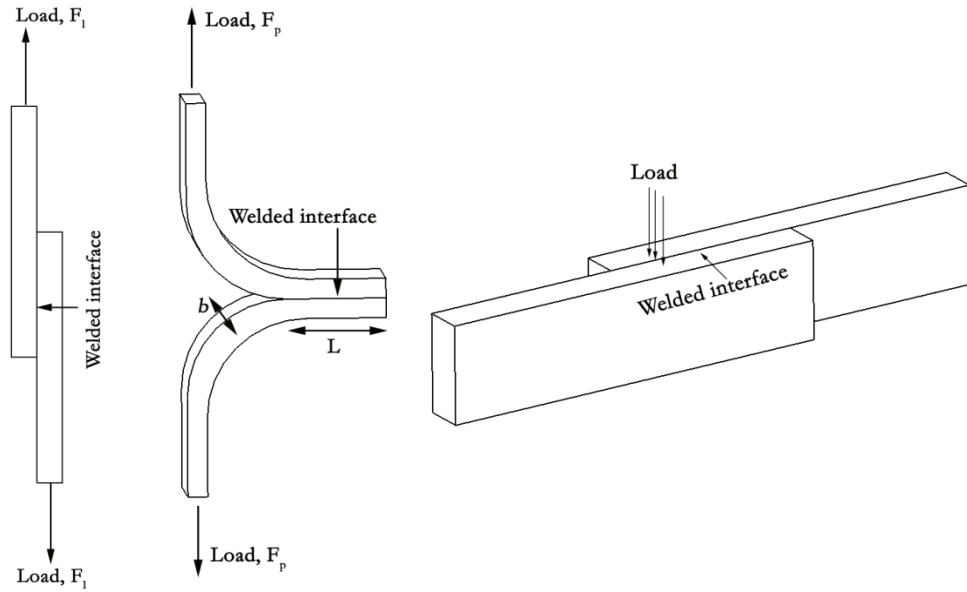
| (a)Lap shear | (b) Peeling | (c) Nanoindentation |

Figure 5.2 Illustration of mechanical tests.

5.3.4 Lap Shear Test

The lap shearing test is similar to tensile test, but the tensile axis is parallel to the welded interface as shown in Figure 5.2(a). It was examined at strain rate about $10^{-2}s^{-1}$ by using MTS 831.10 Elastomer test system. The specimen was prepared by slicing the welded plates as shown in Figure 5.3 from Walker Ceramax$^{®}$ precision grinding machine. The gage length is 100mm and the gage width is 12.7mm. The applied load generates shear stress on the welded region with shearing area (A_0) about 161.29mm^2. The load (F_l) and

displacement were recorded during test. The joint strength (MPa) was calculated by load

dividing the shearing area (F_l/A_0). The elongation and the strain (%) were determined

from the measured displacement.
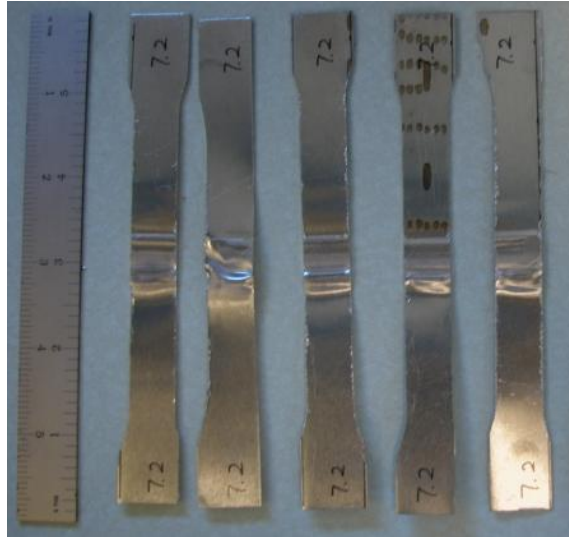
Figure 5.3 Samples for lap shear test

5.3.5 Peeling Test

The peeling test was also performed on MTS 831.10 Elastomer test system with the

tensile axis perpendicular to the welded interface as shown in Figure 5.2(b). And the peel

strength (F_p/b) was defined by force per unit length, as shown in Equation (5.1)-(5.3)

[140].

Assuming the total energy for peeling at constant speed is U, as shown in Equation (5.1), it includes surface energy γ, potential energy of applied load F_p, and the elastic energy due to shrinkage of the joint with strain ε.

$$U = \gamma b(L-l) - F_p(L-l) + \frac{1}{2}bdlE\varepsilon^2 \quad (5.1)$$

where γ is the energy required to fracture unit area of interface, b is he joint width, L is the initial length, l is the residual joint length after peeling, F_p is the applied load, d is the joint thickness, E is Young's modulus and ε is shrinkage strain. Since the energy is conserved and neglecting the viscoelatic losses:

$$\frac{dU}{dl} = 0 = -\gamma b + F_p + \frac{1}{2}bdE\varepsilon^2 \quad \text{Equation (5.2)}$$

And thus the peel strength is given by

$$\frac{F_p}{b} = \gamma - \frac{dE\varepsilon^2}{2} \quad \text{Equation (5.3)}$$

In present study, the joint thickness, Young's modulus and strain were constant and thus F_p/b presents the joint strength.

5.3.6   Nanoindentation Test

Nanoindentation test was conducted on the cross section of the welded interface as shown in Figure 5.2(c). The indenters crossed the interface and the spacing between each indenter was set as $5\,\mu m$. The tested length was $50\,\mu m$ on each side and the overall test length was about $100\,\mu m$.

5.3.7 Microstructure Characterization

Microstructure analysis was performed by using OM, EBSD and TEM. These specimens went through the standard metallographic grinding and polishing procedures and ended with colloidal silica polishing suspension in a Beuhler Minimet^{TM} automatic polishing system. The TEM thin foil specimens were prepared by focus ion beam (FIB) microscopy and the spacial relation between the samples were shown in Figure 5.4. The EBSD specimens were collected from the welded region, spalled region and the base metal. EBSD images were obtained from SEM equipped with TSL^{TM} EBSD detector. And standard image analysis methods were used to quantify the grain size and grain boundary misorientation. FEI CM200T TEM operating at 200kV was also applied for this study.
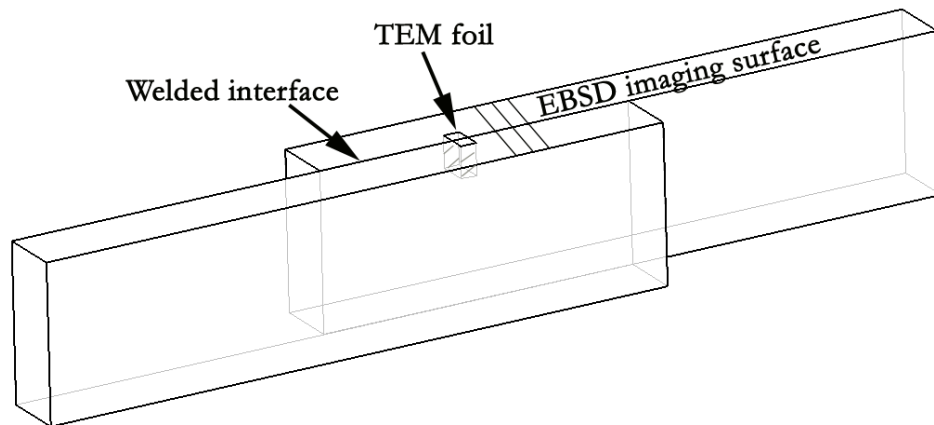
Figure 5.4 Schematic drawing of specimen from the welded interface.

Literature on MPW suggests the possibility of wave interface and adiabatic heating [7, 29, 34]. The wave length and wave amplitude is within millimeter range and can be observed by OM. Because of the adiabatic heating, it is speculated that along the interface, this localized heating may go above the recrystallization temperature. This may induce localized recrystallization of the deformed grain structure. If the temperature is above the melting point of the material, the grain structure may emulate the epitaxial condition observed in fusion welding process. The crystallographic orientation imaging analysis by EBSD and TEM will be able to elucidate this phenomenon. EBSD is SEM based technique and it allows identifying the microstructure and the crystallographic orientation from a single point. Therefore, by analyzing each individual point in a designated area, we can study the grain structure and grain boundary misorientations. Such information will not be obtained from either OM or SEM. For EBSD imaging, it is known that some regions show better diffraction quality while adjacent areas give poor quality patterns which cannot be indexed, possibly due to extensive plastic deformation [141]. The specific crystallographic orientations of grains are typically color coded with reference to a stereographic triangle. Points where the orientation cannot be indexed appear as black. TEM image and their diffraction patterns were also used to investigate the interfacial grain size refinement with higher resolution. High strain rate could also result in high dislocation density, which could be observed by TEM. By comparing the measurements from the base metal and the welded interface, we may be able to understand the deformation conditions close to the interface. For the scientific research, the results from

these investigations will contribute to the fundamental understanding of microstructure changes during MPW.

5.4 Results and discussion

5.4.1 Lap Shear Strength
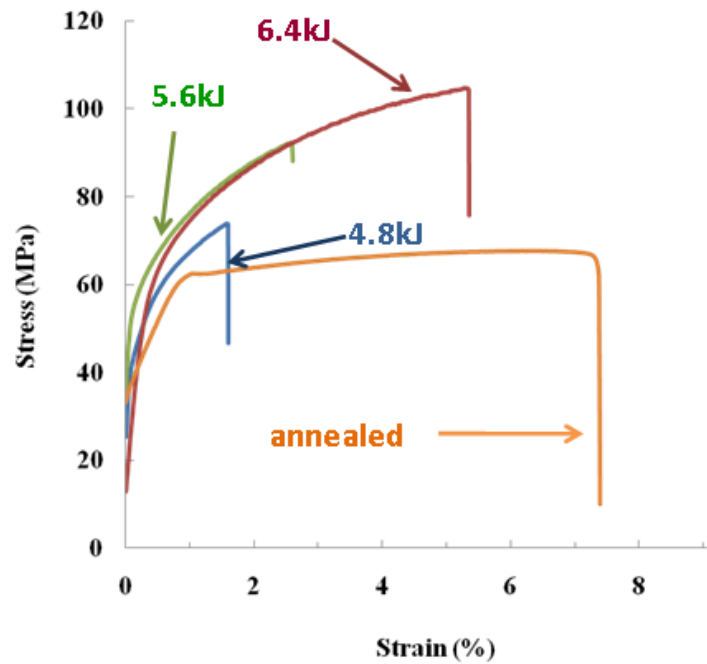
Figure 5.5 Lap shear test results from MPW joints.

Figure 5.5 is the summary of the lap shearing test on the impact welded AA6061 joints. Comparing to base AA6061 metal, as shown in Figure 5.5, the impact welded AA6061

joints from different impact energy levels all indicated an early onset of plastic deformation, and the values of the yield strengths and the ultimate tensile strengths were greater than that of the as-received base metal, presenting a tendency to increase with increasing impact energy. The impact welded samples had limited uniform elongation in contrast to the as-received base metal, which had fairly large uniform deformation before necking and failure. Thus, the ductility of the impact welded AA6061 joint was not as good as the as-received alloy. The uniform elongation increased with increasing strain rate. For example, the 6.4kJ impact joint had larger uniform elongation than 5.6kJ impact welded joint. The low strength and large ductility of the as-received AA6061 plate may result from the annealing process while the high strength and small ductility of the impact joints may cause by high strain rate strengthening. Additionally, it was interesting to point out that the fracture of the lap shearing test was out of the welded zone as shown in Figure 5.6.
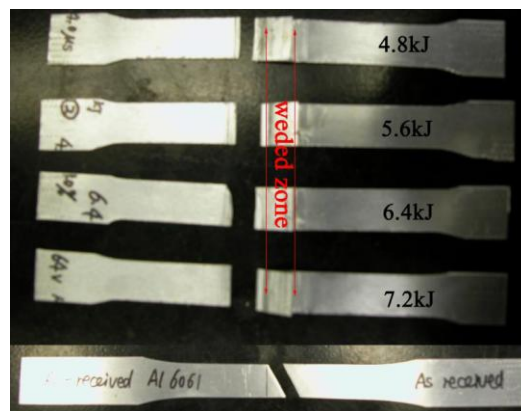
Figure 5.6 Fracture of lap shearing tests.

5.4.2 Peeling Strength

In order to have enough lap welded length, the welding sample from UP actuator was used for peeling test. Due to the configuration of the actuator, the overlap regions right above the actuator turns had stronger joint strength and thus the peeling strengths for all of the joints as shown in Figure 5.7 exhibited oscillations. It was caused by the welding actuator configuration and did not reflect the nature of the welded joint strength. The peeling strength also presented a tendency to increase with the increasing impact energy and the consequent strain rate. The low impact energy leaded to short welded length and weak joint. The peak peeling strength for all joints were tabulated in Table 5. 2.
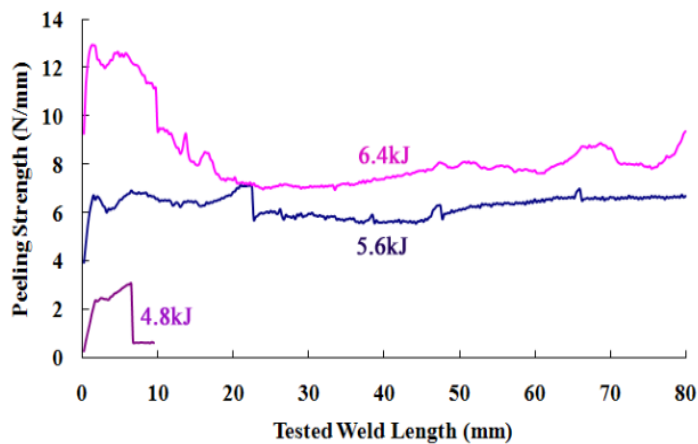
Figure 5.7 Peeling test results from MPW joints.

Table 5.2 Peeling test results for AA6061 joints

Flyer/Target	AA6061/AA6061		
Impact Energy (kJ)	4.8	5.6	6.4
Joint Peel Strength (N/mm)	>3.0	>7.1	>12.9
Failure Mode	through base metal	through base metal	through base metal

5.4.3　Joint Hardness

Microhardness values from nanoindentation test were plotted in Figure 5.8, showing a steady increase with deformation strain rate. The high strain rate hardening effect was found for AA6061. The hardened region across the welded interface was quite narrow for AA6061 joint, about 20 μm wide totally. And the impact hardened region was symmetrical with regard to the welded interface. The hardness values within these regions increased significantly. The test results indicated that the adjacent area had about 1GPa hardness while the welded interface microhardness was larger than the base metal and ranged from 1.3GPa to 3.8GPa. The high strength from impact interface was comparable to the first principle calculation results which were shown in Table 5.3. And it is necessary to point out that tabulated theoretical values are for single crystal pure aluminum rather than aluminum alloy.

Table 5.3 Theoretical and experimental hardness value of aluminum and the unit is GPa.

The VASP and the ABINIT value are for single crystal. [74, 142-144]

Materials	VASP	ABINIT	Theoretical	MPW
Al	3.67~3.73	3.68~3.71	1.4	<3.807
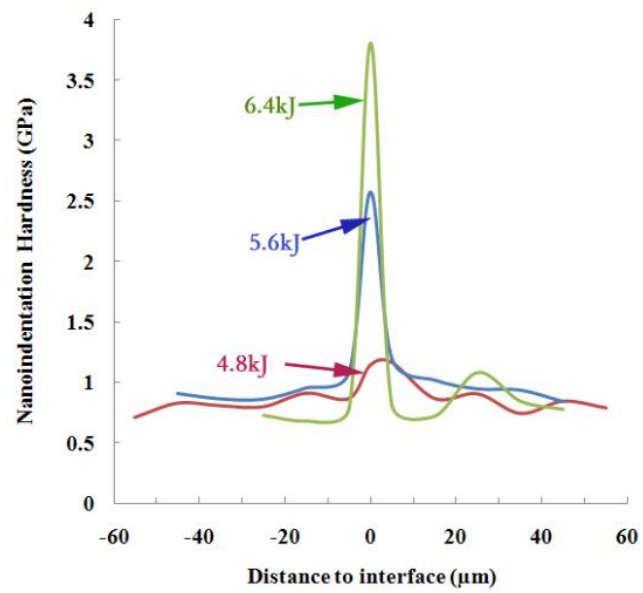
Figure 5.8 Nanoindentation test results from MPW joints.

5.4.4 Interface Grain Refinement

With high strain rate dynamic deformation, MPW process generates submicrocrystalline or nanocrystalline structure along the welded interface. The interfacial grains are different from the base metal coarse grain, which are usually in the order of one hundred micrometer. It is well known that refined grains offer very high strength, significant hardening, which are in the agreement with the mentioned mechanical testing results. This section studied the as-received base material microstructure and then compared with the impact welded interface microstructure.

5.4.4.1 As-received AA6061-T6 Microstructure
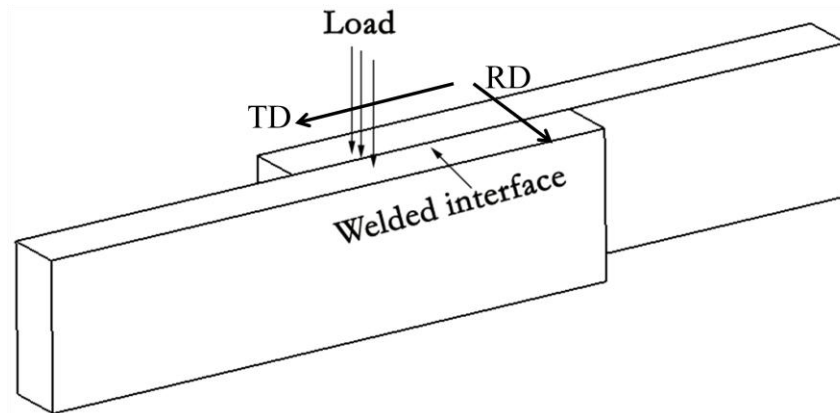
Figure 5.9 Definition of the transversal and longitude direction for joint cross sectoin.

In this research, the direction parallel to the impact welding line was defined as the longitude direction (RD) and the direction perpendicular to the impact welding line was defined as the transversal direction (TD) as shown in Figure 5.9. The load direction in this figure is the microhardness test load direction.

(a)   (b)
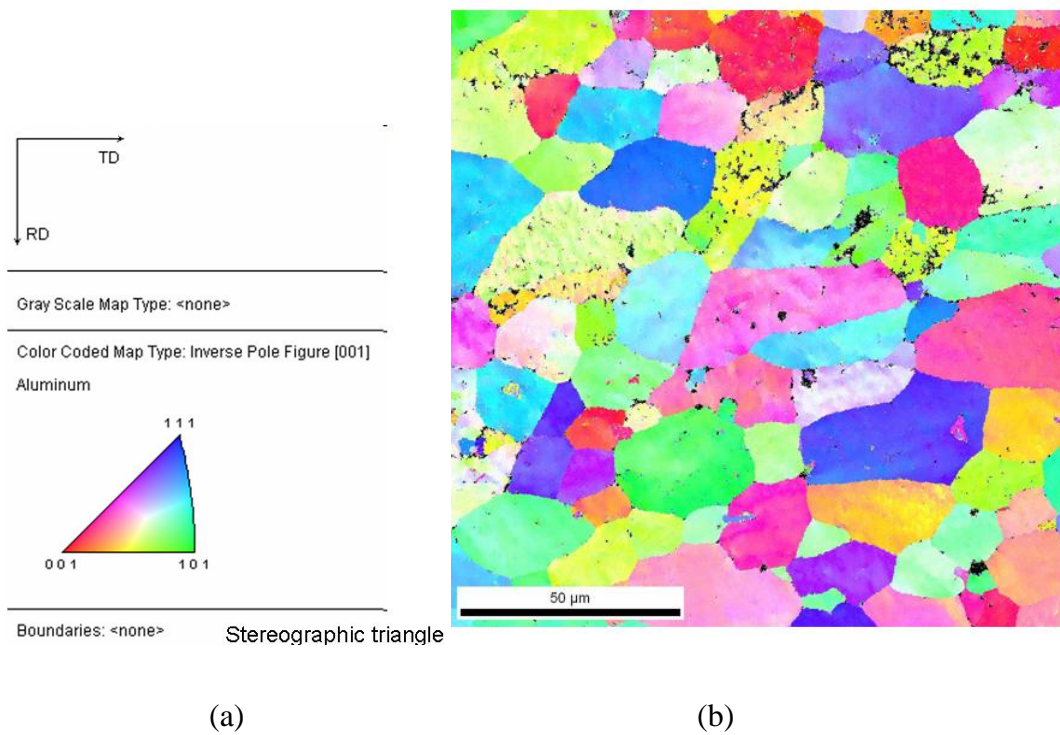
Figure 5.10 EBSD images indicate the grain orientation distribution of the as-received AA6061-T6. (a) Stereographic triangle (b) IPF image for as-received AA6061-T6 with image size $140\,\mu m \times 140\,\mu m$. The crystallorgraphic directions are parallel to the plane normal.

The color coded Inverse Pole Figure (IPF) maps are used to study the grain structure for the as-received and MPW impacted AA6061-T6. The IPF map obtained from the as-received base metal of aluminum alloy is shown in Figure 5.10. The image shows a well-developed equiaxed microstructure with average grain size $25\,\mu m$ and standard deviation $5\,\mu m$, as estimated by the image analysis routines that are part of the EBSD software TSL-EDAX^{TM}. Figure 5.10 also suggests a random grain orientation without any strong preferential orientation for polycrystalline structure.

5.4.4.2 Impact welded AA6061 interface microstructure

The interface microstructure of the seam welded AA6061-T6 plates is presented in Figure 5.10. The EBSD images in Figure 5.11 shows that the grains near the bonded interface are highly deformed along the impact direction. The micrographs also show significant local misorientations and sub-grain formation with higher grain boundary angles. At the same time, the grains at the interface are highly deformed and show significant subgrain formation. These sub-grains can be quite small (about $1\mu m$) and some localized misorentations are relatively high.
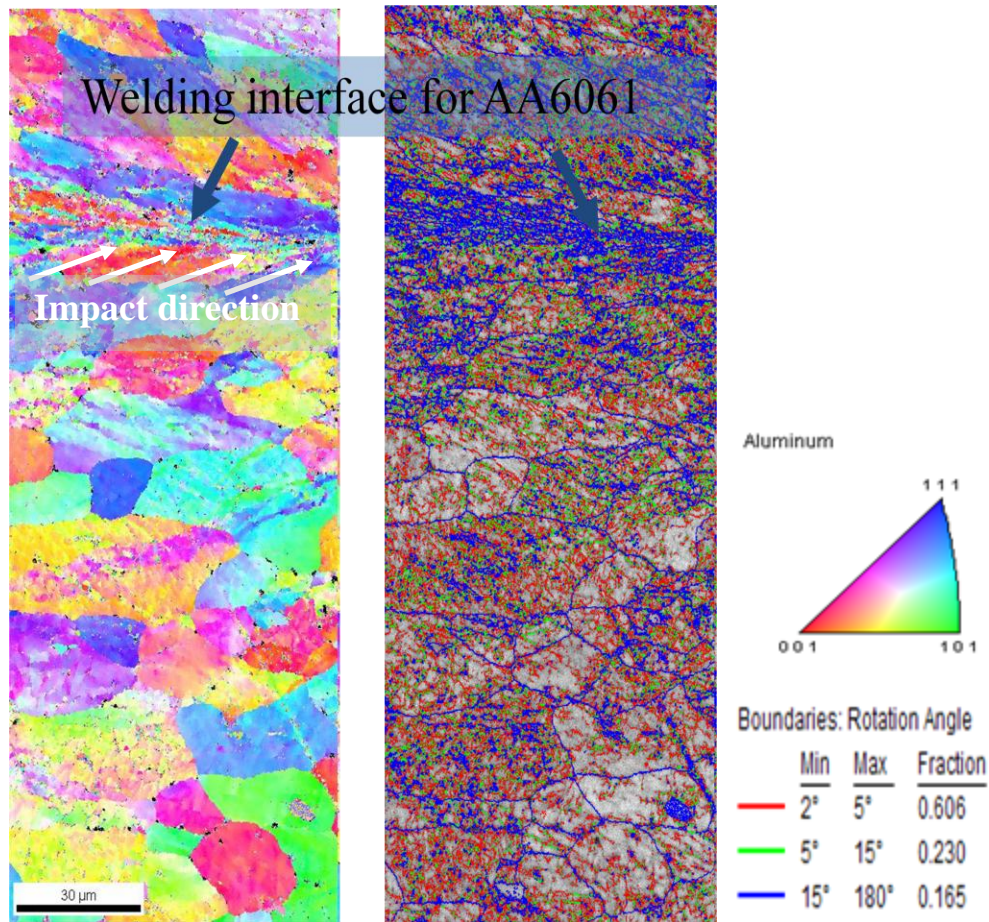
(a)Grain orientation map (b) Index of grain boundary angle (c) Figure legeng

Figure 5.11 EBSD measurements of welded interface from 6.4kJ welded AA6061 joint.

It is interesting to note that a grain size reduction of one order of magnitude occurs within a short duration, about 10^{-6}s, which was measured by PDV. This phenomenon is similar to the interface made by EXW [145] and the mechanically-induced ultrafine grains in the near-surface layer during shot peening [146]. The continuous nature of the transition from the base metal to the refined interface region strongly supports the model that severe localized plastic flow leads to interface bond formation. Together with jet action, the high

local strain is also essential in breaking up the surface oxides and allowing formation of metal-to-metal bonding. There is no evidence of melting in this region of the microstructure. Previous researchers have not reported such microstructure changes of the similar metals of MPW joints.

It is important to note that high impact rates will introduce adiabatic heating. It is incidental in our case that the fine grain structure was frozen in without much recrystallization or melting due to adiabatic heating and followed by rapid cooling. If adiabatic heating increased close to the melting temperature, we would have observed a planar solidification with epitaxial growth as the HAZ grains. Since we observed very fine grain structure at the interface with no epitaxial orientation relationship as shown in Figure 5.10, the extent of melting is concluded to be minimal. Future work is being continued to evaluate the grain structure under different energy conditions and also to simulate the adiabatic heating using computational models to evaluate local strains, strain rates, and the extent of heating.

The high strain rate deformation induced from MPW leaded to interface grain refinement. This result is similar to other various individual severe plastic deformation (SPD) processes which also lead to final equiaxed nanocrystalline structures despite the different strain paths[147]. The welded interface exhibited UFG structure, which were of several decade nanometers in diameter as shown in Figure 5.11 and Figure 5.12. EBSD

measurement presented a gradient in grain size from the impact surface to the base metal. Such grain size gradient was caused by strain and strain rate gradients from high speed impact welding process. The grain size changed from nanometer scale to micrometer scale in a continuous manner from the interface to the base metal. The interfacial grains transformed into essentially equiaxed nanocrystalline structures. And the ultrafine grains were surrounded by high angle boundaries with the angles larger than 15°. These high angle boundaries impeded the dislocation motion and strengthened the joint interface. The EBSD images in Figure 5.11 indicated that the submicron grains near to the impact welded interface were elongated along the impact direction, with average grain boundary misorientation of 5°~15° and boundary spacing of 10μm. Such interfacial grain refinement was also attributed to the interface strength increasing, which is in confirmation with the Hall-Petch relation. Figure 5.12 was the TEM image from 6.4kJ welded AA6061 interface, which clearly showed that the grain size decrease from 40μm in as-received base metal to 50nm in the impact interface. The sharp spot diffraction pattern from base metal changed to spot with ring diffraction patter adjacent to the welded interface, which suggested the fine grain structure near to the interface.
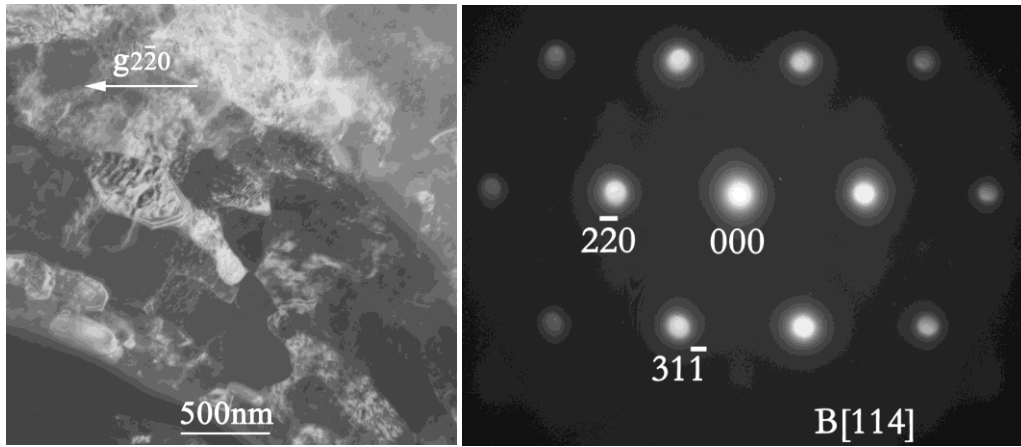
(a) Base metal coarse grain structure
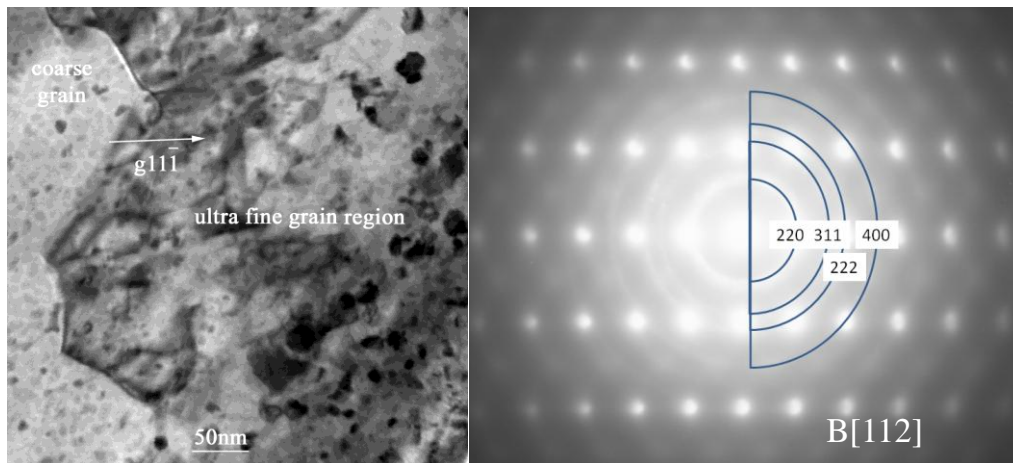
(b) Interfacial fine grain structure

Figure 5.12 TEM images from AA6061 joint showing grain refinement after high strain rate deformation. (All images are TEM BF image)

5.4.5   Dislocation Density for Interfacial Grains

The dislocation density depended on the deforming process, the strain rate, the deformation mode and the materials properties such as SFE (Al is ~160mJ/m^2) and lattice structure [148]. The high strain rate produced grain interior dislocation played a key role to the mechanical behavior of the impact joint. The increase of the joint shear strength, peeling strength, and hardness at high strain rate deformation in Figure 5.5, 5.7, 5.8, can be explained by the increase in dislocation density and the dislocation interaction at the grain interior. Because the impacted welded AA6061 interfacial grains were characterized by high dislocation density and the dislocation tangles were shown in Figure 5.13(b). The dislocation distributed at the interior with tendency to rearrange as cellular structure as shown in Figure 5.13(c). This verified that little amount of dynamic recovery occurred on the high strain rate induced dislocation, because the annihilation and rearrangement were initialed to form the cellar structure. The cell walls were loosely defined but the cell interiors were almost dislocation free, which was also reported from other SPD process [147]. TEM results at Figure 5.13 also indicated that many parallel dislocations aligned near the grain boundaries with very small interval.

(a)   (b)   (c)
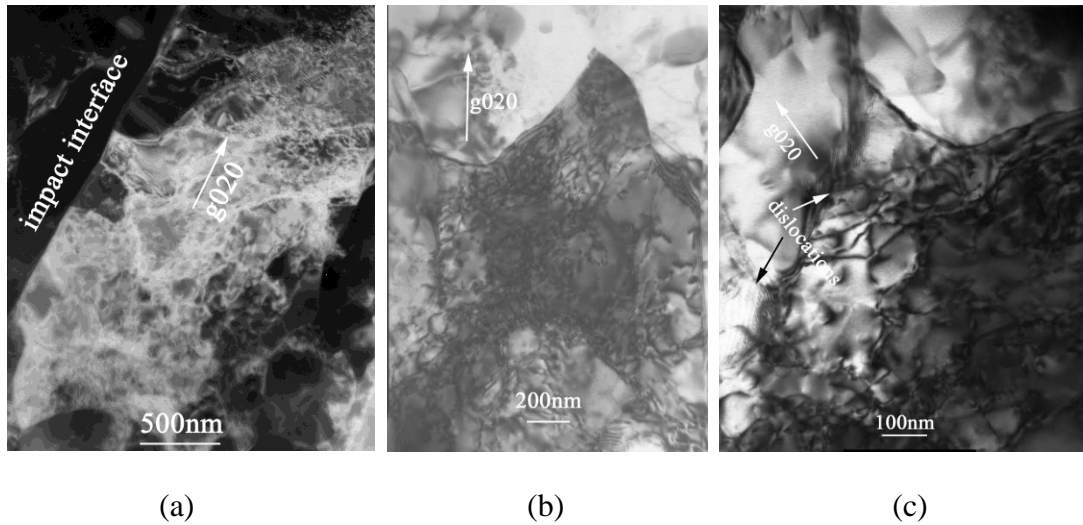
Figure 5.13 Dislocation density increase and formation of cellar structure in AA6061

joint. (TME BF image and the beam direction is along [001].)

5.4.6   Spalling Microstructure on Tubular Joint

It is also observed that delamination occurred away from the impact regions at the inside

surface of the rod, while welding AA6061-T6 tube to rod under high energy conditions.

The spalling occurred on the rod away from the welded interface. The crystallographic

orientation of the microstructure in spalled region was evaluated with the EBSD

technique, and the results are discussed as below.

In tubular MPW, extensive material damage was observed in the regions away from the impact interface on which the electromagnetic impact load was applied, as shown in Figure 5.14(a). This damage is attributed to spalling, which is dynamic fracture by strong shock wave loading [149]. Spalling often occurs in high rate impact processes when critical geometry and discharge energy levels are exceeded. It is noteworthy that the energy levels used in this experiment were at least 10 times higher than the earlier linear seam welding. A schematic illustration of the process is shown in Figure 5.14(b). On impact of the flyer work piece, a stress wave compresses the materials and propagates into the specimen. Upon reaching the far side, these waves are reflected back and the material subjected to tension. An interference of reflected and incoming waves sets up temporally and spatially varying compressive and tensile loads. As a result, the regions in tension will be prone to fracture and spalling. It is typical that the thickness of the spalled scab has a thickness similar to that of the flyer causing the damage and this pattern is seen in our experimental result.
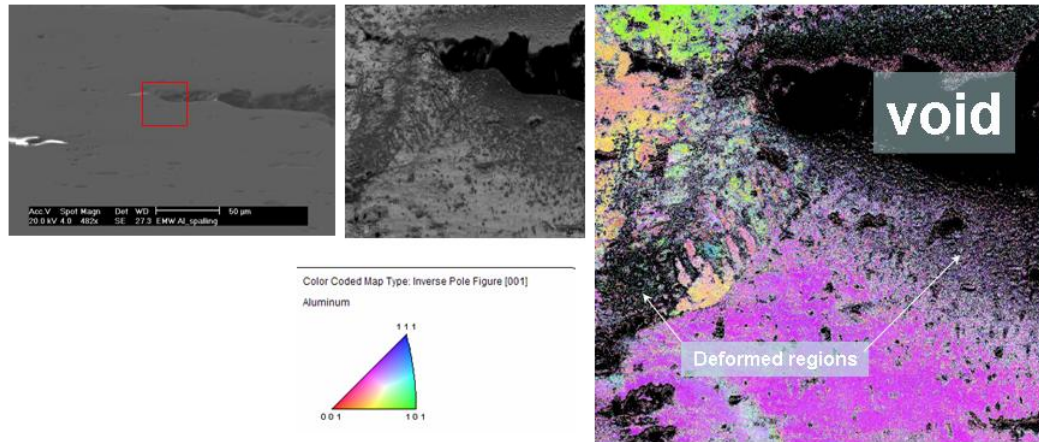
Figure 5.14 (a) OM image of spalled region in an AA6061-T6 rod away from the welded region; (b) Schematic illustration of the physical processes that may lead to spalling; (c) EBSD results from the spalled region. The color code corresponds to spatial orientation of grains with reference to stereographic triangle. The large dark regions are the voids and the black speckles are the regions where good diffraction could not be obtained.

To understand the interaction between spalling and grain structure, an EBSD scan was performed close to the spalled region. The IPF image, as shown in Figure 5.14, shows extensive dark regions due to poor diffraction pattern quality. It is well known that severe strains and micro-void formation may lead to poor diffraction quality, even though the sample surface is prepared properly. It is interesting to note that the diffraction quality around the spalled region is poorer than the linear welded regions shown in Figure 5.11, which indicates that the strain gradients near the spalled regions were very large and continuously decreased away from the interface. This concentrated deformation is tentatively attributed to alternating heavy compressive and tensile plastic deformation due

to the progression of shock waves through the material. This qualitatively supports the spalling mechanism that is reported in the literature [36]. Further analyses are being conducted to understand these spalled regions as a function of discharge energy, geometry and local grain boundary properties of the base metal so that the spalling can be avoided in MPW process.

5.5 Conclusion

MPW can be used for different geometry workpieces and both linear welding and tubular welding on AA6061 were studied. Microstructure characterization of MPW on AA6061-T6 by EBSD indicates almost one order of magnitude grain refinement in the welded interface comparing to base metals. The data also shows large crystallographic misorientations between these grains. These experimental results confirm the hypothesis of localized high strain rate deformation near the welded interfaces during high velocity impact. The results also show that the interface is formed mainly by true solid state bonding. It was also found that the shear strength, peeling strength and hardness of the joint interface increased with the impact energy level (increase of strain rate) and greater than that of the as-received base metals. The possible hardening mechanism include: (1) formation of ultrafine grain structure along the welded interface, with boundaries ranging

from very high angle to low angle varieties; (2) increase of the dislocation density present in grain interior and tendency to form cellar structure.

Significant spalling was observed away from the welded region after the tubular MPW process. EBSD results from the spalled region indicate the strain gradient and extensive plastic deformation. The results qualitatively support the hypothesis of localized deformation in the bulk matrix away from the impacting surface due to the progression of alternating compression and tension deformation waves. However, the exact condition for spalling to occur in MPW has not been fully understood and is currently underway.

Chapter 6 Magnetic pulse welding on copper alloy 110

6.1 Abstract

Copper (Cu) alloy is favored by MPW because it has relatively high electrical conductivity. This study indicated that 0.5mm thick Cu110 plates could be welded with discharge energy greater than 4.8kJ. By PDV, the impact process parameters for Cu110 joints were systemically studied and the weldability map was developed with regard to the impact velocity and impact angle. Mechanical test on Cu110 joints indicated high strain rate hardening effect because the joint presents significantly greater microhardness than the base metal. And microstructure study from TEM revealed that the increasing hardness is from the mechanical twins, the microband and the lamellar structure which were generated by dynamic plastic deformation during impact welding.

6.2 Introduction

116

MPW is a rapid process and the measured rise time for copper welding is 9~12 μs. The estimated strain rate on the welded interface is about $10^7 s^{-1}$, which results deformation twins. Deformation twins were widely observed for polycrystalline copper with grain size from micrometer to nanometer after severe plastic deformation. The proposed twinning mechanism for coarse grain (~1 μm) is pole mechanism activated at high local stress and for fine grains (~100nm) dependent on partial dislocation emission from grain boundary and boundary conjunctions [150]. The possible twinning mechanism for MPW Cu joint was discussed in section 6.4.5. The impact welding process also produced adiabatic heating along the welded interface. For shock load materials, the calculation from constitutive equation indicates the adiabatic heating leading to recrystallization [151]. And then the submicron (~0.1 μm) grain was produced in polycrystalline copper alloy [151].

For this study, Cu110 plates were welded by flat bar actuator with various impact launch angles. The welding system is same as aluminum alloy welding system as described in section 5.3.1. Two independent optic fiber laser beams connected to multiple channels of PDV and used to measure the impact velocity at different locations. The impact angle was calculated from the velocity time profile as discussed in section 4.3.3. The joint mechanical property and welded interface structure were examined. The contribution of deformation twins, microband and grain refinement to the joint mechanical properties was studied.

6.3 Experimental procedure

6.3.1 Study on Process Parameters

The Cu110 plates used for welding were manufactured by cold rolling and the composition is shown in Table 6.1, which is near to pure copper.

Table 6.1 Chemical composition of Cu110

Cu110 (wt%)	
P	Cu
0.015-0.04	Bal.

The as-received copper plates were cut into rectangular shape as 76.2mm wide and 101.6mm long. The width for the lap joint was set as 12.7mm and the other process parameters varied as shown in Table 6.2. The sample thickness is large than the skin depth. (Skin depth of copper is 1.5 μm at 1 GHz.) Design of experiment (DOE) was conduct for four variables and they are the flyer plate thickness, the standoff distance, the initial launch angle and the impact energy level. In order to figure out the effect of each variable, they were set at four or five different levels. And for each individual test, the

flyer plate velocity history was captured at two different locations by two PDV channels. The current history was measured by Rogowski coil. The peak current ranged from 204kA to 300kA and the rise time was about 9~12 μs. The energy level was set up to 8kJ because extra impact energy leads to arcing and degrades the joint quality.

Table 6.2 Process parameter variables ('-' indicated not attempt)

Variables	Low	→→→				High
Thickness (mm)	0.09	0.12	0.254	0.34	0.5	-
Standoff distance (mm)	1.15	2.45	2.60	3.15	4.5	-
Initial launch angle (°)	0	5	10	15	20	30
Impact energy (kJ)	4.8	5.6	6.4	7.2	8	-

According to Table 6.2, for the full factor experiment, there would be $5 \times 5 \times 6 \times 5 = 750$ tests in total. Among all the variables, the standoff distance significantly affects the impact velocity. Insufficient distance results less acceleration for the flyer plate and jet was not able to take place. It is known that the electromagnetic energy transferred into the flyer kinetic energy and potential energy after discharging the welding system. Therefore, too much standoff distance reduced the acceleration efficiency and also brought noise signals for PDV measurement. With the assistant of FEA from LS-DYNA®, the standoff distance was selected to be 3.15mm for all of the tests and thus the total experiments

number reduced to 150.

6.3.2   Mechanical Test

The Cu110 joints were also examined by lap shear test, peeling test and nanoindentation test as AA6061 joints discussed in section 5.3. And the testing details will not be repeated here.

6.3.3   Microstructure Characterization

The microstructure of welded Cu110 joint was characterized by OM, SEM and TEM. The impact welded cross section samples were polished and etched by perchloric acid solution. Thin foil with about 200nm thickness was prepared by FIB with final cleaning voltage at 5 keV. The deformation twins were characterized on these foils by a FEI CM 200T TEM operated at 200kV.

6.4 Results and discussion

6.4.1   Weldability

The impact velocity was instrumentally measured and the profiles were shown in Figure 6.1, in which the typical collision velocity is about 250m/s. As a result, during impact welding, the welded interface deformed by shot blasting with high strain rate in the order of $10^7 s^{-1}$, which was controlled by a number of process parameters, such as the flyer plate thickness, its traveling distance, the impact energy and the electromagnetic field frequency [131]. In this study, the flyer plate traveling distance was kept at 3.15mm and the welded region was about 12.7mm wide and 101.6mm long. The impact energy was controlled at certain levels ranging from 4.8kJ to 8kJ, and the electromagnetic field frequency was kept constant.
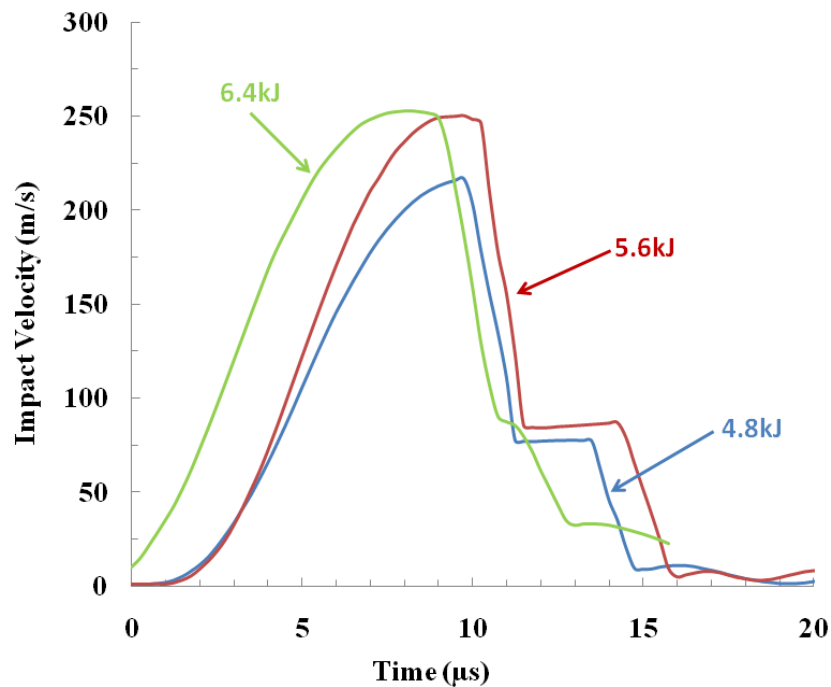
Figure 6.1 Instrumentally measured impact velocity profile from MPW on Cu110.

The symmetrical study on process parameters indicated that plate thickness played an important role for welding process. With impact energy larger than 4.8kJ, the thin plates with 0.09mm and 0.12mm thickness were torn at the edge of the target plate and failed to weld together. For the plate with 0.5mm thickness, it only showed deformation at the overlap region but bonding was seldom reached. Therefore, 0.254mm thick plate was intensively studied and its weldabiltiy map with regard to impact velocity and impact angle were shown in Figure 6.2. The successful welding occurred when the impact velocity was greater than 250m/s and the impact angle was in range of 2°~7°. It was also found that impact angle was smaller than the initial launch angle. For 20° and 30° initial launch angle, no plates were welded. One side of the flyer plates loaded for these actuators were bent into 20° and 30° before impact and they were electromagnetic formed into flat shape after impact only no welding occurred. Therefore, the initial launch angle should be controlled larger than zero degree and smaller than 20°.
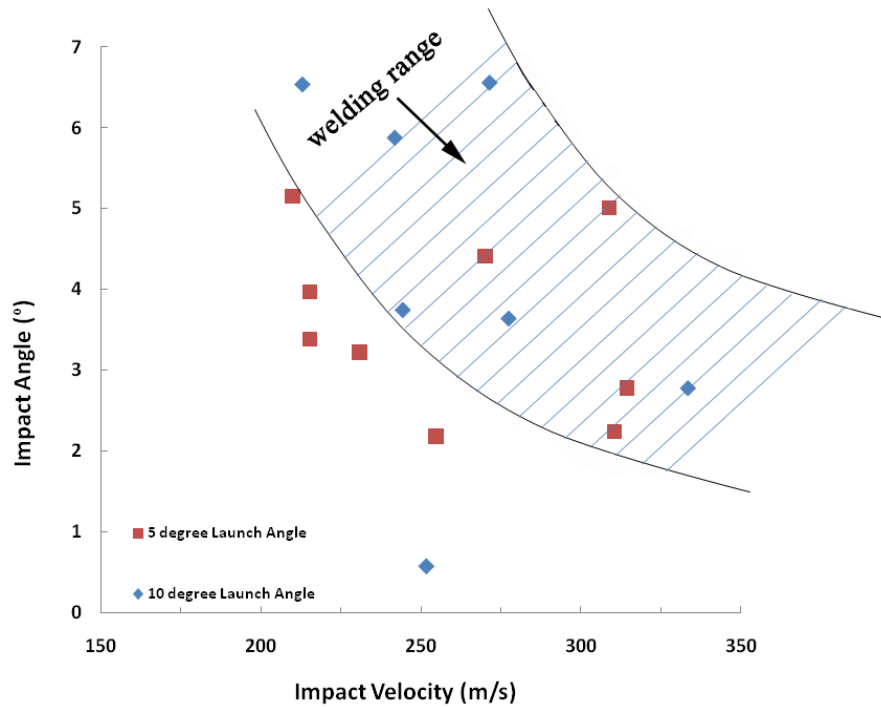
Figure 6.2 Weldability map for Cu110 joints of 0.254mm thick plates.

6.4.2 Lap Shear Strength

Figure 6.3 is the summary of the lap shearing test on the impact welded Cu110 joints. The joint behavior was similar to the as-received base metal with slightly higher tensile strength and less elongation. They both presented large uniform elongation beyond 10%. The joint from 4.8kJ showed abnormal behavior because the joint was weak and brittle. After the applied shear stress, all of the joints did not break and the sample failed out of the welded region on the base metal as shown in Figure 6.4.
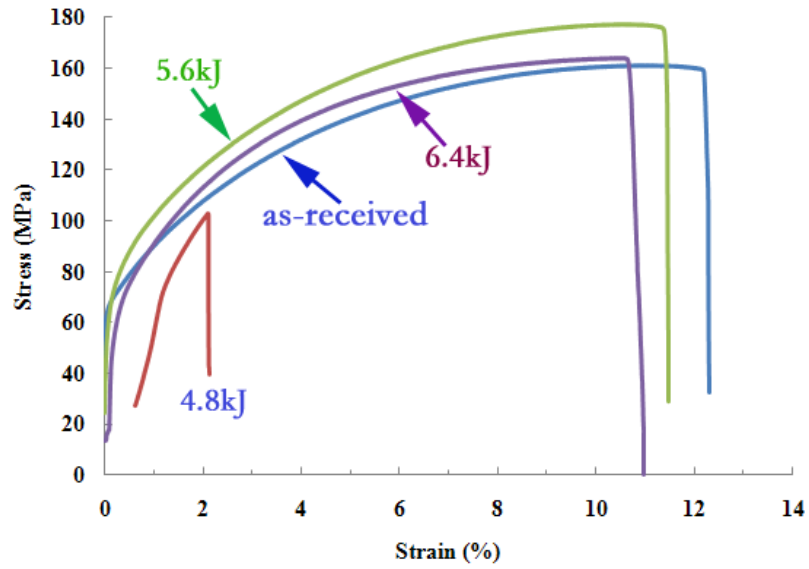
Figure 6.3 Lap shear test results from MPW joints.

Figure 6.4 Fracture of lap shearing tests.

6.4.3 Peeling Strength

Table 6.3 Peeling test results for Cu110 joints

Flyer/Target	Cu110/Cu110		
Impact Energy (kJ)	4.0	4.8	5.6
Joint Peel Strength (N/mm)	0.9	>10.3	>11.4
Failure Mode	through interface	through base metal	through base metal

The peeling results were summarized into Table 6.3. And the average values of the recorded peeling strength for each joint were tabulated into it. The peeling strength presented a tendency to increase with the increasing impact energy and the consequent strain rate. And the low impact energy led to weak joint. For 4.0kJ welded joint, the target plate and flyer plate were pulled apart and the joint was open. For the other higher impact energy level, the joint itself were not pulled apart but the base metals fractured during peeling process. In other words, some of the peeling failure was on both the base metal and the joint itself. It is also important to point out that the strength in Table 6.3 was not the maximal strength to open the joint, but was the maximal recorded strength to break the joint, which may cause by base metal fracture or opening of the joint. And the fracture samples welded at 5.6kJ were shown in Figure 6.5. SEM image was taken from

the opened area on the joint and the fractographic images present ductile fracture surface.

<div align="center">(a)   (b)</div>
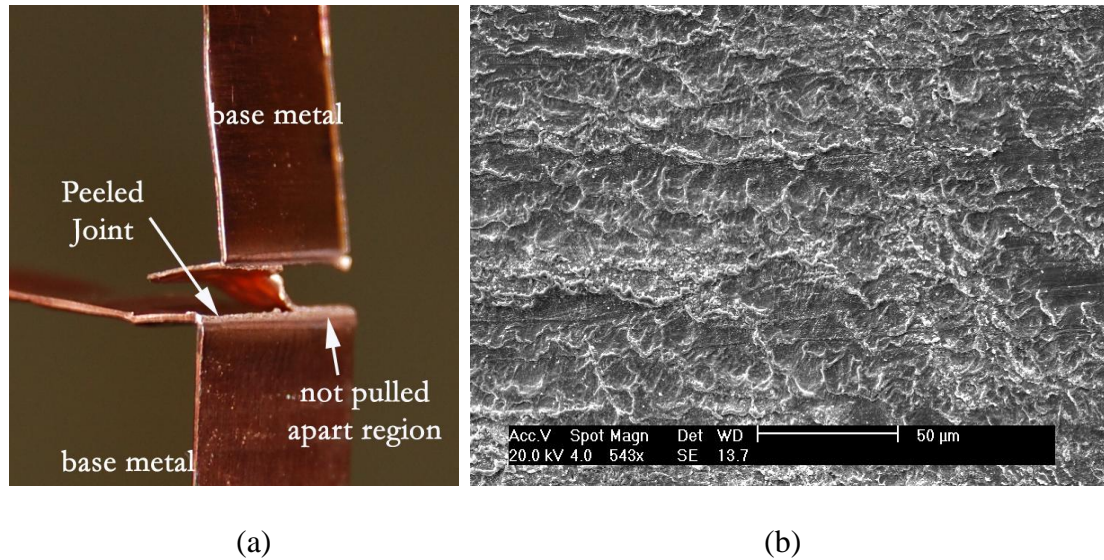
Figure 6.5 (a) Samples after peeling test, (b) fractographic image from SEM. The joint was made at 5.6kJ.

6.4.4 Joint Hardness

Microhardness values from nanoindentation test were plotted in Figure 6.6, showing an increase with deformation strain rate. The high strain rate hardening effect was found for Cu110 joint. The hardened region across the welded interface was quite narrow, about 40 μm, and it did not show symmetrical hardness with regard to the interface. Comparing

to the base metal, the hardness values within these regions increased significantly. The base metal hardness ranged from 1.5~2GPa and the interface microhardness values were up to 2.878GPa. The impact strengthening on the interface was comparable and less than the first principle simulation by higher than the theoretical value. The increase of the base metal hardness within the tested region was also attributed to the high strain rate hardening effect.

Table 6.4 Theoretical and experimental hardness value of copper and the unit is GPa. The VASP and the ABINIT value are for single crystal. [74, 142-144]

Materials	VASP	ABINIT	Theoretical	MPW
Cu	3.42~3.45	3.61	2.2	<2.878
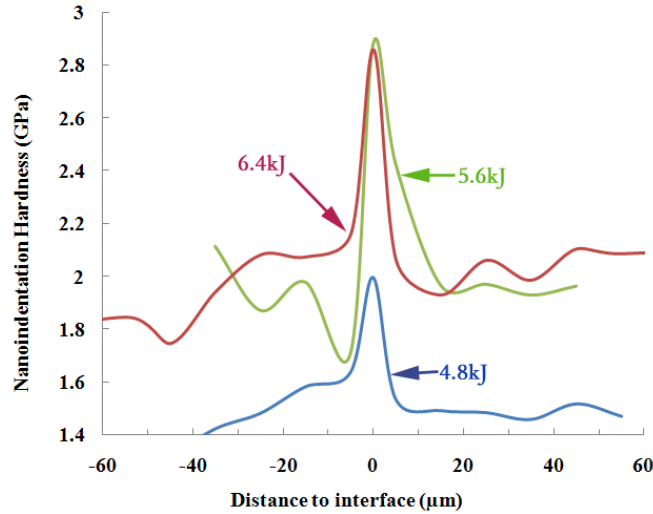
Figure 6.6 Nanoindentation test results from MPW joints.

6.4.5 Impact Induced Deformation Twins

High strain rate deformation is prone to induce deformation twins in low SFE facial center cubic (FCC) structure, which would cause grain subdivision process [147, 151-154]. Dislocation slip in low SFE materials was usually supplemented by twinning, in other words, the twinning microstructure hardened the materials. And the SFE for copper is low about $80mJ/m^2$. The OM images in Figure 6.7 presented the evidence for deformation twins on the Cu110 joint and the twinning density increases with the impact energy. The mechanical property tests indicated that the joint hardness is much higher than that of the as-received base metal. The increase of the joint strength, peeling strength and hardness is therefore attributed to the occurrence of the deformation twins.
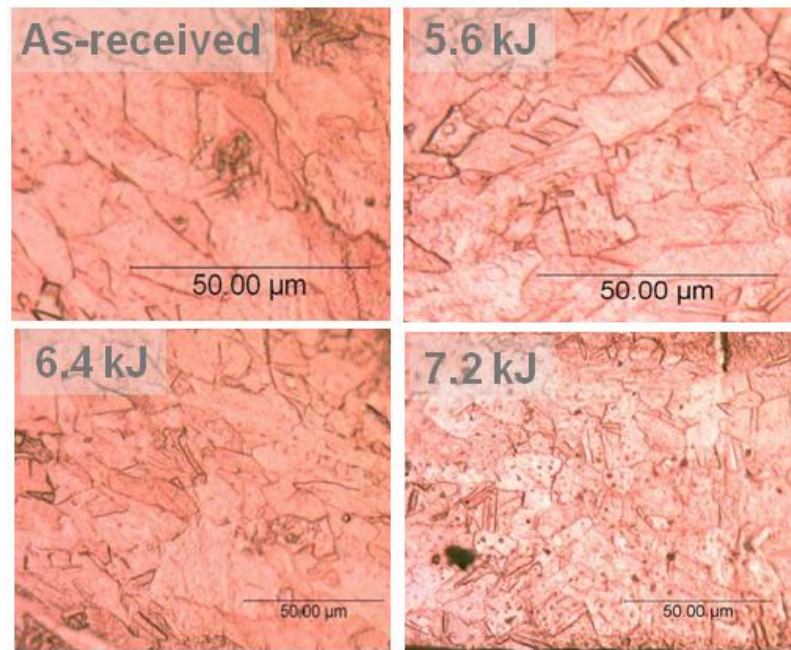
Figure 6.7 Deformation twins observed from OM on MPW Cu110 joint.

The twinning structure was also clearly visible in very fine scale structure as shown in the TEM image in Figure 6.8. And the diffraction pattern presented that twins was in (111) plane. The nano-scale twins expanded the narrowly spaced lamellae structure. Such lamellar structure has been demonstrated in the conventional cold rolled materials with high strain [155, 156]. The width of the nano-twins observed was constant in a range about 10nm, which is much smaller than the width of annealing twins in sub-micrometer [150]. During impact welding process, the PDV estimated shear strain rate was in the order of $10^6 \sim 10^7 s^{-1}$, the dislocation emission from the grain boundary and formed

mechanical twins, which suppressed the dislocation slip. Additionally, the nanometer scale lamellar grain structure served as barriers and inhibited the dislocation slip. The nano-twins cut through the lamellar structure and extended to the entire grain. It was proposed that such deformation twins were formed via partial dislocation emission from GBs and GB junctions are predicted by MD simulations [157]. Therefore, the mechanism for nano-twins was based on the high strain rate deformation, which leaded the coarse grain into nanometer thick lamellar and divided into twin-matrix lamellae. It was necessary to point out that all the twinning structure shown in Figure 6.7 and 6.8 was mechanical twins, because any pre-existing annealing twinning would be destroyed at the strain rate level in which the deformation twins take place [150]. These results also suggested that the deformation twins are the main deformation mechanism for copper alloy at high strain rate impact [150].
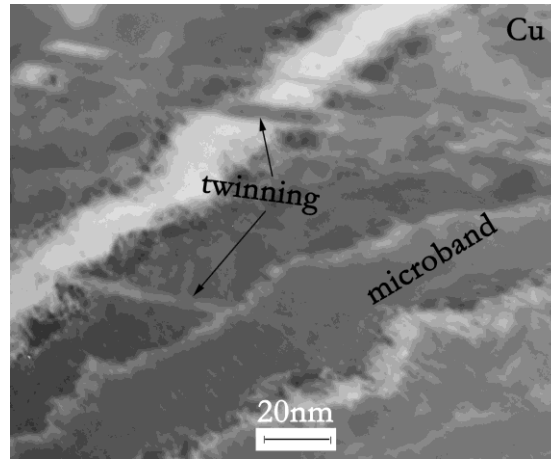
(a)
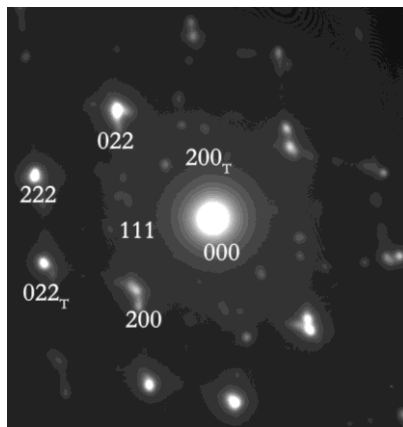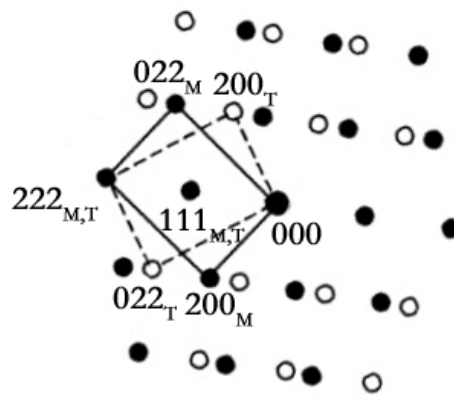
(b)   (c)

Figure 6.8 (a) image of deformation twins (indicate by arrows). (b) Twinning diffraction

obtained with electron beam on [110] direction. (c) Index for twinning.

6.4.6   Lamellar Grain Adjacent to Welded Interface

At the region adjacent to the welded interface, the lamellar grains with clearly defined boundaries presented and they replaced the equiaxed grain structure as shown in Figure 6.9. The direction of the lamellar band approximately followed the flyer plate impact direction. Upon the impact moment, short range but massive dislocation motion was activated and the coarse grains were divided and resulted into the lamellar structure. The lamellar width was less than 100nm and along the preferentially oriented direction. This observation demonstrated the high strain rate induced plastic deformation from impact welding process.
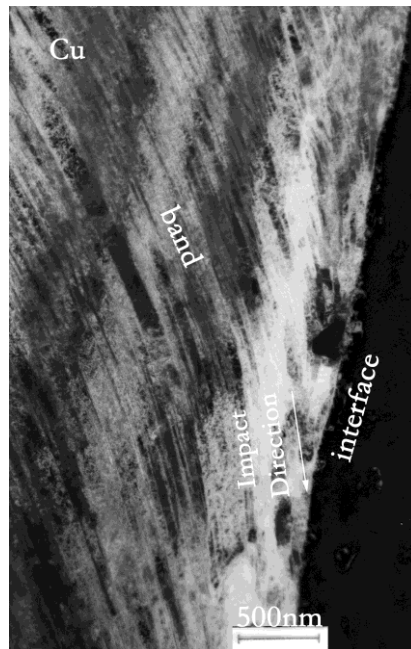
Figure 6.9 Lamellar structure near to the welded interface

6.5 Conclusion

MPW can join Cu110 plates together with high strain rate deformation and the strain rate was estimated in order of $10^7 s^{-1}$. The strain rate increases with impact energy level. The process parameters for Cu110 MPW were systematically studied and the weldability map was developed with regarded to the impact velocity and impact angle. The joint presented greater strength than the base metal. And the failures for the lap shear test and peeling test were out of the welded region. It was also found that the shear strength, peeling strength and hardness of the joint interface increased with the strain rate increasing and greater than that of the as-received base metals. Microstructure study suggested the formation of lamellar grains and deformation twins. Both the lamellar grains and the deformation twins were within nanometer scale, and the twins expanded through the lamellar grains. They are the possible hardening mechanisms.

Chapter 7 Magnetic pulse welding on Cu-Al dissimilar materials

7.1 Abstract

MPW was applied to lap joining on AA6061-T6 and Cu101 plates. The microsecond-duration process introduced high strain rate deformation (about $10^7 s^{-1}$) into the plates. Microhardness tests indicate that the welded interface has a higher hardness than the base metal. SEM revealed that the interface had wave morphology with discontinuous pockets of an intermetallic phase. TEM revealed elongated subgrains, lamellar microbands, micro-twining, dislocation cells, submicron and nano-crystal grains, and articulation teeth-like grains. The high dislocation density and large misorientation of grain boundaries accommodated the deformation. Atom probe tomography suggested that the intermetallic phase formed across the interface. These results indicate that the refined grain structure with large misorientation and intermetallic phase along the welded interface are the reason of high bonding strength of the weld.

7.2 Introduction

MPW is a solid state impact welding technology that is similar to explosive welding. By using the repulsion force between two opposite electromagnetic field, one piece of metal (the flyer plate) is accelerated onto another stationary piece (the target plate) with a high velocity. The velocities attained during this process range from 200 to 500 m/s [29, 109, 138]. The joining occurs on impact of the plates within the order of a microsecond [29, 158]. The proposed joining mechanism is related to the jet effect. During the impact process, the surface oxide is disrupted due to the jet action and metallurgical bonding is achieved between clean surfaces. Compared to traditional fusion welding technology, MPW can be applied to join dissimilar materials and there is no HAZ zone [149]. This welding is a dynamic loading impact process which brings in large deformation. It is also characterized as a rapid process and applicable for high productivity and automation manufacturing. However, the effective use of MPW technology is critically dependent on the ability to characterize not only the weldment properties but also the joining mechanism, the high strain rate deformation, and the microstructure of the interface. Therefore, a systematic microstructure characterization was performed on the welded interface. In this study, the microstructure of the interface has been characterized by multiple techniques, including OM, SEM, TEM, and Atom Probe Tomography (3DAP). The chemistry accuracy and high spatial resolution were achieved and a robust understanding of the interfacial structure and chemical intermixing were developed.

7.3 Experimental procedure

As shown in Table 7.1, aluminum alloy (AA) 6061-T6 plate and a copper alloy 101 (Cu 99.99%) plate with 0.50 mm thickness were prepared for MPW processing. The electrical resistance for Cu101 is 1.71×10^{-8} $\Omega \cdot m$ and for AA6061-T6 is 3.99×10^{-8} $\Omega \cdot m$. Therefore, Cu101 plate, with lower electrical resistance, was chosen as the flyer plate; and the AA6061-T6 plate was the target plate. The discharge energy of the capacitor bank is 7.2kJ. Taking the efficiency into account, about 10% of the discharge energy was converting into the welding process. The maximum induced current of 250 kA was measured and the duration was 12 μs. The nominal strain rate was in the range of $10^7 s^{-1}$. The zone of the welded interface was approximately 10 mm. The cross section of the welded zone was investigated by microhardness test and a combination of OM, SEM, TEM and 3DAP. The load for the microhardness was 10 g and the waiting time was 10 s. OM and SEM samples were prepared through the standard metallographic grinding and polishing techniques. Both the TEM samples and 3DAP samples were prepared by a focused ion-beam (FIB) lift-out technique. The resulted 160- μm-thick foil was examined in a TEM operated with an acceleration voltage of 200kV. The atom probe data were obtained with a Local Electrode Atom Probe (LEAP) operated at a voltage pulse repetition rate of 200 kHz and a pulse ratio of 0.2. Atom probe data analysis was performed with PoSAP software.

Table 7.1 Composition of AA6061-T6

AA6061								
Mg	Si	Cu	Fe	Cr	Mn	Zn	Ti	Al
0.8-1.2	0.4-0.8	0.15-0.4	<0.7	0.04-0.35	<0.15	<0.25	<0.15	Bal.

7.4 Results and discussion

7.4.1   Interface Microhardness

A cross-section of welded interface is shown in Figure 7.1. The SEM images indicate that the fully welded region was in wave pattern and consisted of valleys and peaks. A few isolated particles indicating possible intermetallic phase formation were observed near the vortices of this wave structure. A series of microhardness tests were performed across the interface and the average value for the hardness test as shown in Figure 7.2, indicated that the interface hardness was greater than the base metals.
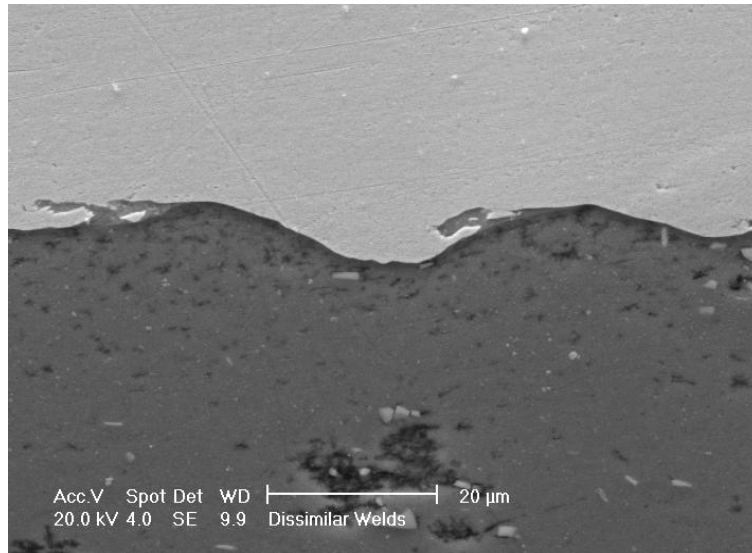
Figure 7.1 MPW Cu-Al joint. The top layer is Cu101 and bottom layer is AA6061.Intermetallic phase was formed along the wave interface.
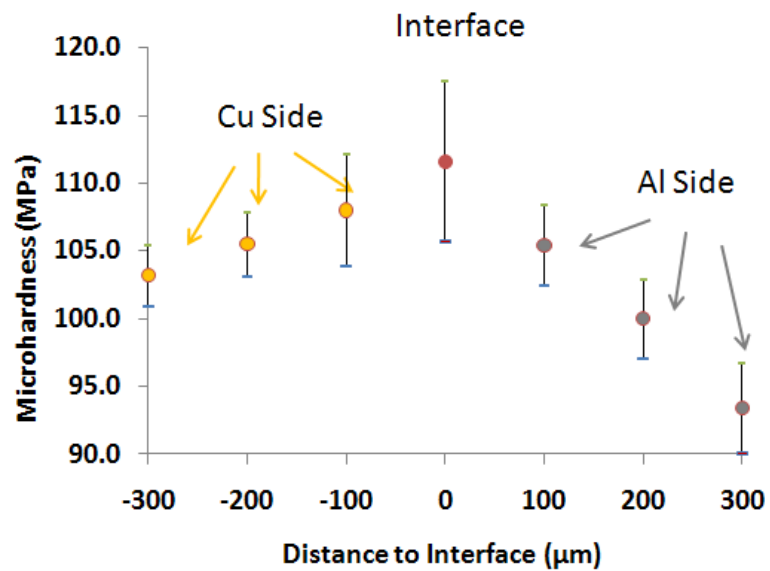
Figure 7.2 Microhardness test across the interface.

7.4.2 Heterogeneous Interface Structure

The welded Cu-Al interface showed wave pattern and the wave length and wave amplitude were within the range of $10\,\mu m$ and $100\,\mu m$ as presented in Figure 7.1. The interface suggested solid state bonding over the entire welded interface and small amount of intermetallic phase was observed on the wave corner. The intermetallic phase was isolated and did not form continuous layer. FIB was used to prepare ~100nm thick foil for TEM observation. And the images from secondary electron beam and gallium ion beam were shown in Figure 7.3. It suggested that the welded interface morphology was highly heterogeneous and it varied with the locations. All the three foils from different locations showed different image contrast along the interface comparing to the base metals. These contrast differences suggested composition changes, which might result from mechanical alloying or local melting. Some of the foils also clearly exhibited the plastic deformation induced shear band structure on copper side.
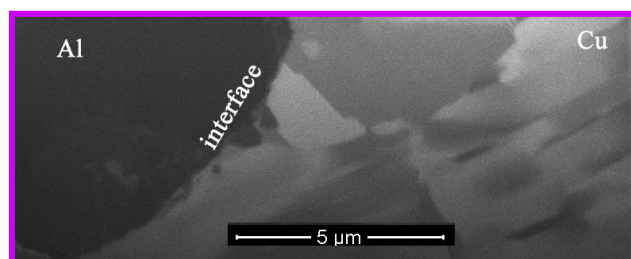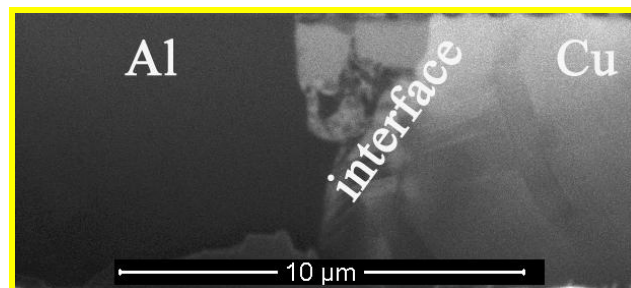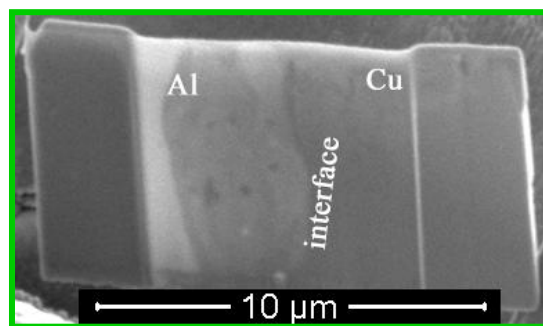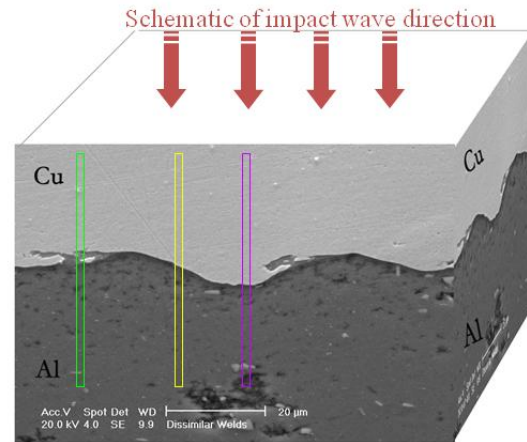
Figure 7.3 Heterogeneous interface structures from different location observed from FIB.

The foil thickness is about 150~200nm.

7.4.3 Grain Structure Along Welded Interface
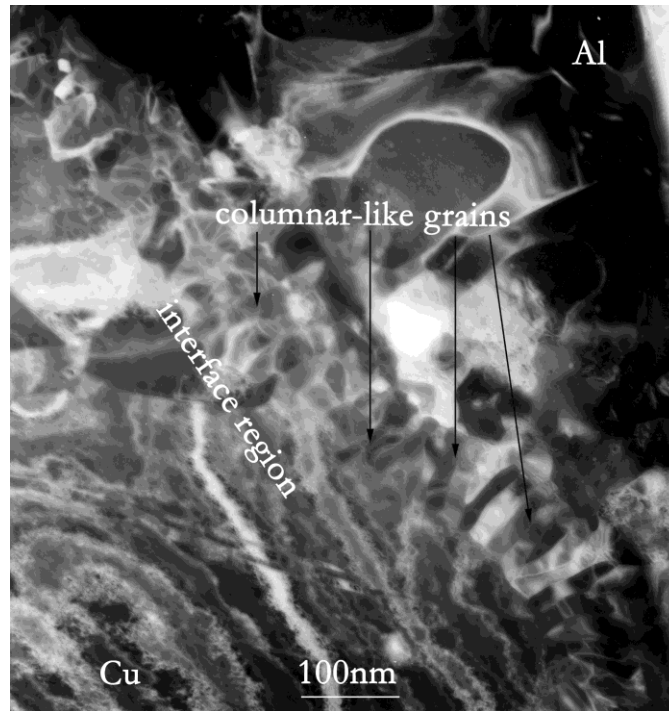
Figure 7.4 TEM BF image of the Cu-Al welded interface.

Bright field TEM image in Figure 7.4 was the overall observation revealed that the foil of the welded interface appeared various microstructure features. The Cu101 side mainly indicates the elongate grains and the AA6061 side presented intensive dislocations. Adjacent to the interface, the grains were extremely refined into submicron and nano-scales. According to the Hall-Petch relation, $\sigma \propto d^{-\frac{1}{2}}$, grain refinement was one of the reasons for higher interface hardness. As shown in Figure 7.5, some of the interfacial

grains were teeth-like grains and their diffraction pattern index indicated that the grain misorientation angle was both large and small. And the axis angle results between each grain were shown in Table 7.2. These grains formed interlock between each other. The grain refinement, deformation twins, and dislocation density were all accommodating to the high strain rate deformation.

Table 7.2 Axis angle between teeth-like grains

Pair	Rotation Axis	Rotation Angle	Σ
G1 and G2	001	36.9	5
G2 and G3	100	22.6	13a
G3 and G4	210	48.2	15
G4 and G5	111	60.0	3
G5 and G6	100	36.9	5
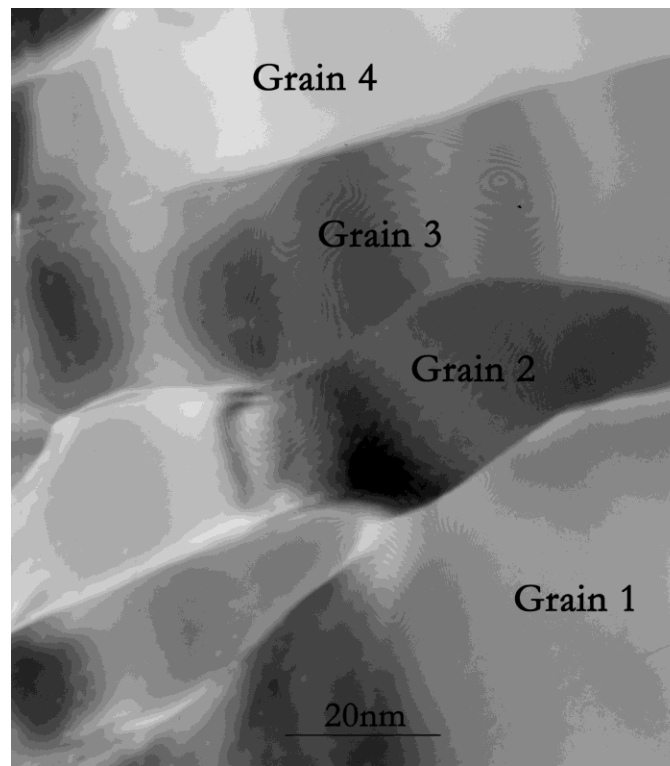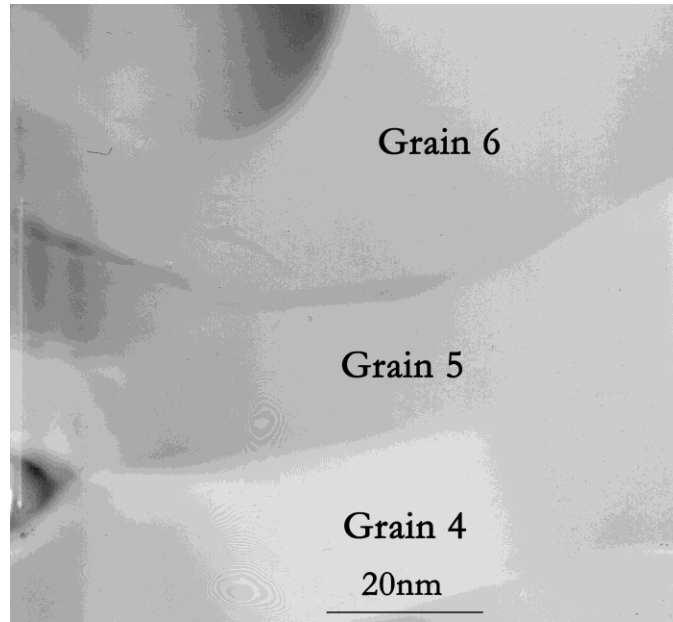
Figure 7.5 Teeth-like grains along the welded interface.

7.4.4 Short Distance Diffusion Observed by 3DAP

The needle shaped specimen was prepared from the welded interface and the diameter of the needle tip was about few nanometers (~10nm). The needle specimen included three phases: Cu101, welded interface intermetallics (IM) and AA6061 from the specimen tip to bottom as shown in Figure 7.6. And thus there were two interfaces, Cu/IM and IM/Al on the needle specimen.
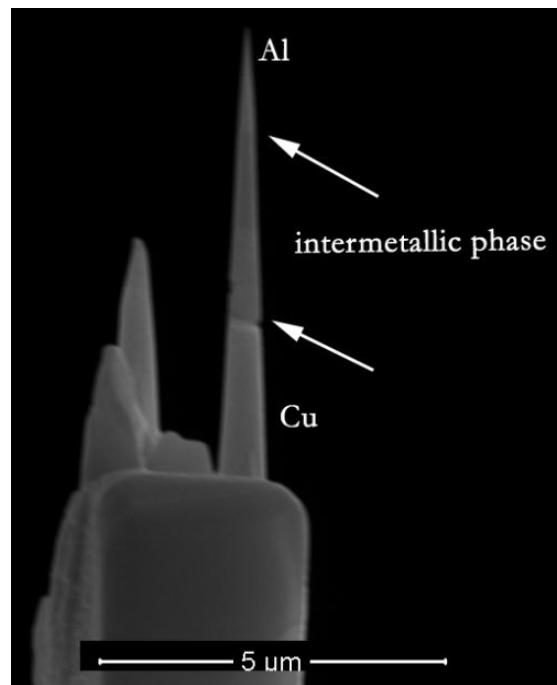
Figure 7. 6 Needle shaped sample for APFIM. The arrows indicate the boundary between the aluminum and mixture, and the boundary between mixture and copper.

The collected atom position history files were reconstructed into 3D cylinder structure and the special atoms distribution was plotted into Figure 7.7. It showed that the aluminum atoms were confined in half of the cylinder with a very sharp interface, while the copper atoms fulfilled the cylinder uniformly. The composition profile for aluminum atoms and copper atoms as shown in Figure 7.8 was obtained from the welded interface. It showed that there might be 10nm wide intermetallic phase formed along the interface and the nominal compounds were close to Al_4Cu_{15}. Therefore, short distance diffusion could occur. However, further study is needed to determine if the mixture is intermetallic phase or not. The diffusivity (D) of FCC metal surface was found to be $10^{-12} \sim 10^{-9} m^2 s^{-1}$ [159] when the temperature is less than melting temperature. The completed MPW process duration (t) lasts roughly for 10^{-7}s. As a result, the distance that aluminum can diffuse in copper within that time, given by $\sqrt{Dt}$, was in the range of 0.1~10nm. The observation from 3DAP results was in a good agreement with the 10nm short distance diffusion. Therefore, the intermetallic phase formation approved that the mating interface temperature was close to the melting point. Additionally, since the morphology of the atoms was uniform, this intermetallic phase formed from solidification process, which also indicated possible local melting and short distance diffusion occurred in the interface.
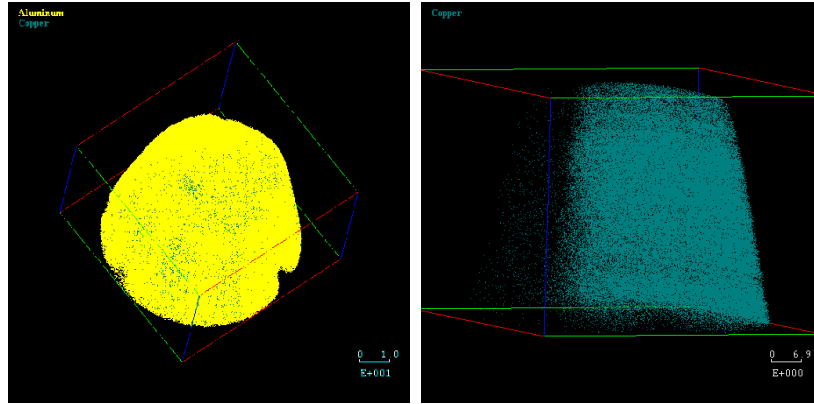
Figure 7.7 3DAP reconstruction for the needle shaped sample from Cu-Al welded interface.
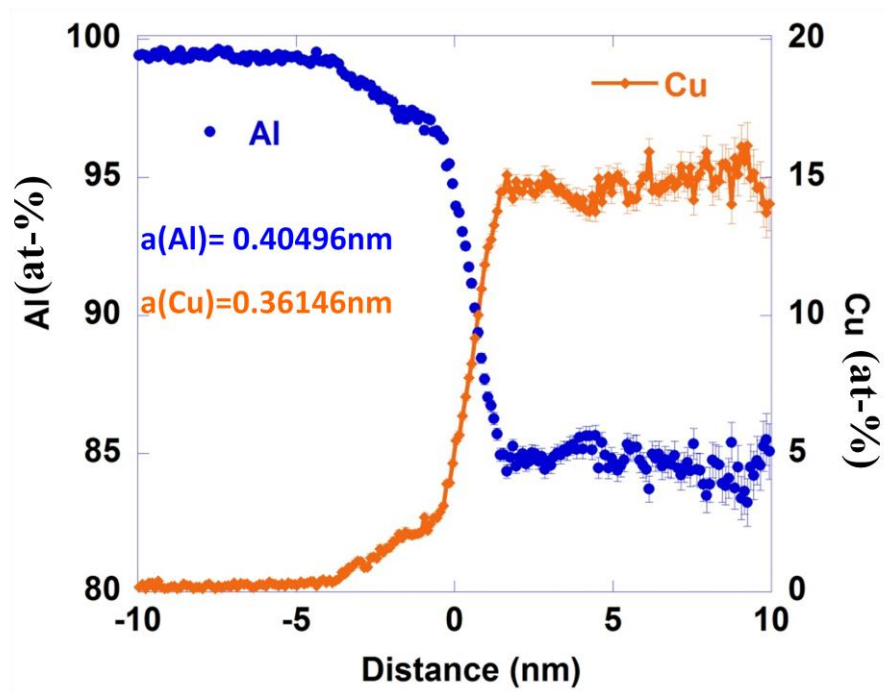
Figure 7.8 Composition profile for aluminum and copper atoms. The zero distance was defined as the boundary between aluminum and mixture.

7.5 Conclusion

MPW can be used on dissimilar materials welding. The welded interface has higher microhardness. Combination of the observation from OM, SEM, TEM and 3DAP, the interface microstructure was investigated. It shows wave morphology with discontinuous pockets of few intermetallic phases, Al_4Cu_{15}. It is also noticed that the interface has various microstructure, such as the lamellar grains, submicron and nanocrystalline grains, and teeth-like grains. Therefore, the refined grain structure with large misorientation and intermetallic phase were considered to be the origin of high bonding strength for MPW joint. The composition profile and the 3D morphology with high spatial resolution might prove short distance diffusion and possible local melting occurred along the welded interface.

Chapter 8 Magnetic pulse welding on Al-Fe dissimilar materials

8.1 Abstract

Traditional fusion welding has difficulties to weld dissimilar materials but there is increasing demand for joining dissimilar materials, such as joining between aluminum alloy and steel. Recent research suggested that MPW can be applied onto dissimilar materials joining and this study investigated tubular joining and plate joining. The tubular joining was conducted between low carbon steel 1018 rod and aluminum alloy (AA) 6063-O tube. The plate lap joining was carried on AA 6061-T6 plate to low carbon steel 1008 plate. For both of them, aluminum alloy was the flyer and low carbon steel was the target. The study focused on a basic MPW process factor, the impact energy, which significantly affects the joint strength. The joint strength and microstructure from different impact energy levels were compared. Peeling test and microhardness test were used to evaluate the joint strength. And the metallographic examinations were conducted on OM, SEM, and EDS. It was found that both the welded interface morphology and the joint strength were relative to the impact energy level. With increasing impact energy, the joint strength increased and the welded interface changed from flat feature to wave

pattern. Low impact energy induced grain refinement in a narrow zone without any intermetallic phases, while high impact energy introduced grain refinement in a relatively wide zone with certain amount of intermetallic compound. The intermetallic phase formation was also discussed.

8.2 Introduction

Taking the fuel efficiency improvement into consideration, the joining between aluminum alloy and steel has raising demand in lots of applications, such as the spacecraft, vehicle space frame, high vacuum chambers and even the cooking utensils. Both aluminum alloy and steel have different but favorable properties, namely, the high thermal conductivity and low density of aluminum alloy, and the high tensile strength, the good weldability and economics of steels [160, 161]. Therefore, the hybrid structures between aluminum alloy and steel are receiving more attention. However, there are few suitable methods for welding between steel and aluminum alloy. Fusion welding technologies of steel and aluminum alloy suffer from poor weldability and heavy cracking with brittle failure in service [162, 163]. It is because that aluminum alloy and steel have large difference between their melting points (933K for Al and 1811K for Fe), and nearly zero solid solubility of iron in aluminum. Therefore, they are prone to form brittle intermetallic compounds such as Fe_2Al_5 and $FeAl_3$ [164, 165]. Additionally, the differences in thermal properties such as expansion coefficients, conductivities, and

specific heats lead to internal stresses after fusion welding. As solid state welding techniques has proven to practically eliminate the formation of intermetallic phases, it could be an effective alternative to weld dissimilar materials [137, 139, 161, 162, 166-169].

MPW is one of the solid state impact welding techniques. It is a rapid welding process (less than 50 μs) and no HAZ is generated. Therefore, the distortion and weakening problems are eliminated. Additionally, the tooling cost is relative low and the welding design is flexible [9, 13, 18, 165]. Since late 1960's, there has been lots of research works on MPW of axi-symmetric workpieces, such as tubular welding [8, 18, 139, 170]. But these work focused mainly on the similar material welding with energy up to several hundreds of kilojoules. Masumoto et al. (1985), Hokari et al.(1998) and Aizawa et al.(2007) have proven that MPW is a useful method for aluminum/steel joining [8, 9, 139]. However, most of the previous work proposed the concept of MPW, and less research work has been stressed on the process parameter effect. In order to expand the application of this impact welding technology widely, it is required to understand the process parameter effect on the weld properties. This chapter specifically studied the impact energy effect on the welding of AA6063-O tube to low carbon steel 1018 rod and AA6061-T6 plate to low carbon steel 1008 plate.
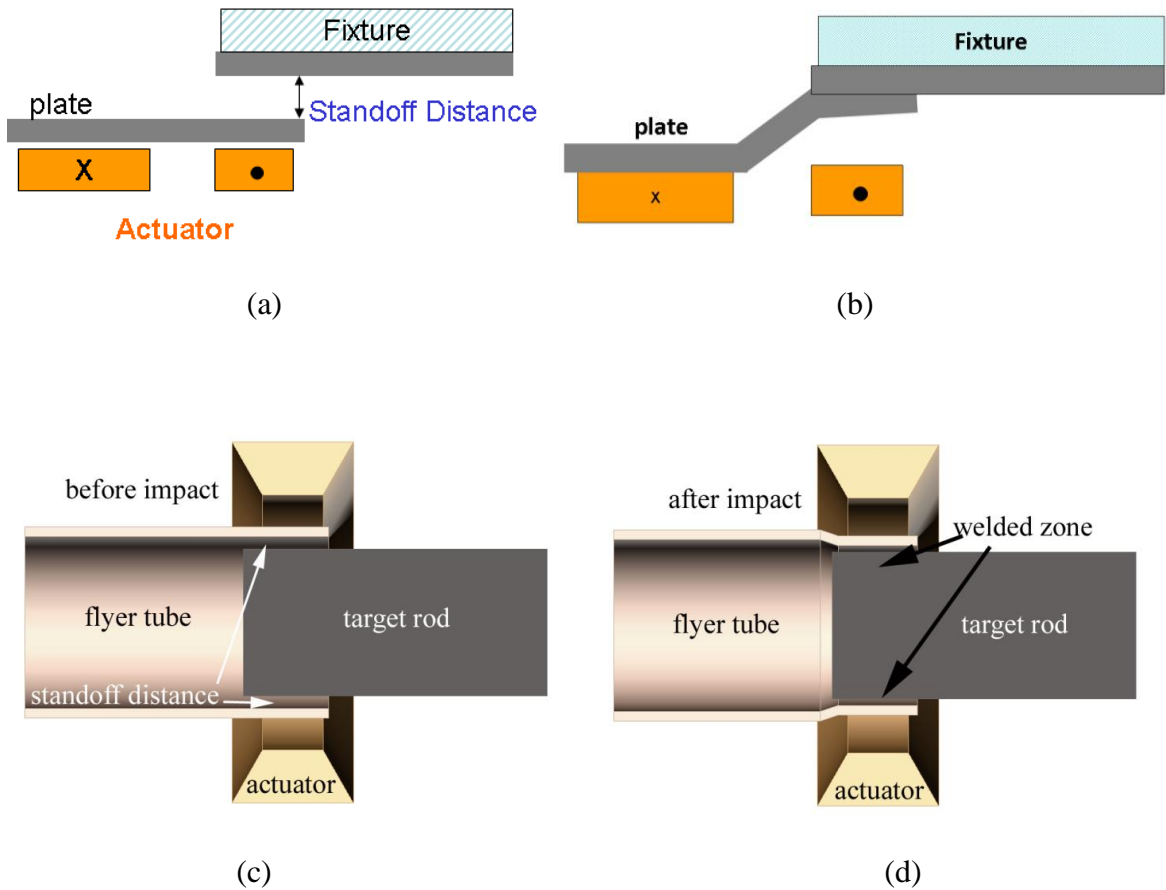
Figure 8.1 (a) Cross section image of plate welding before impact, (b) Cross section image of plate welding after impact, (c) Cross section image of the tubular welding before impact, (d) Cross section image of the tubular welding after impact.

MPW uses electromagnetic force to accelerate the workpiece for impact welding and the system mainly includes the power supply, the capacitor bank, the actuator, and being welded workpieces. During welding process, the stored electric energy in the capacitor bank is discharged into the actuator. The discharging current through the actuator is the

primary current and it induces the secondary current flowing parallel but in the opposite direction in the nearby metal workpiece. Consequently, both the primary and the secondary current generate magnetic fields. Due to the opposite phases of the resulting magnetic fields, the flyer tube receives a repulsive force and collides against the target rod at 200m/s~500m/s collision velocity [131, 171]. Figure 8.1 present the cross section of the actuator and the workpieces. Before impact, there is about millimeter standoff distance between flyer and target. After impact the flyer collides onto the target and forms metallurgical bonding.

During impact process, the oxide layer on the metal workpieces surface was removed by jetting from the high speed collision [139]. Meanwhile the huge magnetic pressure held the two clean metal surfaces together to form the metallurgical bonding between the flyer tube and the target rod. It is also interested to point out that impact welding could be obtained only with certain optimum impact angles.

8.3 Experimental procedure

8.3.1   Materials Selection

Aluminum alloy was used as the flyer and low carbon steel was used as the target for the experiment. The nominal composition for both flyer and target materials were tabulated

into Table 8.1. The outer diameter for AA6063-O tube is 25.40mm and the wall thickness is 1.905mm. The axial length is of 50.80mm. The diameter for 1018 steel rod is 17.145mm and the length is 38.10mm. Both the AA6061 and low carbon steel 1008 plates were in the same size, and the width is 76.2mm, the length is 101.6mm. The plate thickness was 0.254mm.

Table 8.1 Chemical composition of welded materials (wt%)

Tubular welding

AA 6063-O (flyer)

Mg	Si	Cu	Fe	Cr	Mn	Zn	Ti	Al
0.45-0.9	0.2-0.6	<0.1	<0.35	<0.1	<0.1	<0.1	<0.1	Bal.

AISI 1018 (target)

C	Mn	P	S	Fe
0.14-0.20	0.60-0.90	<0.04	<0.05	Bal.

Plate welding

AA6061-T6 (flyer)

Mg	Si	Cu	Fe	Cr	Mn	Zn	Ti	Al
0.8-1.2	0.4-0.8	0.15-0.4	<0.7	0.04-0.35	<0.15	<0.25	<0.15	Bal.

AISI 1008 (target)

C	Mn	P	S	Fe
0.10	0.3-0.6	0.04	0.05	Bal.

8.3.2 Study on Process Parameters

The impact energy level for tubular welding varied at 7.7kJ, 11.2kJ and 14.9kJ. And this welding was conducted on tubular actuator. The plate to plate welding used flat bar actuator with 5 ºinitial launch angle. And the impact energy levels were 5.6kJ, 6.4kJ, and 7.2kJ. The standoff distances for tubular welding and plate welding were 2.22mm and 3.15mm respectively.

8.3.3   Mechanical Test and Microstructure Characterization

The joint strength was studied by peeling test and microhardness test. The plate joints were sliced into 10mm wide sample for peeling test. The force applied on the sample was recorded with regard to the displacement. And the joint strength was interpreted as the force on unit welded length (F/L). Microhardness test was conducted on the cross sections of the tubular welded samples. It was measured across the welded interface using the Vickers method with a 10g load and 10s dwell time. The measured data was plotted as two dimensional microhardness maps. OM, SEM and EBSD were used to investigate the microstructures of the welded interface and the surrounding area. For microstructure study, the cross sections of welded samples were prepared by standard metallurgical polish techniques. And the final procedure ended by polishing on 1 μm diamond paste. To identify the composition changes and the intermetallic phase on the welded interface, linear scan from the EDS was carried out on the polished cross sections.

8.4 Results and discussion

8.4.1   Peeling Strength and Joint Hardness

The joint strength measured by peeling test indicated that it increases with the increasing of impact energy as shown in Figure 8.2. The peeling experiment was repeated on several samples and the results were quite consistent. The overall load to pull the jointed two plates apart was only about hundred Newtons, which indicate the plate to plate Al-Fe joint was weak.
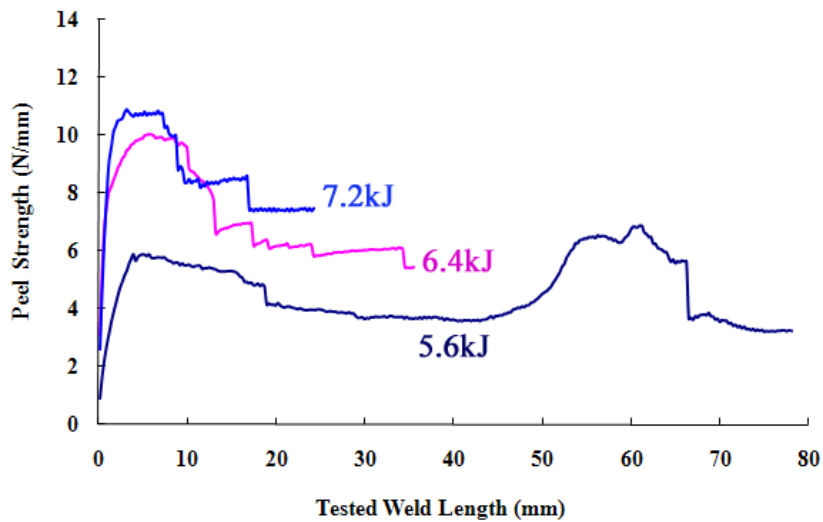
Figure 8.2 Peeling strength of the Al-Fe joint by three different impact energy levels.

The cross sections from the tubular welded samples at different impact energy levels were shown in Figure 8.3. The images were taken from the same location near the middle of the welded length. All welded interface showed wave structure. The wave length and wave amplitude increased with the impact energy increasing. Low impact energy resulted in relatively flat surface while high impact energy resulted in rough wave surface. The wave feature was generated by high velocity impact. Different from quasi-statistic state, under high strain rate deformation, the welding interface materials approaches plastic formation at lower stress level than the nominal yield stress. And thus they were readily pressed into each other and formed the interlocking wave pattern. It was also observed that intermetallic phase existed on the medium and high impact energy welded interface and they showed different contrast.
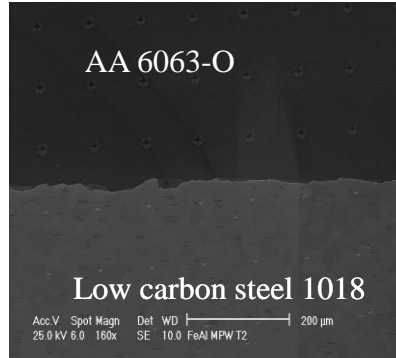
(a)
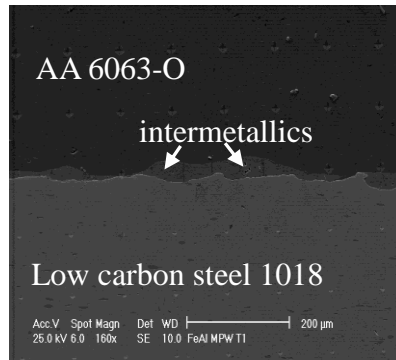
(b)
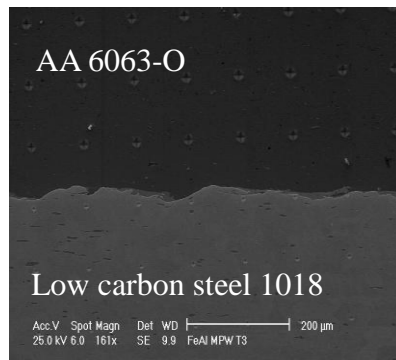
(c)

Figure 8.3 SEM images on Al-Fe interface for three impact energy levels. (a) low impact

energy (b) medium impact energy (c) high impact energy

The indenters on SEM images were used to measure microhardness and the hardness maps were shown in Figure 8.4. The hardness map was generated from an array of the tested microhardness value and the spacing between each indenter was 30 μm. From the surrounding area to the interface, hardening was observed on both low carbon steel side and aluminum side. But the increase in the hardness was found to be more along the interface. For example, the hardness value of the base aluminum alloy was almost constant at about 50Hv, while the hardness of aluminum alloy near to the interface could be up to 100Hv. The steel base metal had microhardness about 180Hv, and the interface hardness was up to about 270Hv.

(a)Low impact energy   (b) Medium impact energy   (c)High impact energy
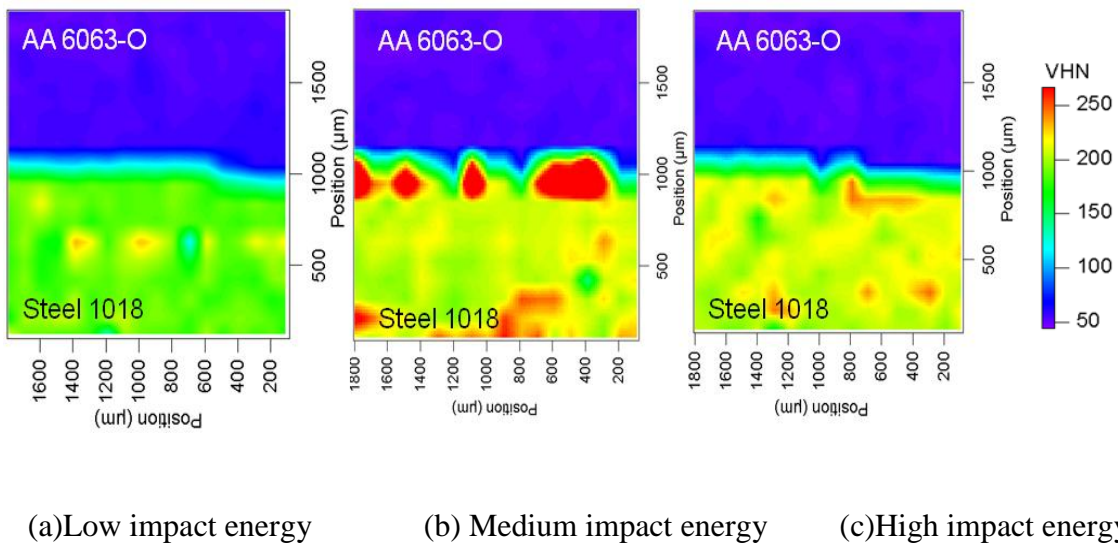
Figure 8.4 Microhardness map for welded Al-Fe pairs at different energy levels.

Microhardness maps also exhibited the wave pattern and it suggested that the medium impact energy has largest microhardness along the interface. This abnormal hardness increasing was related to the interface intermetallic phases as shown in Figure 8.3(b). Overall, it was believed large amount of hardness increase was due to the heavy plastic, the high strain rate hardening, and the intermetallic phase formation.

8.4.2   Interface Grain Refinement

The ultra-fine grain structure and the elongated grains adjacent to the interface were observed by EBSD as shown in Figure 8.5 and 8.6. The grain structure from all of the three impact energy levels had the same trend as shown in Figure 8.5. Coarse grains were found in the base metal away from the interface. The low carbon steel base metal was in BCC structure and indexed as iron alpha phase, and the grain size was about $20\,\mu m$; and aluminum alloy was in FCC structure and the grain size was about $80\,\mu m$. However, in the interface region, the grains were extremely refined and the size was less than $5\,\mu m$. The refined grains also presented large misorientation as shown in Figure 8.6. The grains in base metal had misorientation angle in range of 0 to 15 degree, whereas the misorientation angle for interfacial grains fell into the range of 30 to 45 degree. Further TEM study is needed to analysis the composition of each individual grains. Table 8.2 was the summary of the measured grain size and misorientation from the three different impact energy levels. The experiment data was in the agreement with Hall-Petch relation,

$\sigma_y \sim d^{-1/2}$, in which σ_y is the yield strength and d is the grain size, as the linear relationship shown in Figure 8.7.
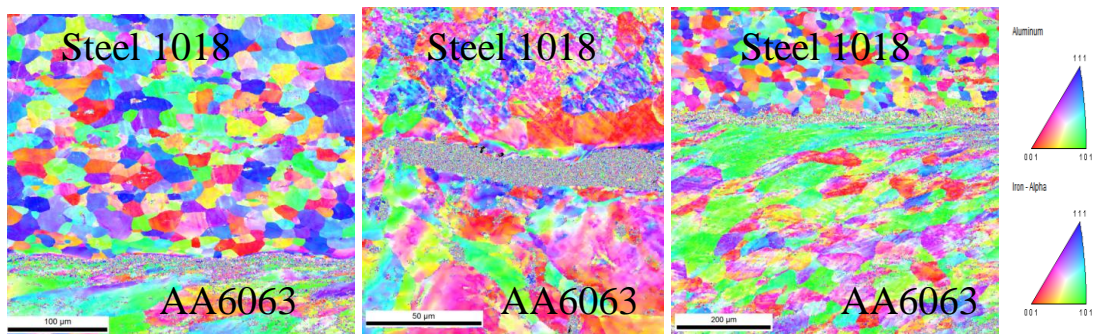
(a) Low impact energy   (b) medium impact energy (c) high impact energy (d) index key

Figure 8.5 Color code index for inversed pole figure from EBSD.
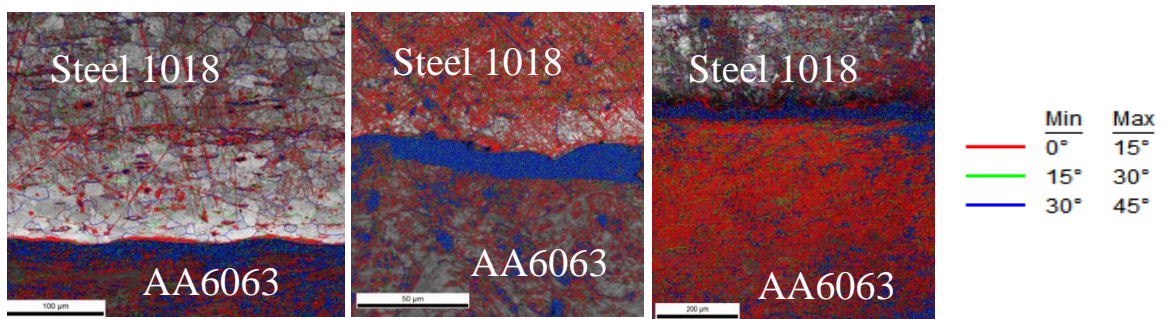
(a) Low impact energy   (b) medium impact energy   (c) high impact energy   (d) index boundary

Figure 8.6 Grain misorentitaion angle index from EBSD

Table 8.2 Grain size and misorientation at the welded interface from different impact energy level

Impact Energy (kJ)	Misorientation Angle (degree)	Average Grain Size d (μm)	(Grain Size) $^{-1/2}$ ($d^{-1/2}$)	Maximum Microhardness (Hv)
Base Metal AA 6063-O	5.28	80	0.11	50
Base Metal steel 1018	6.73	20	0.22	180
7.7	40	3.98	0.50	120
11.2	45	0.8	1.12	250
14.9	45	3.7	0.52	180
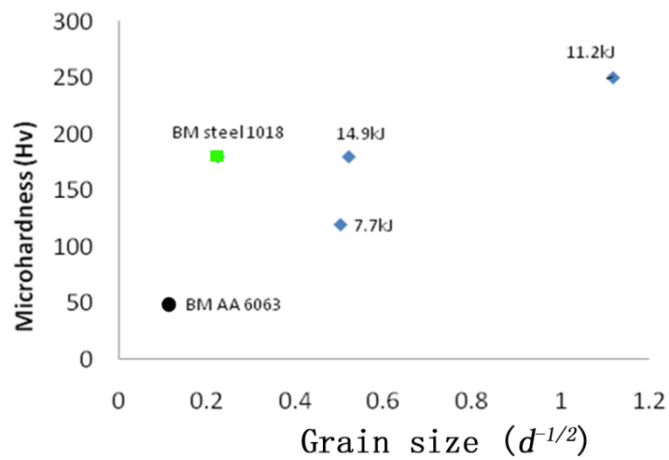
Figure 8.7 Relationship between grain size and microhardness from MPW joints

Figure 8.7 also indicated that the aluminum grains along the interface presented the elongation in the impact direction, while steel grains did not show obvious elongation. This phenomenon was related to the high stain rate impact and the following dynamic recrystalization. Both the steel grains and aluminum alloy grains suggested the effect of the high strain rate impact, which broke the coarse grains with low grain boundary misorientation into fine grains with high grain misorientation. And the following dynamic recrystalization of the heavily deformed grains also attributed to the grain refinement. It is known that the grain recrystalization is related to the temperature relative to the melting point of the materials. The grain elongation of low carbon steel was expected to be smaller than that of aluminum alloy because steel has higher melting point than aluminum alloy. The similar phenomenon was reported from friction stir welding as well [168].

Besides the corner intermetallic phase formed along the wave pattern, the grain refinement along the welded interface was also observed by EBSD, which was attributed to the increase of the peeling strength and the microhardness.

8.4.3   Intermetallic Phase Formation

Discontinuous intermetallic phase was found along the welded interface as shown in

Figure 8.3, which also offered higher microhardness. But the intermetallic phase distribution from MPW interface was different from traditional fusion welding process, in which the continuous intermetallic layer was formed. However, in MPW, the intermeatllic phase was only found at the corner of the wave pattern and it did not disperse along the interface or form any continuous layers. In order to study the composition of the intermetallic phase, linear EDS scan was conducted and the results were shown in Figure 8.8-8.10. At low impact energy level, there was no intermetallic phase along the welded interface, which was proved by the composition profiles in Figure 8.8(b-e) from four different locations as shown in Figure 8.8(a). The composition changes in traces of Mg, Al and Fe (wt %) only showed one sharp step crossing the interface and there was no other phases along the detected lines.

There was intermetallic phase along the medium and high impact energy welded interface, but they were not continuous. For the pure solid state bonding region, the composition profile had only one sharp step. For the intermetallic phase region, the composition changed with platform once crossing the interface. The composition profile in Figure 8.9 (c) and (e) presented that Al-rich phase was formed at the medium impact energy level and Al composition was about 70wt%. Figure 8.10 (c) and (d) from the high impact energy also indicated Al-rich phase with 70wt% Al concentration. This composition was a mixture of compounds and close to Al_9Fe_2, an aluminum-rich metastable phase. It was reported that Al-rich intermetallic compounds are hard and brittle with almost null compressive strain at 200MPa [163]. Therefore, the large amount of Al-rich intermetallic

phase should be avoided and the impact energy should be selected within a suitable range. The intermetallic phase formed at MPW process was believed from the solid state reaction. Namely, they were formed from the supersaturated solid solution due to mechanical alloying rather than from melting and solidification. However, further TEM study for the structure of the mixture phase can help to reveal is the mixture are crystalline structure of amorphous structure. One possible reason is that the entire welding process usually completes less than $50\,\mu s$, and no interdiffusion of the elements could occur within such short reaction time. Also on the collision point, the metal surface was pulled by the jetting effect and then some of them scattered into the corner of the just-formed wave interface under huge magnetic pressure. There was no melting occurred during the impact welding of Al-Fe, which could also be verified by the intermetallic phase morphology. Because there is no petal or needle shaped precipitations, which are the most typical morphology of the intermetallic phase from melting [162].

(a) EDS line scan positions for 7.7kJ

(b) composition profile from line 1

(c) composition profile from line 2

(d) composition profile from line 3

(e) composition profile from line 4
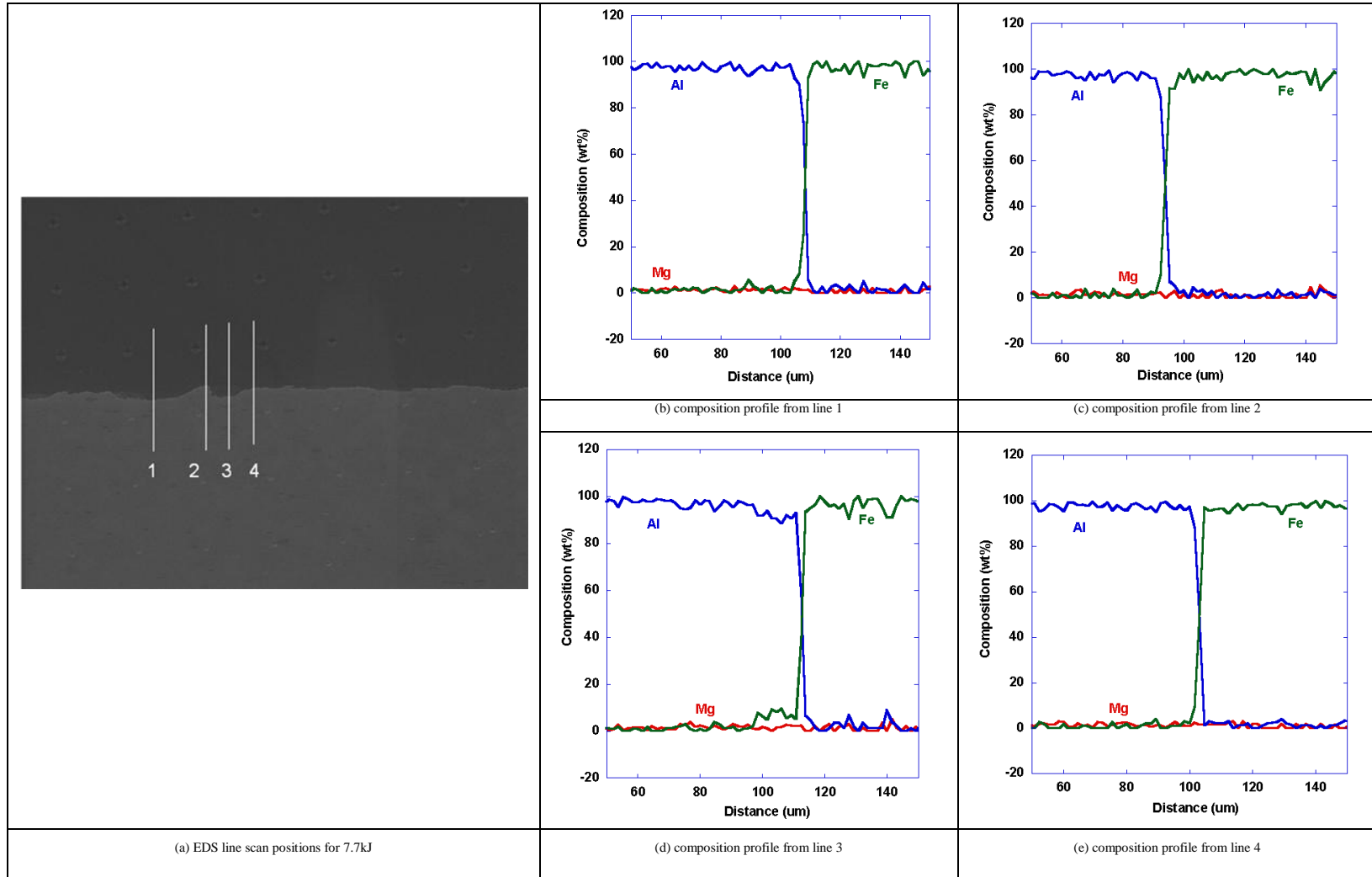
Figure 8.8 EDS chemical composition analysis on low impact energy (7.7kJ) welded Al-Fe interface.

(a) EDS line scan positions for 11.2kJ

(b) composition profile from line 1

(c) composition profile from line 2

(d) composition profile from line 3

(e) composition profile from line 4
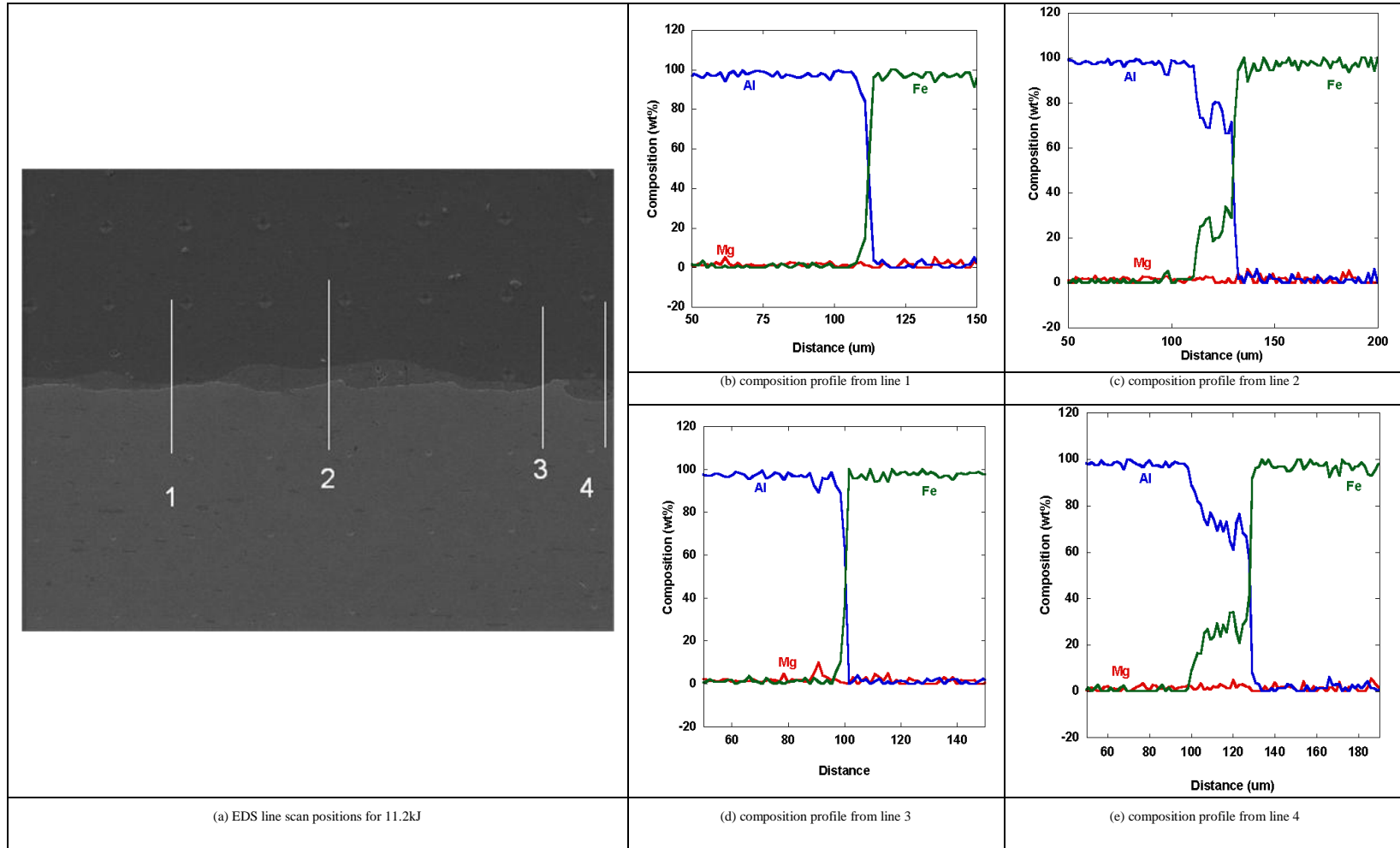
Figure 8.9 EDS chemical composition analysis on medium impact energy (11.2kJ) welded Al-Fe interface.
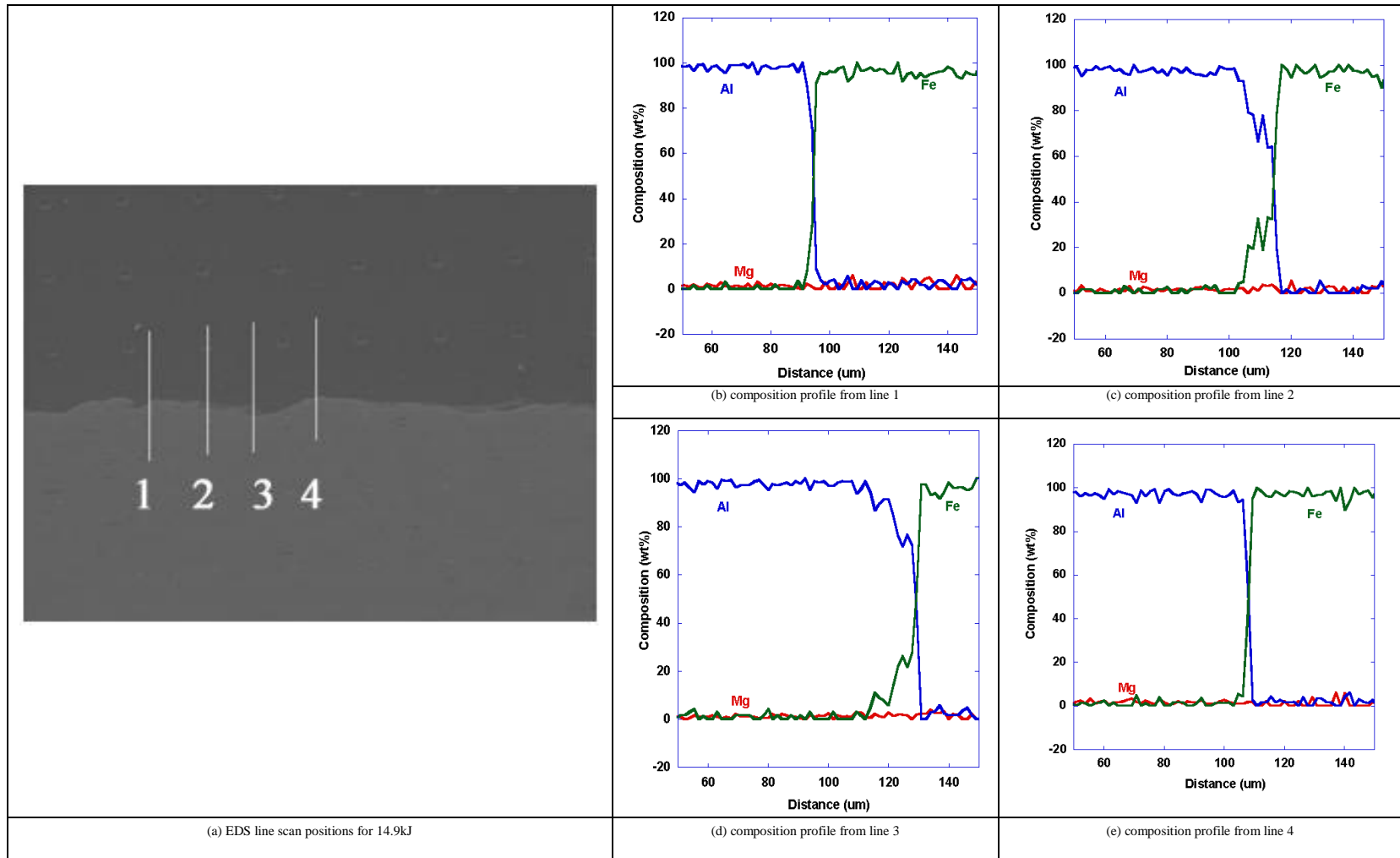
Figure 8.10 EDS chemical composition analysis on high impact energy (14.9kJ) welded Al-Fe interface.

In summary, impact energy level significantly influenced the joint strength, the microhardness and the welded interfacial microstructure. Metallographical and microanalytical studies of the welded interface from three different impact energy levels indicated that increasing the impact energy level assisted the improvement of the joint strength and hardness. Usually, MPW joints had greater hardness value comparing to the base metal. The mechanical property changes were related to both the intermetallic phase formation and the refined grain structure. The intermetallic phase did not exist on the low impact energy welded interface but existed at the corner of the wave pattern from the medium and high impact energy welds.

8.5 Conclusion

This study investigated that the dissimilar metal joining of aluminum alloy 6063-O tube to low carbon steel 1018 rod with a sound heterogeneous welding microstructure was feasible by MPW. During the welding process, AA6063-O tube was the flyer and steel 1018 rod was the target. One process parameter, the impact energy level, was studied. It was found that all of the welded interfaces showed wave pattern and the interface strengths were related to the impact energy level. High impact energy resulted in greater strength due to the extremely refined interfacial grains. The wave amplitude and wave length increased with the impact energy level. However, exceeded impact energy could lead to large amount of intermetallic phase which embrittled the joint.

Chapter 9 Finite element analysis for magnetic pulse welding

9.1 Abstract

During MPW, the well focused and controlled electromagnetic energy leads to high velocity impact and true metallic bonding between two workpieces. This microsecond duration process is also associated with high strain rate deformation and Joule heating. Up to date, only the primary current, secondary current and impact velocity can be instrumentally measured with high temporal resolution, whereas the transient mechanical property and thermal property of the materials are hard to capture during welding process. Therefore, finite element based software, LS-DYNA®, was introduced for MPW at a macroscale. It can couple mechanical, thermal, and electromagnetic simulation within in one single simulation. This computational simulation not only helps to investigate the optimal welding conditions but also helps to develop the welding system with high efficiency.

This chapter intruded the preliminary work on plate to plate MPW of AA6061 and Cu101. The obtained impact velocity form computational simulation was compared to the

experimental measurement to verify the buildup models. After verification, such model was used to predict the strain, strain rate and temperature changes along the welded interface and also to investigate the successful welding criterion with regard to the impact angle and impact velocity.

9.2 Introduction

The new developed electromagnetism (EM) module introduced in LS-DYNA allows simulating the complex electromagnetic forming process accurately and efficiently [175-178], because LS-DYNA can solve the electromagnetic, thermal, and mechanical problem coherently. Conventional FEA approaches solve the electromagnetic and mechanical analysis separately. And the user subroutine was used to extract the EM modeling results and transfer to mechanical analysis. And therefore, the numerical simulation for EM forming process is not accurate and reliable [132, 179]. Lots of effort is needed to clarify the appropriate assumptions and verify the results. For example P. Zhang [132, 179] used electrodynamics code to calculate the magnetic repelling force and then transferred the force to a solid dynamics code to calculate the plastic strain. And the codes were only modified from the experimentally measured strain, which could bring in errors. LS-DYNA is a tight coupling approach, and the deformation of the workpiece was setup as a function of the EM field. The solution of continuum solid mechanics equations were coupled with Maxwell's equations and then it is able to

directly link the electromagnetic pressure into the mechanical and thermal modules. The measured primary current was imposed into the simulation as the input file, and equation of state (EOS) includes the electromagnetism with regard to the electrical conductivity, the current density and the temperature changes.

For mechanical analysis, there are several constitutive analytical functions for metals at high rate forming process, as such the Johnson-Cook models [20], Zerilli-Armstrong model [180], and Steinberg models [181]. All of these models offer the analytical function of strain which is dependent on the materials constitutive properties. Johnson-Cook model (as shown in Equation (9.1)) was used for MPW simulation and the materials parameters were listed in Table 9.1.

$$\sigma(\varepsilon, \dot{\varepsilon}, T) = (\sigma_0 + B\varepsilon^n)(1 + C\ln\frac{\dot{\varepsilon}}{\dot{\varepsilon}_0})(1 - T^{*m}) \text{ with } T^* = \frac{T - T_r}{T_m - T_r} \text{ Equation (9.1)}$$

in which σ_0, B, C, m and n are materials properties. T_r is a reference temperature (at which σ_0 is measured) and $\dot{\varepsilon}_0$ is a reference strain rate (often equal to 1). T_m is the melting temperature.

Table 9.1 Materials parameter for Johnson-Cook model for AA6061 [27]

J-C parameter	σ_0 (MPa)	B(MPa)	C	m	n
Literature value	60	500	0.02	1	0.3

The goal of this simulation work is to establish an accurate model for MPW. Before FEA analysis, a three dimensional geometry file is developed comparable to the real sample size. The geometry file is then meshed into certain a mount of elements. Finer mesh offers higher resolution but needs more computer time. The meshed geometry file with coordinate for each individual node is used as part of the input file for simulation work. The other input files include the primary current, the strain stress relationship at high strain rate, and the materials properties. Since MPW involves adiabatic heating, and the variation of the stress with temperature should also be considered. The magnetic field and electric field in conductors (actuator, flyer plate and target plate) are solved by Finite Element Method (FEM) and in insulators (air and insulating tapes) are solved by Boundary Element Method (BEM). BEM makes it much easier to catch the flyer plate motion. It is necessary to point that the FEM plus BEM approach takes long matrices assembly time and require big memory.

This chapter attempts to provide the basis for a FEA-based approach. The oblique MPW impact of AA6061-T6 and Cu101 sheets were analyzed using the newly available Electromagnetism (EM) module in LS-DYNA. This module allows coupling between mechanical, thermal, and electromagnetic calculation. The simulation can predict impact condition and thermal cycling on the mating interface. The computational results were validated with instrumentally measurement from PDV.

9.3 Simulation principles

9.3.1 Pre-post of Simulation

The secondary generation of flat bar actuator was applied for the simulation process and 5 °initial launch angle was chosen. The model as shown in Figure 9.1 includes three parts, and they are the actuator, flyer plate and target plate. All of the parts are meshed using solid hexahedral elements, with four elements through the thickness of the plate. The mesh on the actuator was refined near the chamfered side, where determined the 5° initial launch angle. The target and the flyer plates were assembled adjacent to the actuator with 12.7mm overlap. The standoff distance between target and flyer was 3.15mm. This setup was plotted by commercial software (Solidworks®) and meshed into hexahedron element by Hypermesh®. The drawing and mesh procedures can also be conducted by LS-Prepost®. The number of the element is determined by the mesh size. The mesh near to

the welded region is recommended to be in finer size. After simulation, the results were visualized by LS-Prepost.
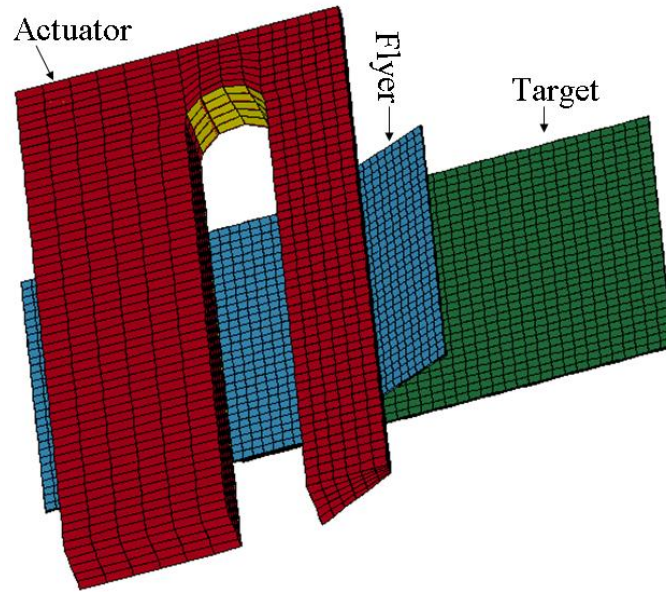
Figure 9.1 Meshed three-dimension model for MPW system. This is the view from bottom.

9.3.2 Materials Properties

The required mechanical, electromagnetic and thermal properties for simulation are shown in Table 9.2. All of these parameters are measured at quasistatic state. The strain stress relationship for high strain rate and J-C model parameters were cited from

literatures [112].

Table 9.2 Material Property of AA6061-T6 and Cu101[172]

Properties	Flyer Workpiece (AA6061-T6)	Target Workpiece (Cu101)
Electrical Conductivity (Ω mm)$^{-1}$	0.250627×10^5	0.584795×10^5
Mass Density (g/mm^3)	2.7×10^{-3}	8.94×10^{-3}
Young's Modulus (GPa)	68.9	115
Poisson Ratio	0.33	0.31
Yield Stress* (MPa)	276	195
Heat Capacity (J/g ^{o}C)	0.896	0.385
Thermal Conductivity (W/mK)	167	391
Melting Point (^{o}C)	582~651.7	1083

(*The yield stress is measured at the quasistatic state.)

9.3.3   Primary Current and Secondary Current

The primary current measured by Rogowski coil during MPW process was used as the input file for the simulation process. A typical current profile was shown in Figure 9.2. The current profile showed a damped sinusoidal waveform with regard to time which can be expressed as Equation (9.2):

$$I(t) = \frac{V_0 \sqrt{C/L_{sys}}}{\sqrt{1-\xi^2}} \exp(-\xi \omega t) \sin(\omega t)$$

Equation (9.2)

in which, *Vo* is the system voltage, ξ is the damping factor, *C* and L_{sys} is the system capacitor and inductance, and ω is the frequency.

The primary currents for different discharge energy have similar period but different magnitude. The higher discharge energy generated a larger induced current. The shape of the primary current depends on the properties of the actuator and the capacitor bank. The induced secondary current is mainly determined by the flyer plate properties, and it is in the opposite phase with the primary current.
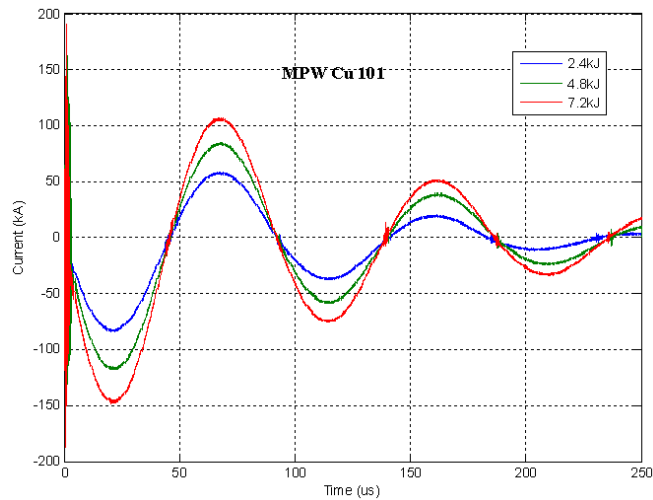
Figure 9.2 Measured primary current for Cu101 plates with different impact energy levels.

9.3.4 Governing Equation

For MPW process, the eddy current approximation

$$\varepsilon_0 \frac{\partial \vec{E}}{\partial t} = 0$$
Equation (9.3)

was applied to the Maxwell equations as shown in below:

$$\vec{\nabla} \wedge \vec{E} = -\frac{\partial \vec{B}}{\partial t}$$

$$\vec{\nabla} \wedge \vec{H} = \vec{j} + \varepsilon_0 \frac{\partial \vec{E}}{\partial t} = \vec{j} + 0 = \vec{j}$$

$$\nabla \bullet \vec{B} = 0$$

$$\nabla \bullet \vec{E} = 0$$

$$\nabla \bullet \vec{j} = 0$$

$$\vec{j} = \sigma \vec{E} + \vec{j}_s$$

$$\vec{B} = \mu_0 \vec{H}$$
Equation (9.4)

These equations described the induced time harmonic EM field in the flyer plate. And the EM module in LS-DYNA can solve them to obtain the induced current density, the electric field, and the magnetic field. The mechanics in MPW process involves extra Lorentz force ($\vec{j} \wedge \vec{B}$) as shown in Equation (9.5).

$$\rho \frac{d\vec{u}}{dt} = \nabla \bullet \ddot{\sigma} + \vec{f} + \vec{j} \wedge \vec{B}$$ Equation (9.5)

And the thermal calculation has extra Joule heating, $\dfrac{j^2}{\sigma\rho}$

$$\frac{D\varepsilon}{Dt} = \ddot{\sigma} : \dot{\varepsilon}^{pl} + \frac{Dq}{Dt} + \frac{j^2}{\sigma\rho} \quad \text{Equation (9.6)}$$

As a result, the governing equation can be regarded as the function of temperature and electric conductivity, $\sigma = \sigma(T, \rho)$, in which T is temperature and ρ is the electric conductivity.

9.4 Preliminary simulation results

9.4.1 Plastic Deformation

The deformation localization at the welded region was observed for MPW joints as shown in Figure 9.3. Materials adjacent to welding zone were stretched and necking occurred near the overlap region. The simulation process also indicated the localized plastic deformation as shown in Figure 9.4. The images were the selected serial snapshots of the induced current in both flyer plate and target plate It was noticed that the maximum current was condensed at the edge of the plate where the necking took place. The snapshots also indicated that the induced current changed direction periodically. The non-uniform plastic deformation leaded to weak joint at the edge of the welded plate.

179
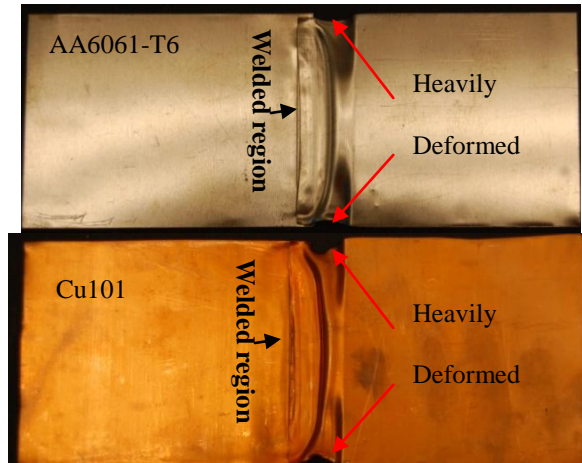
Figure 9.3 Welded piece with necking on the edge of the welded region.
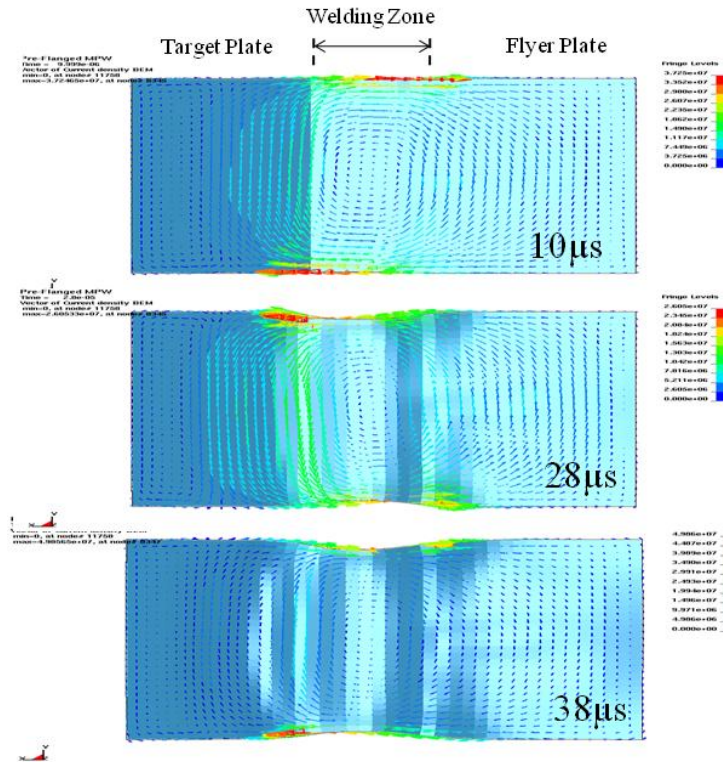
Figure 9.4 Current density distrtubtion in the flyer plate and target plate. The images were

taken from Cu101 joint at 2.4kJ impact energy.

9.4.2　Impact Velocity

The optical fiber laser probe from PDV was focused at one specific position on the flyer plate during impact welding experiment. In order to properly compare the experiment measurement with the simulation result, the particular node at the same position from the flyer plate in the built up 3D model was chosen. And the velocity of this node was taken into the comparison with the PDV data, as shown in Figure 9.5.
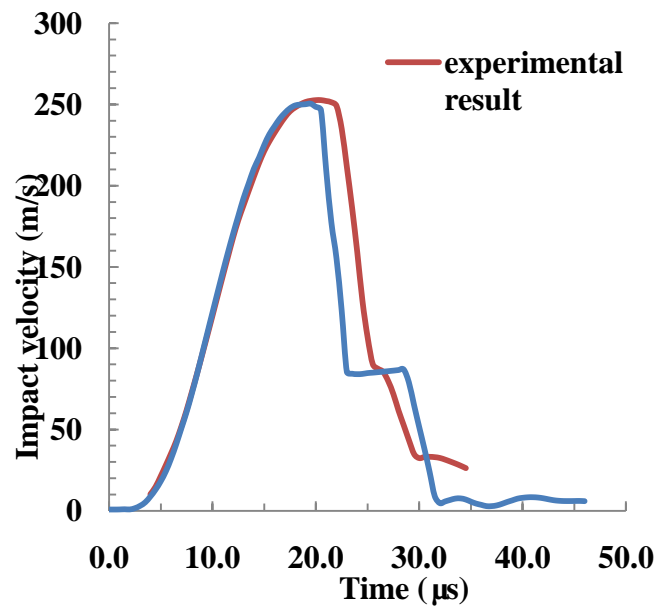
Figure 9.5 Comparison of the flyer plate impact velocity from LS-DYNA simulation and PDV measurement for AA6061 joints at 4.8kJ.
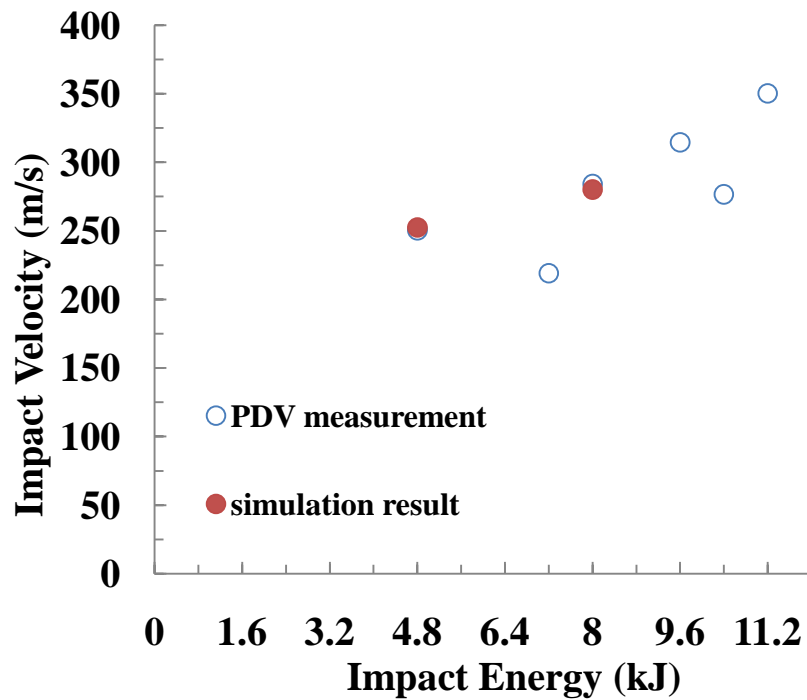
Figure 9.6 LS-DYNA simulated velocity and PDV measured velocity for AA6061 at different impact energy.

The experiment result and the computation result were in a good agreement. They almost had the similar rise time (~20 μs) and peak velocity (~250m/s). The simulation result presented a quick velocity drop after reaching the peak velocity value. The experimental measured velocity decreased from 250m/s to 100m/s and held at this velocity for about 7 μs and then dropped to zero, which was quite different with the simulation result. The possible reason was that during the welding process, the target plate was not stationary and moved with the flyer plate after the collision. Therefore, the impact velocity of the

flyer plate decreased gradually. It is important to point out that, the impact weld is more efficient when the target plate keeps stationary during the collision process. And the experiment setup needs to be improved to avoid the target plate movement.

With the valid model, by plugging different primary current files, the impact velocity can be calculated at different conditions. And the simulation results for both AA6061 and Cu101 joints at different energy level were compared to PDV measurement. The difference was not very significant.

9.5 Conclusion

FEA was used to study the impact welding process with a tight coupling approach, which solves the electromagnetic, thermal, and mechanical property changes in one simulation. The Lorentz force and induced current effect were imposed into Maxwell Equations. The simulation results presented good match with the experiment results. The comparison on the non-uniform deformation and impact velocity helped to verify the simulation models. And the interface temperature was then investigated by this evaluated model.

Chapter 10 Conclusion and future work

10.1 Conclusion

High velocity oblique impact welding technologies are significant because they can be easily applied in typical manufacturing environments, and therefore offer new opportunities for dissimilar metals welding. The studied welding processes are EXW, MPW and LIW. This research work indicates that high velocity oblique impact welding is feasible for all length scales with proper impact angle and velocity. And all of them can be applied to join similar and dissimilar materials. The wave interface is observed at all length scales, and it is presumed that cleaning of the interface by jetting is important in all cases. The jetting removes surface oxide layer and the oblique impact brings the two clean surfaces joint together. In each case a wave interface was generated and the wave length and amplitude are related to both flyer plate thickness and flyer impact velocity. High energy density results in long wavelength and great wave amplitude. EXW has wave interface with vortex; MPW has wave interface near sinusoidal profile; LIW has a relatively gently curved surface. Interfacial intermetallic phase was often found to exist in the wave vortex of explosively welded samples, but there was no continuous intermetallic layer along the welded interface. Intermetallics were possible but isolated in MPW, and were not

observed in LIW. It was also found that all of the three welding processes result in the improved microhardness along the interface after high velocity impact welding. While EXW has earned a reputation for excellent weld quality between widely dissimilar metals, the magnetic pulse and laser impact techniques produce similar structures.

This study particular stresses MPW on similar and dissimilar materials joining with different actuator configuration. The Al-Al, Cu-Cu, Cu-Al and Al-Fe pairs were successfully joined with different process parameters. The critical process parameters are the impact velocity and impact angle. All of the joint strength was examined by mechanical test, such as the lap shear test, the peeling test and the microhardness test. The similar materials joints also underwent nanoindentation tests. For Al-Al, Cu-Cu, Cu-Al, the shearing failure and peeling failure were out of the welded region on the base metals. For Al-Fe, the joint itself was broken at certain stress level. All the hardness tests indicated joint interface has greater hardness value than the base metals. It was also found that the shear strength, peeling strength and hardness of the joint interface increased with the impact energy level (increase of strain rate) and greater than that of the as-received base metals.

Microstructure characterization of MPW on Al-Al pair by EBSD indicates almost one order of magnitude grain refinement in the welded interface comparing to base metals. The data also shows large crystallographic misorientations between these grains. These experimental results confirm the hypothesis of localized high strain rate deformation near the welded interfaces during high velocity impact. The results also

show that the interface is formed mainly by true solid state bonding. Microstructure study suggested the formation of lamellar grains and deformation twins on Cu-Cu joint. Both the lamellar grains and the deformation twins were within nanometer scale, and the twins expanded through the lamellar grains. The interface microstructure for Cu-Al pair was observed from OM, SEM, TEM, and 3DAP. It shows wave morphology with discontinuous pockets of few intermetallic phases, Al_4Cu_{15}. It is also noticed that the interface has various microstructure, such as the lamellar grains, submicron and nanocrystal grains, and teeth-like grains. The composition profile and the 3D morphology with high spatial resolution proved short distance diffusion and possible local melting occurred along the welded Cu-Al interface. For Fe-Al pair, it was found that all of the welded interfaces showed wave pattern and the interface strengths were related to the impact energy level. High impact energy resulted in greater strength due to the extremely refined interfacial grains. The wave amplitude and wave length increased with the impact energy level. However, exceeded impact energy could lead to large amount of intermetallic phase which embrittled the joint. Therefore, the possible strengthening mechanism mentioned in this study includes:

(a) Wave interface morphology increase contact area and enhance interlocking.

(b) Ultrafine grain structure was observed after impact, grain size changes from micrometer to nanometer scale.

(c) Dislocation density increases in crystalline structures.

(d) Twinning, columnar-like grains, lamellar and microbands structure accommodate deformation.

(e) Possible local melting and short range diffusion occurs to form intermetallic phase.

Preliminary FEA based simulation work was also applied to study the similar materials impact welding process with a tight coupling approach, which solves the electromagnetic, thermal and mechanical property changes in one simulation. The Lorentz force and induced current effect were imposed into Maxwell Equations. The comparison on the non-uniform deformation and impact velocity helped to valid the simulation models. And the simulation results indicated a rapid heating on the mating interface. The rising temperature was up to $225\,°$ but less than the melting point of aluminum ($\sim660\,°C$), which indicated that MPW was solid state welding process and no melting was involved for similar materials welding. With the microstructure study, it can be conclude that the generated Joule heating was used to rapidly anneal the impact deformed interface in which the dislocation cellar structure was founded at the grain interior.

10.2 Future work

Impact welding technology is useful for different length scale solid state welding, especially for dissimilar materials welding. EXW has been applied for many industries, whereas MPW has very limited application. In order to spread and develop MPW for more practical application, the following problems need to be solved:

First of all, improve the energy efficiency. For MPW, it is necessary to develop the

capacitor bank and actuator to shorten the rise time. Welding is more likely to take place when the flyer plate collides onto the target no later than the primary current reaching the peak value. For small scale welding, highly focused laser beam should replace the electromagnetic force to impact the materials because the coupling effect from the interference of the electromagnetic field at small scale reduces the efficiency.

Secondly, attempt MPW onto other dissimilar material pairs, such as joint between magnesium alloy and steel, which has been highly demanded in automobile industry; and shape memory alloy joining for medical devices. However, the electric conductivity for both magnesium and steel are lower than that of copper and aluminum alloy, and in order to reach the required impact velocity and impact angle, more impact energy is required.

Thirdly, understand the dynamic deformation at the welded interface. The interface strain rate was established to be in the order of $10^6 \sim 10^7 s^{-1}$ for MPW. It is known that at high strain rate, the materials strain stress relationship is quite different with the quasistatic state, but less experimental strain stress data was available at this strain rate. It is also necessary to avoid the dynamic deformation induced cracking, which was observed away from the welded interface.

Forth, develop instrumental measurement for the spacial and temporal temperature changes during impact welding. This study will help to understand the microstructure evolution. Further TEM work is required to study the structure of the mixture along the welded interface.

Last but not least, improve the FEA based simulation for MPW and apply it onto dissimilar materials welding. Also conduct thermodynamic simulation at micrometer scale to understand the short range diffusion and phase transformation along the welded interface during high pressure impact.

Bibliography

1.	Kore, S.D., *Electromagnetic welding of flat sheets*, in *Mechanical Engineering Department*. 2007, Indian Institute of Technology: Bombay.
2.	Daehn, G.S. and J.C. Lippold, *Low Temperature Spot Impact Welding Driven Without Contact*. 2009: US.
3.	Bahrani, A.S., T.J. Black, and B. Crossland, *The Mechanics of Wave Formation in Explosive Welding.* Proceedings of the Royal Society of London. Series A, Mathematical and Physical Sciences, 1967. **296**(1445): p. 123-136.
4.	Crossland, B., *Explosive welding of metals and its application*. 1982: Oxford New York: Clarendon Press, Oxford University Press.
5.	Blazynski, T.Z., *Explosive welding, forming, and compaction*. 1983, London: New York: Applied Science Publishers.
6.	Tamaki, K. and M. Kojima, *Factors affecting the result of electromagnetic welding of aluminum tube.* Trans. Jpn. Weld. Soc, 1988. **19**(1): p. 53-59.
7.	Shribman, V., et al., *Magnetic pulse welding produces high-strength aluminum welds.* Welding Journal, 2002. **81**(4): p. 33-37.
8.	Hokari, H., et al., *Magnetic impulse welding of aluminium tube and copper tube with various core materials.* Welding international, 1998. **12**(8): p. 619-626.
9.	Lee, K.-J., et al., *Interfacial microstructure and strength of steel/aluminum alloy lap joint fabricated by magnetic pressure seam welding.* Materials Science and Engineering A, 2007. **471**: p. 95-101.
10.	Ben-Artzy, A., et al., *Interface phenomena in aluminium magnesium magnetic pulse welding.* Science and Technology of Welding &# 38; Joining, 2008. **13**(4): p. 402-408.
11.	Hutchinson, N., et al. *Solid state joining of Zr-based bulk metallic glass*. in *TMS*. 2009. San Francisco,CA.
12.	Pulsar *http://www.pulsar.co.il/news/?nid=14*. **Volume**,
13.	Shribman, V. and O. Gafri, *Magnetic Pulse Welding and Joining-A New Tool for the Automotive Industry.* 2001.
14.	Uhlmann, E., R. Hahn, and D. Jurgasch, *Pulsed-Magnetic hot Joining-New Solutions for Modern Lightweight Structures.* Steel Research int., 2005. **76**(2): p. 245-250.
15.	Chizari, M., S.T.S. Al-Hassani, and L.M. Barrett, *Effect of flyer shape on the bonding criteria in impact welding of plates.* Journal of Materials Processing Technology, 2009. **209**(1): p. 445-454.
16.	Palmer, T.A., et al., *Development of an Explosive Welding Process for*

Producing High-Strenght Welds between Niobium and 6061-T651 Aluminum. Welding Journal, 2006: p. 252-263.

17. Kistersky, L., *Welding process turns out tubular joints fast.* Metalworking Distributor, 1996. **140**(4): p. 41-42.

18. Khrenov, K.K. and V.A. Chudakov, *Magnetic pulse welding of butt joints between tubes.* Automatic Welding Ussr, 1969. **22**: p. 75.

19. Aizawa, T., M. Kashani, and K. Okagawa, *Application of Magnetic Pulse Welding for Aluminum Alloys and SPCC Steel Sheet Joints.* Welding in the World, 2005. **49**(9): p. 212-222.

20. Kore, S.D., P.P. Date, and S.V. Kulkarni, *Effect of Process Parameters on Electromagnetic Impact Welding of Aluminum Sheets.* International Journal of Impact Engineering, 2007. **34**: p. 1327-1341.

21. A.A.Ezra, *Principles and Practice of Explosive Metalworking.* Vol. I. 1973, London: Garden City Press.

22. K.K.Botros and T.K.Groves, *Characteristics of the wavy interface and the mechanism of its formation in high-velocity impact welding.* J.Appl.Phys, 1980. **51**(7): p. 3715-3721.

23. K.K.Botros and T.K.Groves, *Fundamental impact-welding parameters-an experimental investigation using a 76-mm powder cannon.* J.Appl.Phys, 1980. **51**(7): p. 3706-3714.

24. Salem, *Some aspects of liquid/solid interaction at high speeds.* 1980.

25. Howard, L.N., *Note on a paper of John W. Miles.* J. Fluid Mech, 1961. **10**(4): p. 509–512.

26. Miles, J.W., *On the stability of heterogeneous shear flows.* J. Fluid Mech, 1961. **10**(4): p. 496–508.

27. Grignon, F., et al., *Explosive welding of aluminum to aluminym: analysis, computations and experiments.* International Journal of Impact Engineering, 2004. **30**: p. 1333-1351.

28. Robinson, J.L., *Fluid Mechanics of Copper: Viscous Energy Dissipation in Impact Welding.* Journal of Applied Physics, 1977. **48**(6): p. 2202-2207.

29. Marya, M. and S. Marya, *Interfacial microstructures and temperatures in aluminium-copper electromagnetic pulse welds.* Science and Technology of Welding and Joining, 2004. **9**(6): p. 541-547.

30. Ezra, A.A., *Principles and Practice of Explosive Metalworking.* Vol. I. 1973, London: Garden City Press.

31. Glouschenkov, V.A., V.F. Karpouchin, and V.A. Pesotsky, in *Proc. 6th Int. conf. on 'Joining of Materials' (JOM-5).* 1993, The European Institute for the Joining of Materials, 473-484: Helsingor, Denmark.

32. Mousavi, A.A.A. and S.T.S. Al-Hassani, *Numerical and experimental studies of the mechanism of the wavy interface formations in explosive/impact welding.* Journal of Mechanics and Physics of Solids, 2005. **53**: p. 2501-2528.

33. Marya, M., D. Priem, and S. Marya, *Microstructures at aluminum-copper magnetic pulse weld interfaces*, in *Thermec, Pts 1-5.* 2003. p. 4001-4006.

34. Stern, A. and M. Aizenshtein, *Bonding zone formation in magnetic pulse welds.* Science and Technology of Welding and Joining, 2002. **7**(5): p. 339-342.

35. Minoru Okada, et al., *Joint Mechanism of Ultrasonic Welding.* Journal of Japan Institute of Metals, 1962. **26**: p. 250-256.

36. Johnson, W., *Impact strength of Materials*. 1972, New York: Crane,Russak & Company, Inc.

37. Seregeeva, Y.A. and V. Chudakov, *Study of the Transition Zone in Aluminum and Copper Joints Made by Magnetic Pulsed Arc Welding*. Avtom. Svarka, 1989(12): p. 5-8.

38. Lucien, T., *Electron-Microscope Study of Thermal Recovery Processes in Explosion-Shocked Nickel*. Journal of Applied Physics, 1969. **40**(7): p. 2976-2987.

39. Wakeman, D.W., *The physical chemistry of copper, copper-the science and technology of the metal, its alloys and compounds*, ed. A.C. Society. 1954: Reinhold Publishing Corporation.

40. Hultgren, R., et al., *Selected values of the thermodynamic properties of binary alloys*. 1973: American Society for Metals.

41. T. Aizawa, M.Kashani, and K. Okagawa, *Application of Magnetic Pulse Welding for Aluminum Alloys and SPCC Steel Sheet Joints*. International Conference on New frontiers of Process Science and Engineering in advanced Material, 2004.

42. T. Aizawa, M.Kashani, and K. Okagawa, *Application of Magnetic Pusle Welding for Aluminum alloys and SPCC Steel Sheet Joints*. Welding Journal, 2007: p. 119-124.

43. Cao, X., et al., *Research and progress in laser welding of wrought aluminum alloys. II. Metallurgical microstructures, defects, and mechanical properties*. Materials and Manufacturing Processes, 2003. **18**(1): p. 23-49.

44. Cao, X., et al., *Research and progress in laser welding of wrought aluminum alloys. I. Laser welding processes*. Materials and Manufacturing Processes, 2003. **18**(1): p. 1-22.

45. Jones, I.A., et al., *Laser welding of aluminium alloys*. TWI Journal, 1998. **7**(2): p. 421-481.

46. Naeem, M. and R. Jessett, *Welding aluminum tailored blanks with Nd: YAG laser for automotive applications*. Pract. Weld. Today, 1999. **3**(1): p. 24–28.

47. Quinones, S.A., et al., *Direct observations and comparison of crater cross-section microstructures in copper targets for aluminium projectiles impacting at 1.4 and 6.7 km(-1)*. Journal of Materials Science, 1996. **31**(15): p. 3921-3927.

48. Rohatgi, A. and K.S. Vecchio, *The variation of dislocation density as a function of the stacking fault energy in shock-deformed FCC materials*. Materials Science and Engineering a-Structural Materials Properties Microstructure and Processing, 2002. **328**(1-2): p. 256-266.

49. Huang, J.C. and G.T. Gray, *Microband Formation in Shock-Loaded and Quasi-Statically Deformed Metals*. Acta Metallurgica, 1989. **37**(12): p. 3335-3347.

50. Jackson, P.J., Scripta Materialia, 1983. **17**: p. 199-205.

51. M.Hatherly and A.S.Malin, Metal Tech., 1979. **6**: p. 308.

52. A.S.Maline and M.Hatherly, ibid., 1979. **13**: p. 463.

53. Chen, M.W., et al., *Deformation twinning in nanocrystalline aluminum*. Science, 2003. **300**(5623): p. 1275-1277.

54. Esquivel, E.V., et al., *Comparison of microstructures for plane shock-loaded*

and impact crater-related nickel: the microtwin-microband transition. Journal of Materials Science, 2003. **38**(10): p. 2223-2231.

55. Rohatgi, A., K.S. Vecchio, and G.T. Gray, *A metallographic and quantitative analysis of the influence of stacking fault energy on shock-hardening in Cu and Cu-Al alloys.* Acta Materialia, 2001. **49**(3): p. 427-438.

56. Murr, L.E., A. Ayala, and C.S. Niou, *Microbands and shear-related microstructural phenomena associated with impact craters in 6061-T6 aluminum.* Materials Science and Engineering a-Structural Materials Properties Microstructure and Processing, 1996. **216**(1-2): p. 69-79.

57. Johari, O. and G. Thomas, *Factors Affecting Dislocation Sub-Structure in Deformed Copper.* Acta Metallurgica, 1964. **12**: p. 679-686.

58. Grace, F.I., *Shock-Wave Strengthening of Copper and Nickel.* Journal of Applied Physics, 2003. **40**: p. 2649.

59. L.E.Murr, *Shock Waves and High-Strain Rate Phenomena in Metals*, ed. M.A.M.a. L.E.Murr. 1981, New York. 607.

60. DeAngelis, R.J. and J.B. Cohen, *Some Crystallographic Techniques for the Study of Mechanical Twnning and their Applicaion to Shock-Induced Twinning in Copper*. 1963: Northwestern Univ Evanston Ill Technological, Inst.

61. L.E.Murr, et al., *Shock-induced deformation twinning in Tantalum.* Acta Materialia, 1997. **45**(1): p. 157-175.

62. Embury JD, Szczerba MS, and B. ZS, *Twinning in advanced materials*, ed. W.M. Yoo MH. 1994, Warrendale: The Minerals, Metals and Materials Society. 331-336.

63. G.T.Gray, *High Pressure Shock Compression of Solids*, ed. M.S. J.R.Asay. 1993, New York: Springer-Verlag.

64. R.Asfhani, E.Chen, and A. Crowson, *High Strain Rate Behavior of Refractory Metals and Alloys*. 1992, Warrendale,PA: The Metallurgical Society.

65. M.A.Meyers, L.E.Murr, and K.P.Staudhammer, *Shock Wave and High-strain-rate phenomena in Materials*. 1992, New York: Marcel Dekker.

66. K.Wongwisal and L.E.Murr, Materials Science and Engineering, 1978. **35**: p. 273.

67. G.E.Dieter, *Response of Metals to HIgh Velocity Deformation*. 1961, New York: Wiley Interscience.

68. F.Greulich and L.E.Murr, Mater.Sci.Engng, 1979. **37**: p. 81.

69. L.E.Murr, *Shockwaves in Condensed Matter*, ed. N.D.H. S.C.Schmidt. 1998: Elsevier Science.

70. L.E.Murr, *Materials at High Strain Rates*, ed. T.Z.Blazynski. 1987, New York/London: Elsevier Science.

71. Gray, G.T.I., R.S. Hixson, and C.E. Morris. in *Shock Compression of Condensed Matter Proc. conf.* 1991. Williamsburg,VA,USA: Elsevier Science Publishers.

72. L.E.Murr, *Interfacial Phenomena in Metals and Alloys*. 1975, Reading, MA: Addison-Wesley.

73. Marc Andre Meyers and K.K. Chawla, *Mechanical Metallurgy Principles and Applications*, ed. T.S. Bette Kurtz, Natalie Krivanek. 1984, Englewood Cliffs: Prentice-Hall Inc.

74. Ogata, S., J. Li, and S. Yip, *Ideal pure shear strength of aluminum and copper.*

Science, 2002. **298**(5594): p. 807.

75.   Heino, P., et al., *Stacking-fault energy of copper from molecular-dynamics simulations.* Physical Review B, 1999. **60**(21): p. 14625-14631.

76.   R.W.Armstrong and P.J.Worthington, *Metallurgical Effects at High Strain Rates*, ed. B.M.B. R.W.Rohde, J.R.Holland,C.H.Karnes. 1973, new York.

77.   Smith, C.S., *Metallographic Studies of Metals after Explosive Shock.* Trans.Met.Soc.AIME, 1958. **212**(574-589).

78.   Weertman.J., *High Velocity Dislocations.* Proc.Met.Soc.Conf. Response of Metals to High Velocity Deformation, 1960. **205-247**.

79.   Weston, J. and R. Wallach, *Mechanical properties of laser welds in aluminum alloys*, in *Proc.INALCO'98/7th Int. Conf.: Joints in Aluminum.* 2000: Cambridge.

80.   F.A.Shunk, *Constitution of binary alloys, Second supplement*. Vol. 24. 1969, New York: McGraw-Hill.

81.   *ASM handbook.* Welding, Brazing and Soldering. Vol. 6. 1993: American Society for Materials.

82.   Armstrong, R.W., in *Deformation Twinning Proc.Conf.* 1963, Gordon and Breach Science: Florida,USA.

83.   Wright, R.N. and D.E. Mikkola, *Deformation Twinning: Time Dependence and Associated Strengthening Effects in Shock-Loaded Cu--8. 7 At.-% Ge.* MATER. SCI. AND ENG., 1982. **53**(2): p. 273-283.

84.   Dudas, J.H. and F.R. Collins, *Preventing weld cracks in high-strength aluminum alloys.* Welding Journal, 1966. **45**(6).

85.   Matsunawa, A., et al., *Porosity formatin and solidification cracking in laser welding*, in *Proc. Taiwan Int. Welding Conf.'98 on Technology Advancements and New Industrial Applicaitons in Welding,*. 1998: Taipei, Taiwan.

86.   Matsunawa, A., S. Katayama, and Y. Jujita, *Laser welding of aluminum alloys-defects formation mechanisms and their suppression methods*, in *Proc. 7th Int. conf./INALCO'98: Joints in Aluminum.* 1998: Cambridge.

87.   Kanazawa, H., *Welding performance of high power yag lasers with aluminum alloys.* J. Light Met. Weld. Constr., 1997. **35**(7): p. 10-15.

88.   Dausinger, F., et al., *Laser beam welding of aluminum alloys: state of the art and recent developmetns*, in *Proc. Int. Body Engineering Conf. IBEC'97: Advanced Technologies and Processes.* 1997: Stuttgart, Germany.

89.   Markashova, L.I., et al., *Evolution of a dislocation structure of a zone of thermal influence of welded steel-20 joints under electrohydraulic pulse treatment.* Metallofizika I Noveishie Tekhnologii, 2000. **22**(4): p. 67-70.

90.   Markashova, L.I., G.M. Grygorenko, and V.V. Arsenyuk, *The processes of plastic deformation, mass transfer, and phase formation under the conditions of increased deformation rates.* Metallofizika I Noveishie Tekhnologii, 2001. **23**(9): p. 1259-1277.

91.   Markashova, L.I., et al., *Features of the phase formation in conditions, of pressure welding of dissimilar materials at high-rate deforming.* Metallofizika I Noveishie Tekhnologii, 2001. **23**(10): p. 1403-1417.

92.   L.I.Markashova, et al., Paton Weld.J., 1991. **3**: p. 187-191.

93.   Kachan, M.S. and V.N. Shtern, *Explosive Welding and the Stefan Problem.* Combustion Explosion and Shock Waves, 1979. **15**(2): p. 214-220.

94. Lysak, V.I., *Evaluation of Factors Determining the Reliability of Explosive Welding.* Welding Production, 1979. **26**(3): p. 9-12.

95. Sudarshan, T.S., *Explosive Welding of Metals and Its Application - Crossland,B.* Journal of Metals, 1983. **35**(10): p. 68-68.

96. Kornev, V.M. and I.V. Yakovlev, *Model of Undulation in Explosive Welding.* Combustion Explosion and Shock Waves, 1984. **20**(2): p. 204-207.

97. Linse, V.D. and N.S. Lalwaney, *Explosive Welding.* Journal of Metals, 1984. **36**(5): p. 62-65.

98. Szecket, A., et al., *A Wavy Versus a Straight Interface in the Explosive Welding of Aluminum to Steel.* Journal of Metals, 1984. **36**(12): p. 28-28.

99. Zhang, X.D., et al., *Explosive Welding of Multifilamentary Nbti50-Cu Composite Superconductor.* Journal De Physique, 1984. **45**(Nc-1): p. 611-614.

100. Bazdenkov, S.V., et al., *Possible Mechanism of Wave Formation in Explosive Welding.* Combustion Explosion and Shock Waves, 1985. **21**(1): p. 124-130.

101. Bondar, M.P. and V.M. Ogolikhin, *Plastic-Deformation in Bonding Zone under Explosive Welding and Its Role in Bonding Formation.* Journal De Physique, 1985. **46**(Nc-5): p. 379-384.

102. Szecket, A., et al., *A wavy versus straight interface in the explosive welding of aluminum to steel.* Journal of Vacuum Science & Technology A: Vacuum, Surfaces, and Films, 1985. **3**: p. 2588.

103. Simonov, V.A., *Binding Criterion for Metals with Explosive Welding.* Combustion Explosion and Shock Waves, 1991. **27**(1): p. 121-123.

104. Simonov, V.A., *The Relationship between Plastic-Deformation and Collision Angle in Explosive Welding.* Combustion Explosion and Shock Waves, 1991. **27**(3): p. 352-355.

105. Vaidyanathan, P.V. and A.R. Ramanathan, *Design for Quality Explosive Welding.* Journal of Materials Processing Technology, 1992. **32**(1-2): p. 439-448.

106. Brasher, D.G. and D.J. Butler, *Explosive Welding - Principles and Potentials.* Advanced Materials & Processes, 1995. **147**(3): p. 37-38.

107. Abe, A., *Numerical study of the mechanism of wavy interface generation in explosive welding.* Jsme International Journal Series B-Fluids and Thermal Engineering, 1997. **40**(3): p. 395-401.

108. Buchar, J., S. Rolc, and V. Hruby, *On the explosive welding of a ring to the axisymmetric body.* Journal of Materials Processing Technology, 1999. **85**(1-3): p. 171-174.

109. Holtzman, A.H. and G.R. Cowan, *Bonding of Metals with Explosives.* Welding Research Council Bulletin, 1965. **104**.

110. A.Ben-Artzy, et al., *Interface Phenomena in Aluminum-Magnesium Magnetic Pusle Welding*, Pulsar Welding Ltd.

111. Okada, M., et al., *Joint Mechanism of Ultrasonic Welding.* Journal of Japan Institute of Metals, 1962. **26**: p. 250-256.

112. Krishnan, J., et al., *An Experimental Investigation into Tube to Tube-plate Welding Using the Impactor Method.* Journal of Materials Processing Tech., 1990. **22**: p. 191-201.

113. Volobuev, I.V. and A.V. Legeza, Weld Prod. (USSR), 1972. **19**(8): p. 12-15.

114. Hammerschmidt, M. and H. Kreye, *Metallurgical characterisation of the*

explosively weld zone. J. Metals, 1984. **37**(3): p. 12–21.

115. Al-Hassani, S.T.S., S.A. Salem, and G.L. Lazari, *Exposive welding of flat plates in free flight.* Int.J. Impact Eng., 1984. **1**(2): p. 85-101.

116. Al-Hassani, S.T.S., *Numerical and experimental investigation of explosive bonding process variables and their influence on bond strength.* 2001, University of Manchester Institute of Science and Technology: Manchester,UK.

117. Mousavi, A.A.A., S.J. Burley, and S.T.S. Al-Hassani, *Simulation of explosive welding using the Williamsburg equation of state to model low detonation velocity explosives.* International Journal of Impact Engineering, 2005. **31**(6): p. 719-734.

118. Reid, S.R., *A Discussion o fthe Mechanism of Interface Wave Generation in Explosive Welding.* International J. Mech. Sci., 1974. **16**: p. 399-413.

119. Otto, H. and S.H. Carpenter, *Explosive Cladding of Large Steel Plates with Lead.* Met. Mater, 1973: p. 75-79.

120. Robinson, J.L., *A FLUID MODEL OF IMPACT WELDING.* 1975.

121. Wronka, B., *The influence of base plate thickness and anvil on the characteristics of explosive welded joints.* Insight, 1999. **41**(6): p. 383-387.

122. Jaramillo, D. and V. Szecket, *On the Transition From a Waveless to a Wavy Interface in Explosive Welding.* Mater. Sci. Eng., 1987. **91**(1): p. 217-222.

123. Epechurin, V.P., *Porperties of Bimetals Joints Produced by Magntic Pulse Welding.* Welding Production, 1974. **21**(5): p. 21-24.

124. Demichev, V.F., *The use of strong-pulsed magnetic fields to weld metals.* Atomic Energy, 1992. **73**(4): p. 793-798.

125. Chankvetadze, Z.A., *Technological Characteristics and Conditions of Formation of Joints in Magnetic-Pulse Welding.* Automat. Weld. (USSR), 1979. **32**(6): p. 26-28.

126. J.Krishnan, et al., *An Experimental Investigation into Tube to Tube-plate Welding Using the Impactor Method.* Journal of Materials Processing Tech., 1990. **22**: p. 191-201.

127. Panshikar, H.M., *Computer modeling of electromagnetic forming and impact welding.* 2000, Ohio State University.

128. Nemat-Nasser, S., Y.F. Li, and J.B. Isaacs, *Experimental/computational evaluation of flow stress at high strain rates with application to adiabatic shear banding.* Mechanics of Materials, 1994. **17**(2): p. 111-134.

129. Vadovic, C.J. and C.P. Colver, *Hard-Sphere Model for Self-Diffusion in Liquid Metals.* Physical Review B, 1970. **1**(12): p. 4850-4851.

130. Turcotte, R., et al., *Thermal hazard assessment of AN and AN-based explosives.* Journal of Hazardous Materials, 2003. **101**(1): p. 1-27.

131. Johnson, J.R., et al., *Couplign Experiment and Simulation in Electromagnetic Forming Using Photon Doppler Velocimetry.* Metal Forming, 2009. **80**(5): p. 359-365.

132. Ben-Artzy, A., et al., *Wave Formation Mechansim in Magnetic Pulse Welding.* 2006.

133. Banik, K., *Factors affecting electromagnetic flat sheet forming using the uniform pressure coil*, in *Materials Science and Engineering.* 2008, The Ohio State University: Columbus,OH.

134. Kamal, M., *A uniform pressure electromagnetic actuator for forming flat sheets*, in *Materials Science and Engieering*. 2005, The Ohio State Univeristy: Columbus,OH.

135. Zhang, P., *Joining Enabled by high velocity deformation*, in *Department of Materials Science and Engineering*. 2003, The Ohio State Unviersity: Columbus. p. 271.

136. Strand, O.T., et al. *Velocimetry using heterodyne techniques*. 2005.

137. Zhang, Y., et al., *Application of high velocity impact welding at varied different length scales*. Journal of Materials Processing Technology, 2010.

138. Kore, S.D., P.P. Date, and S.V. Kulkarni, *Effect of process parameters on electromagnetic impact welding of aluminum sheets*. International Journal of Impact Engineering, 2007. **34**(8): p. 1327-1341.

139. Masumoto, I., K. Tamaki, and M. Kojima, *Electromagnetic welding of aluminum tube to aluminum or dissimilar metal cores*. Trans. Jpn. Weld. Soc, 1985. **16**(2): p. 110-116.

140. Kendall, K., *Shrinkage and peel strength of adhesive joints*. Journal of Physics D: Applied Physics, 1973. **6**: p. 1782-1787.

141. Wilson, A.W. and G. Spanos, *Application of orientation imaging microscopy to study phase transformations in steels*. Materials Characterization, 2001. **46**(5): p. 407-418.

142. Courtney, T.H., *Mechanical Behavior of Materials*. 1990, New York: McGrill-Hill. 80-136 and 263-324.

143. Thilly, L., F. Lecouturier, and J. Von Stebut, *Size-induced enhanced mechanical properties of nanocomposite copper/niobium wires: nanoindentation study*. Acta Materialia, 2002. **50**(20): p. 5049-5065.

144. Minor, A.M., et al., *A new view of the onset of plasticity during the nanoindentation of aluminium*. Nature Materials, 2006. **5**(9): p. 697-702.

145. El-Sobky, H., *Mechanics of explosive welding*. Explosive Welding, Forming, and Compaction, ed. T.Z. Blazynski. 1983: Applied Science Publishers. 189-217.

146. Wu, X., et al., *Microstructure and evolution of mechanically-induced ultrafine grain in surface layer of AL-alloy subjected to USSP*. Acta Materialia, 2002. **50**(8): p. 2075-2084.

147. Zhilyaev, A.P., et al., *An evaluation of microstructure and microhardness in copper subjected to ultra-high strains*. Journal of Materials Science, 2008. **43**(23): p. 7451-7456.

148. Zhang, H.W. and N. Hansen, *Deformed metals and alloys with a structural scale from 5 nm to 100 nm*. Journal of Materials Science, 2007. **42**(5): p. 1682-1693.

149. Kanel, G.I., et al., *Spall fracture properties of aluminum and magnesium at high temperatures*. Journal of Applied Physics, 1996. **79**: p. 8310.

150. Huang, C.X., et al., *Deformation twinning in polycrystalline copper at room temperature and low strain rate*. Acta Materialia, 2006. **54**(3): p. 655-665.

151. Andrade, U., et al., *Dynamic recrystallization in high-strain, high-strain-rate plastic deformation of copper*. Acta Metallurgica et Materialia, 1994. **42**: p. 3183-3183.

152. Bussiba, A., et al., *Grain refinement of AZ31 and ZK60 Mg alloys—towards*

superplasticity studies. Materials Science & Engineering A, 2001. **302**(1): p. 56-62.

153. Mishra, R.S., et al., *High strain rate superplasticity in a friction stir processed 7075 Al alloy.* scripta materialia, 1999. **42**(2): p. 163-168.
154. Komura, S., et al., *High strain rate superplasticity in an Al-Mg alloy containing scandium.* Scripta materialia, 1998. **38**(12): p. 1851-1856.
155. Hughes, D.A. and N. Hansen, *Graded nanostructures produced by sliding and exhibiting universal behavior.* Physical Review Letters, 2001. **87**(13): p. 135503.
156. Hughes, D.A., et al., *A microstructurally based method for stress estimates.* Wear, 1995. **181**: p. 458-468.
157. Yamakov, V., et al., *Dislocation processes in the deformation of nanocrystalline aluminium by molecular-dynamics simulation.* Nature Materials, 2002. **1**(1): p. 45-49.
158. Daehn, G.S., et al. *Coupling Experiment and Simulation in Electromagnetic Forming Using Photon Doppler Velocimetry.* in *3rd International Conference on High Speed Forming.* 2008. Dortmund, Germany.
159. Gjostein, N., *Diffusion, ASM, Metals Park.* 1973, Ohio. 241-274.
160. Y lmaz, M., M. Çöl, and M. Acet, *Interface properties of aluminum/steel friction-welded components.* Materials Characterization, 2003. **49**(5): p. 421-429.
161. Fukumoto, S., et al., *Friction welding process of 5052 aluminium alloy to 304 stainless steel.* Materials Science and Technology, 1999. **15**(9): p. 1080-1086.
162. Chen, C.M. and R. Kovacevic, *Joining of Al 6061 alloy to AISI 1018 steel by combined effects of fusion and solid state welding.* International Journal of Machine Tools and Manufacture, 2004. **44**(11): p. 1205-1214.
163. Rathod, M.J. and M. Kutsuna, *Joining of aluminum alloy 5052 and low-carbon steel by laser roll welding.* WELDING JOURNAL-NEW YORK-, 2004. **83**(1): p. 16.
164. Lee, W.B., et al., *Interfacial reaction in steel–aluminum joints made by friction stir welding.* Scripta Materialia, 2006. **55**(4): p. 355-358.
165. Park, Y.B., H.Y. Kim, and S.I. Oh, *Joining of thin-walled aluminum tube by electromagnetic forming (EMF).* International Journal of Automotive Technology, 2005. **6**(5): p. 519-527.
166. Kikuchi, M., H. Takeda, and S. Morozumi, *Bonding Interfaces in Friction- and Explosive-Welded Aluminum and Steel Joints.* J. Jpn. Inst. Light Met., 1984. **33**(3): p. 165-173.
167. Uzun, H., et al., *Friction stir welding of dissimilar Al 6013-T4 to X5CrNi18-10 stainless steel.* Materials and Design, 2005. **26**(1): p. 41-46.
168. Elrefaey, A., M. Takahashi, and K. Ikeuchi, *Friction-Stir-Welded Lap Joint of Aluminum to Zinc-Coated Steel.* Quarterly Journal of the Japan Welding Society, 2005. **23**(2): p. 186-193.
169. Babu, S.S., *Thermodynamic and kinetic models for describing microstructure evolution during joining of metals and alloys.* Internatinal Materials Reviews, 2009. **54**(6): p. 333-367.
170. Brown, W.F., J. Bandas, and N.T. Olson, *Pulsed Magnetic Welding of Breeder Reactor Fule Pin End Closures.* Welding Journal, 1978: p. 22-26.

171. Zhang, Y., et al. *Numerical Simulation and Experimental Study for Magnetic Pulse Welding Process on AA6061-T6 and Cu101 Sheet*. in *10th International LS-DYNA Users Conference Simulation Technology*. 2008. Dearborn,MI.

172. Alcoa. *http://www.matweb.com/search/DataSheet.aspx?MatID=9391&ckck=1*. [cited; Available from: http://www.matweb.com/search/DataSheet.aspx?MatID=9391&ckck=1.